Development of a scintillation-based CMOS Quantitative Autoradiography imager for Safeguard Applications

By

Ardelia Michelle Clarke

Dissertation

Submitted to the Faculty of the

Graduate School of Vanderbilt University

in partial fulfillment of the requirements

for the degree of

DOCTOR OF PHILOSOPHY

in

Physics

December 12, 2020

Nashville, Tennessee

Approved:

Todd E. Peterson, Ph.D.

Mary Bliss, Ph.D.

Arnold Burger, Ph.D.

Kevian G. Stassun, Ph.D.

Norman H. Tolk, Ph.D.

PACIFIC NORTHWEST NATIONAL LABORATORY
operated by
BATTELLE
for the
UNITED STATES DEPARTMENT OF ENERGY
under Contract DE-AC05-76RL01830

Dedication

To my spiritual guiding light, thank you for the favor, mercy, grace, love, and strength to see this journey to the end.

To my phenomenal mother, Christine Burson, for her unwavering support, unconditional love, and perseverance to always strive to be different and limitless.

and

To my praying grandparents, Malcolm and Ardelia Clarke, for their drive and faith to never let me give up.

Acknowledgments

This research was supported in part by the U.S. National Nuclear Security Administration (NNSA) Office of International Nuclear Safeguards within the U.S. Department of Energy (DOE) under Contract DE-AC05-76RL01830. Pacific Northwest National Laboratory is a multi-program national laboratory operated by Battelle for the U.S. Department of Energy.

Table of Contents

Page

List of Tables

Page

List of Figures Page

Chapter 1

Introduction

This dissertation's primary objective is to demonstrate a detailed understanding of radiation detection and how radiation (alpha, beta, photons) interact within a digital autoradiography radiation imager called the large-area ionizing-radiation Quantum Ionizing Detector (iQID). Secondly, this dissertation will characterize the imaging capabilities and performance limitations of the large-area iQID (LA-iQID) and its quantitative imaging of samples relevant to safeguards applications and make targeted advancements to iQID hardware and analysis approaches. The LAiQID offers promising characteristics as an imaging tool for safeguards. According to the International Atomic Energy Agency (IAEA), safeguards are technical measures applied to verify nuclear material and activities independently [1]. The correctness and completeness of a state's nuclear declarations are within the guidelines of various international agreements. Overall, IAEA safeguards' primary purpose is to deter nuclear proliferation by ensuring that nuclear materials and facilities are peacefully used [1]. Satellite imagery, nondestructive assay, sample analyses, and environmental swipe sampling are examples of critical technical tools useful in safeguards applications [2] [3]. This dissertation will focus on the latter topic of environmental swipe sampling.

Environmental swipe sampling is when an IAEA inspector enters a state's declared facility and physically swipes surfaces using cotton fabric squares. These cotton fabric squares swipe on surfaces are defined as environmental swipe samples (ESS). These swipe samples are placed in two plastic bags to prevent cross-contamination. Next, swipe samples' dose rates are collected in the field using handheld instruments to determine the laboratories for further analysis.

Multiple swipes are simultaneously analyzed by gamma counting via high-resolution gamma spectroscopy (HRGS). Flagged swipes from HRGS are placed into x-ray fluorescence spectroscopy (XRF) to map uranium concentrations [4]. Section 1.3 **below** will further discuss more information related to these two imaging techniques. Overall, the full process of collecting swipe samples in the field, shipping, examining, and locating particles of interest takes the IAEA on the scale of months to complete. This dissertation proposes to offer an alternative method of locating particles by using the LAiQID.

Pacific Northwest National Laboratory (PNNL) previously developed an approach to prioritize ESS by examining and locating particles of interests using the iQID imager [5]. This methodology from PNNL included the LAiQID due to multiple beneficial imaging characteristics useful as a technical measure for safeguards. First, the LAiQID has a larger imaging area than the smaller iQID configuration due to a fiber-optic taper (10 cm x 10 cm). The addition of a fiber-optic taper allows for the LAiQID to simultaneously image the swipe sample's area. The taper in the LAiQID may provide some limitations to energy resolution by causing blurring across the larger imaging area rather than guiding light towards the readout device. Secondly, the LAiQID is easily portable for in-field measurements and is inexpensive due to assembly with commercially off-the-shelf- (COTS) parts. Thirdly, the iQID imager has a high spatial resolution or ability to locate particles of interest within a region of interest [6] [7]. Other unique performance characteristics, such as the signal generation process, of the LAiQID is due to corresponding hardware components, are further explained in Chapter 2 **below.**

L. Han investigated the performance limitations in energy resolution and particle discrimination of the LAiQID [8]. Preliminary results demonstrated the LAiQID might lack pulse-shape discrimination due to the presence of an image intensifier.

As a result, these preliminary theoretical and experimental analysis lower the capability of particle and energy discrimination with the LAiQID [8]. This dissertation will re-investigate particle and energy discrimination in the LAiQID. This topic is of interest because Miller et al. found some discrimination capabilities in smaller-iQID imaging systems. In this previous study, beta particles were discriminated against and appeared as elongated event shapes in the post-processing output window [6]. If the LAiQID can achieve similar discrimination, it may improve the imager's ability as a pre-screening prioritization tool to measure high priority swipe samples.

To determine whether the LAiQID has any usefulness as a technical tool in safeguards, its baseline performance must be characterized first. The metrics included spatial resolution, minimum detectable activity (MDA), energy response, detector uniformity, dead time, and count-rate (Chapter 3 **below).** The count-rate capability of the LAiQID was further investigated, in Chapter 4 **below,** using a gated image intensifier and a 506 μCi ^{241}Am source. The gated functionality added to the LAiQID allows the imager to quantitatively image hot samples' activities (10^7 Bq) similar to those found on swipe samples. Overall, the LAiQID must be able to detect higher count-rates to apply to safeguards. If the LAiQID cannot discriminate between different types of radiation such as beta vs. gamma events, this lowers its utility in safeguards applications. As shown below, this dissertation focuses on three topic areas. Each topic reveals information regarding whether the LAiQID can quantitatively image samples relevant to safeguards applications.

1. To characterize the baseline performance of the LAiQID and identify promising characteristics useful for safeguards applications
2. To investigate the count-rate capability of the LAiQID to promote quantitative imaging at higher count-rates by investigating spatial pileup

3. To implement enhancements to list-mode post-processing algorithms for particle and energy discrimination with iQID

I experimentally characterized the LAiQID for spatial resolution, minimum detectable activity (MDA), energy response, dead time, detector uniformity, and count rate capability as baseline performance measurements. Previous data from count-rate capability measurements of a smaller-iQID system were replicated and compared to the characterized count-rate of the large-area iQID. A. Clarke published these results in Nuclear Instruments and Methods in Physics Research Section A: Accelerators, Spectrometers, Detectors, and Associated Equipment (NIMA) journal in an article titled "Characterization of Large-area iQID Imager for Safeguards Applications" [9]. These results will be presented in Chapter 3. Also, previous Monte Carlo radiation transport modeling results from MCNP6 for photons and electrons up to 1 keV were included to compare against measured results in the Appendix. Similarly, Edward Siciliano calculated MCNP theoretical photon and beta efficiencies compared to measured absolute efficiencies for beta and gamma sources [10] [11].

The second aim of this dissertation explored the count-rate capability of the large-area iQID in three different experiments. The first experiment compared two separate detectors based on spatial pileup. Selected imagers were the large-area iQID and a cadmium telluride (CdTe) semiconductor detector called High-Energy X-ray Spectroscopic Imaging Detector (HEXITEC) [12]. HEXITEC was chosen as a comparable detector based on its detector characteristics such as detector accessibility, simpler detector size (i.e., cluster size < 10 pixels), and higher count-rate capability than the large-area iQID. Despite HEXITEC's higher count-rate ability, the performance tradeoffs of HEXITEC are small detector area and high cost [13].

Firstly, the purpose was to calculate the experimental spatial pileup for the large-area iQID and determine whether the large-area iQID may achieve quantitative imaging at higher count-rates (sample activities up to 10^7 Bq). An analytical algorithm for calculating spatial pileup was created and benchmarked for HEXITEC. Researchers at the University of Arizona previously developed the theoretical spatial pileup framework for detectors similar to HEXITEC [14]. Therefore, the HEXITEC detector assisted to create the analytical spatial pileup MATLAB algorithm.

Next, a Monte Carlo simulation algorithm (MC algorithm) in MATLAB was designed and compared to the analytical MATLAB algorithm of HEXITEC. I hypothesized the derived analytical solution of spatial pileup for HEXITEC would be closely aligned to its spatial pileup stimulated via the MC algorithm.

Once validated, this Monte Carlo simulated algorithm was adapted to calculate the experimental spatial pileup of the large-area iQID. Characterized count-rates for large-area iQID assisted in creating the spatial pileup algorithm for the large-area iQID. The purpose was to determine whether large-area iQID could remain quantifiable at higher count-rates. This experimental algorithm for large-area iQID evaluated observed events per frame and spatial pileup. One preliminary finding demonstrated a close agreement between analytical, simulated, and experimental spatial pileup of the large-area iQID demonstrating pileup gradually increased as event-rate increased (Chapter 4 **below).**

The second experiment evaluated how the hardware components of the large-area iQID could affect its count-rate capability. Two separate tests assisted in investigating count-rate capability. Quantitative imaging with the large-area iQID and other iQID systems typically occurred at 20 frames per second (fps) and fixed CMOS shutter time of 49 ms [6]. These were considered the nominal settings for imaging with the large-area iQID. I proposed investigating the count-rate capability of the large-area iQID by adjusting the frame-rate and shutter time of the CMOS sensor.

The LABVIEW image acquisition software of the large-area iQID allowed a user to set specific values for imaging parameters. Examples of these parameters include but are not limited to CMOS frame-rate, CMOS shutter time, the cluster size of radiation interactions, image intensifier value, and CMOS gain. I used the graphical user interface (GUI) of LABVIEW acquisition software to set these specified imaging parameters.

The first test of the count-rate experiment investigated the effect of a gated image intensifier on the large-area iQID. One must characterize the gated signal of the gated image intensifier to ensure proper operation with a function generator. The gated functionality of the image intensifier was a new hardware addition for LAiQID. The duty cycle and waveform polarity were the two most adjusted imaging parameters for the gated image intensifier. When the photocathode is sensitive to light, the duty cycle is at a higher percentage. The gated signal could have a waveform polarity set to normal or inverted. Count-rate linearity and absolute efficiency were the two metrics evaluated throughout these measurements.

The final count-rate experiment investigated whether the large-area iQID could remain quantitative at higher count-rates. This experiment used a 506 μCi ^{241}Am source. I hypothesized that the gating image intensifier of the LAiQID enables quantitative imaging at high count-rates. The gated signal on the image intensifier controls the amount of scintillation light the LAiQID detects, hence potentially allowing for manageable count-rates when imaging higher activity samples. Count-rate, spatial pileup, average event-rate, and frame count density were the metrics for evaluation. Reducing the CMOS shutter time and using the gated image intensifier were the two selected methods to reduce spatial pileup as frame count density (photons/frame) increased due to the activity of the ^{241}Am source. Two scenarios evaluated quantitative imaging of the large-area. The first scenario reduced the CMOS shutter time from 49 ms to 9 ms. The second scenario increased the duty cycle of the gated image

intensifier from 10% to 100%. Both scenarios methods investigated the linearity between count-rate and measured activity as a metric for quantitative imaging with the large-area iQID.

Lastly, I investigated the feasibility of improved particle and energy discrimination with the large-area iQID by implementing post-processing data cuts. The event cluster shape, area, and intensity were the metrics for the data cuts. Cluster area equates to the number of pixels that contain signal or event clusters collected by the large-area iQID. Cluster intensity is the amount of energy deposited by a particular type of radiation interaction, such as alpha, beta, and gamma sources. I chose cluster intensity and area as the metrics for data cuts with the large-area iQID. I did not select cluster shape as a discriminating metric due to diminished particle differences by the fiber-optic taper. A previous study by Taggart et al. demonstrated techniques for discriminating gamma/neutron events with pulse shaped discrimination (PSD) plastic scintillators and silicon photo-multiplier tubes (SiPMs) [15]. This study's methods have implemented the feasibility of discriminating different particle and energy type with the large-area iQID. A 2D histogram could be used to quantify the ability of the LAiQID to differentiate beta/gamma events based on cluster intensity and cluster area. The outcome of this study was to determine whether a figure of merit (FOM) could be calculated to quantify the LAiQID imager's ability to discriminate betas and gammas. A detector with a FOM higher than 1.27 may be suitable for gamma discrimination [15]. The large-area iQID will use this FOM value to state whether the imager can distinguish beta/gamma events. To differentiate between beta and gamma events, I have hypothesized that gamma events deposit a large amount of energy (high cluster intensity) across a large cluster area. In contrast, beta events deposit a large amount of energy across a smaller cluster area. Chapter 5 **below** will further explain these results. This chapter's remaining part will introduce further basic definitions and concepts necessary to understand this dissertation's outcomes and impact.

1.1. Radiation Sources and Interactions with Matter

Radiation is the emission of energy in the form of three different groups, charged particles, photons, or neutrons. Charged particles consist of the emission of alphas, betas, electrons, positrons, etc., whereas photons are electromagnetic waves and include gamma- and x-rays. Different types of radiation pass through matter differently. A charged particle moving through a material interacts mostly by Coulombic forces. This charged particle interacts with the atoms that make up that material, consisting of the positive nuclei and negative electrons. Through these Coulombic interactions, the charged particle loses energy continuously while traversing a finite distance called range. The particle's lost energy accumulates until the charged particle comes to a stop. The particle's range depends on the particle's type and energy and the material through which the particle moves. There is practically a zero probability that a charged particle goes through a material without an interaction. Unlike neutrons, gamma-rays have an electric field, which both interacts differently with matter than charged particles. Likewise, neutrons and gammas have a finite nonzero probability that they may travel through any material thickness without interaction. Therefore, there is no limited range defined for neutrons or gammas [16]. This dissertation will not discuss neutrons further; instead, the emphasis is on alpha and beta particles and photon interactions.

How radiation interacts with matter depends on the type of particle, absorber, and relative kinetic energy. Therefore, all charged particles' common energy-loss mechanism involves slowing down a moving charged particle or reducing the particle's momentum. A particle loses energy based on Coulombic interactions (collision processes) between the particle and electrons in the chosen medium. If the moving charged particle is heavy or massive (i.e., alpha particles) and traversing matter, then the particle loses its energy through the ionization and excitation of the medium/absorber atoms.

Several assumptions regarding the collision process relate to the amount of energy transferred to the massive charged particle traversing the medium. For example, the maximum energy transfer occurs if the collision is head-on. Likewise, the amount of energy transferred is larger than the electron's binding energy in the absorber atom. This interaction is called an elastic collision that conserves energy (Equation 1 **below**) and momentum (Equation 2 **below**) via the law of conservation of kinetic energy and momentum for alphas and electrons. In these equations, the variables are as followed: massive particle of rest mass is *M*, the initial speed of the alpha particle is *V*, the final velocity of an alpha particle is V'_1, and final speed of the electron is V'_2, and the mass of the electron is *m* [17].

$$\frac{1}{2}M\bar{V}^2 = \frac{1}{2}M\overline{V'_1}^2 + \frac{1}{2}m\overline{V'_2}^2 \qquad \textbf{Equation 1}$$

$$M\bar{V} = M\bar{V}_1 + m\overline{v_1} \qquad \textbf{Equation 2}$$

$$Q_{max} = \frac{1}{2}\left(M\overline{V^2} - M\overline{V_1^2}\right) = \frac{4mME}{(M+m)^2} \qquad \textbf{Equation 3}$$

Q_{max} is the fractional energy loss per elastic collision, and $E = \frac{MV^2}{2}$ is the incident particle's initial kinetic energy. The average linear rate of energy loss, $\left(\frac{MeV}{cm}\right)$ of a massive charged particle, is calculated from an elastic collision between massive charged particle and electron [18]. Energy loss relates to the stopping power$\left(-\frac{dE}{dx}\right)$ of the medium (Equation 4 **below)**. Therefore, a particle's kinetic energy is proportional to the rest mass for a given particle's speed relative to the speed of light (β).

$$-\frac{dE}{dx} = \frac{5.08\ x\ 10^{-31} z^2 n}{\beta^2}[F(\beta) - ln\ I_{ev}]\frac{MeV}{cm} \qquad \textbf{Equation 4 } [17]$$

$$F(\beta) = \ln \frac{1.02\ x\ 10^6 \beta^2}{1-\beta^2} - \beta^2$$

Parameters in Equation 4 **above** are $\beta = \frac{V}{c}$ for speed of the particle relative to the speed of light *c*, *z* for the atomic number of the massive particle, *n* for the number of electrons per unit volume in the medium or electron density, and *I* for the mean excitation energy of the medium.

While traversing through the medium, the moving charged particle creates an ionization track due to the electromagnetic force exerted on absorber atomic electrons. The electromagnetic force transfers its energy to these atomic electrons until the energy transferred is higher than the ionization threshold or sufficient energy to eject an electron out of the atom. As a result, the electron is either excited to a higher energy state (i.e., orbital) around the nucleus or ejected from the atom leaving the atom ionized. A massive charged particle only transfers a small fraction of its energy during a single electronic collision, so any deflection from one interaction is negligible. The interaction between massive charged particles and absorber electrons produces some very unique characteristics for the charged particles. These unique characteristics are as follows: straight ionization paths expected near their ends, well-defined mean distance-of-travel or range, sharp changes in direction occur at the end of the ionization path where particles are slowing down (i.e., nuclear collisions), and higher density of ions at the end of the ionization track. Note interactions within the nuclei can occur but do not contribute to a moving massive charged particle's primary energy/flux reduction mechanism. Additionally, the alpha particle's charge is two electron charges and loses its energy at a rate of 1/E, as demonstrated in Equation 4 **above** [17].

1.1.1 Charge-particle energy loss mechanism

1.1.1.A Coulomb Interactions

Charged particles traveling through a medium interact with the atoms of that material. As a result, the fast-moving charged particle can either interact with the bound electrons or with the atom's nucleus. Interactions with atomic electrons are favorable over nuclear collisions based on the difference in the nucleus' radius (10^{-14} m) and atom (10^{-10} m). This dissertation will not mention nuclear collisions further. Atomic collisions between electrons and charged particles place the charged particle at a particular position *P* in time and the electron at position *E*. The distance between the charged particle and electron is *r*, the charge of the electron is *ze* where *z* is the charge number or atomic number and *e* is the electronic charg*e*, and *k* is a constant. The Coulomb force for this scenario is expressed in Equation 5 **below** [19]**.**

$$F = k\frac{ze^2}{r^2} \qquad \textbf{Equation 5}$$

Over time, the Coulomb force on the electron may cause the moving charged particle to transfer its energy to a bound electron. The transfer of energy from Coulomb force to bound electron converts the electron into a quantized state. At this particular state, ionization or excitation can occur as the charged particle passes by the material's atoms. Ionization occurs when the bound atomic electron gains enough energy to detach from the atom and become a free particle. This ejected electron's kinetic energy is equal to the energy given by the incident charged particle minus the ionization potential necessary to expel the bound electron. Once emitted from the atom, the electron can now act as a moving charged particle. This high-energy electron (once ejected) can cause secondary ionization of another atom while it interacts within the material and loses its kinetic energy.

Secondary ionization will occur until the high-energy electron becomes trapped. In addition to a new free high-energy electron, the process of ionization results in a positive ion. This positive ion is a massive particle when compared to the free-moving electron. As both the free electron and positive ion move through the material, the ion will move slower than the free electron. The positive ion may not move during the ionization process because the activation energy necessary to move an atom in a solid absorber material is significantly high. Radiation damage occurs if displaced atoms are present within the absorber. At some point in time, the positive ion will return to a neutral state by picking up an electron [17] [19].

On the other hand, the excitation process of Coulomb interactions occurs when an electron obtains enough energy (i.e., excited electron) to move to an empty yet higher energy state within the same atom. In a short time (10^{-8} to 10^{-10} s), the electron will move to a lower unoccupied energy state (E_2-E_1). The energy emitted is in the form of an X-ray (or photon) with a frequency $v = \frac{(E_2 - E_1)}{h}$. Overall, collisions that result in ionization or excitation are called elastic collisions due to the law of conservation of kinetic energy (Equation 1 **above**) and momentum (Equation 2 **above**). [17] [19].

1.1.1.B Emission of Electromagnetic Radiation (Bremsstrahlung)

Most charged particles accelerate or decelerate its kinetic energy through the emission of electromagnetic radiation. This braking radiation or bremsstrahlung radiation is not mono-energetic but consists of photons with energies ranging from zero to the particle's kinetic energy. The emission of bremsstrahlung radiation is energy with intensity proportional to the square of its acceleration. Equation 6 **below** represents emitted bremsstrahlung radiation where *ze* is the charge of the moving particle, *M* is the mass of the moving particle, and *Z* is the material atomic number [17].

$$I\ \alpha\ a^2 \sim \left(\frac{zZe^2}{M}\right)^2 \sim \left(\frac{z^2Z^2}{M^2}\right) \qquad \textit{Equation 6}$$

Equation 6 **above** demonstrates a lighter particle will emit a more significant amount of bremsstrahlung radiation than the more massive particle when both are traveling in the same material. Charged particles that travel through higher atomic number *Z* materials generate more bremsstrahlung radiation *[17]*.

1.1.1.C Alpha Decay

Alpha decay is a spontaneous emission of an alpha particle when one radioactive isotope decays to a more-stable progeny/daughter isotope, as shown in Equation 7 **below**. The transition from parent to daughter isotope is defined by the energy difference or Q-value between both isotopes and its probability to have enough energy to overcome the energy threshold [17]. The emission of the alpha particle accounted for the energy difference and detected using the large-area iQID.

$$^{A}_{Z}X \rightarrow\ ^{A-4}_{Z-2}Y + ^{4}_{2}\propto \qquad \textit{(Equation 7)}$$

Alpha particles are massive particles and equal to the helium nucleus' size and mass, as shown in Equation 8 **below**. Alphas are the least penetrating form of radiation and can only transmit their energy within a distance of a few micrometers through soft tissue [16]. In other words, a sheet of paper has enough thickness to stop alpha particles. Alpha particles traverse within the absorber atoms, hitting the nucleus and come to a halt (thickness of sheet of paper, 90 μm.

$$2\,{}_0^1n + 2\,{}_1^1p = {}_2^4He \qquad \textit{(Equation 8)}$$

Therefore, as alpha particles lose energy traveling through matter, alphas travel in a straight line and are easily stopped at a small range within the material. The straight-line trajectory occurs because a massive charged particle only transfers a small fraction of its energy during Columbic collisions. Therefore, any deflection during one interaction is negligible [17] [19].

1.1.1.D Beta Decay

As shown in Equation 9 **below**, beta decay is a spontaneous emission of a beta particle and an anti-neutrino during the unstable radioactive decay of a parent isotope to a more stable daughter isotope. Beta-decay can occur via beta- or beta+ decay, which emits an anti-neutrino and neutrino, respectively. Neutrinos won't be discussed further in this dissertation. Beta-decay can also eject a photon (i.e., gamma-ray) and will be discussed further in the next sub-section **below**.

$$ {}_Z^AX \rightarrow {}_{Z+1}^{A}Y + \beta^- + \bar{\nu} \qquad \textit{(Equation 9)}$$

Isotopes that have a higher likelihood of emitting beta particles are called pure beta emitters. Pure beta emitters discussed throughout this dissertation are ^{90}Sr/ ^{90}Y, ^{99}Tc, and ^{14}C. The Q-value for beta emission is a fixed value based on the mass differences between the parent and daughter isotopes. The energy emitted from the beta particle can occur over a range of energies from 0 to maximum theoretical energy or beta endpoint energy due to multiple ways in which the beta together with the progeny nucleus and neutrino.anti-neutrino (i.e., three-body final state) can conserve energy and momentum.

Beta particles are lighter in weight than alphas (one electron vs. 2 protons); hence betas emit a more significant amount of bremsstrahlung radiation than alphas. Beta particles interact less readily within the atoms or molecules due to their small size. Beta particles have a greater penetration power than alphas. Therefore, a few mm of aluminum can attenuate and stop beta particles [16]. The difference in penetration power is due to electric charge interactions. Betas have charge and smaller mass than alphas so, they interact and penetrate deeper.

1.1.1.E Photon Interactions (Gamma-rays)

Gamma rays are electromagnetic radiation (photons) created within the nucleus during radioactive decay. Electron transitions make x-rays and other photons in the orbitals surrounding the nucleus and, in the case of x-rays, the acceleration of charged particles. Gamma-rays interact with a material to produce an energetic electron that creates secondary ionization events. There are three significant types of gamma-ray interactions: photoelectric absorption, Compton scattering, and pair production energy (**Figure 1**), further described in sub-sections below [16].

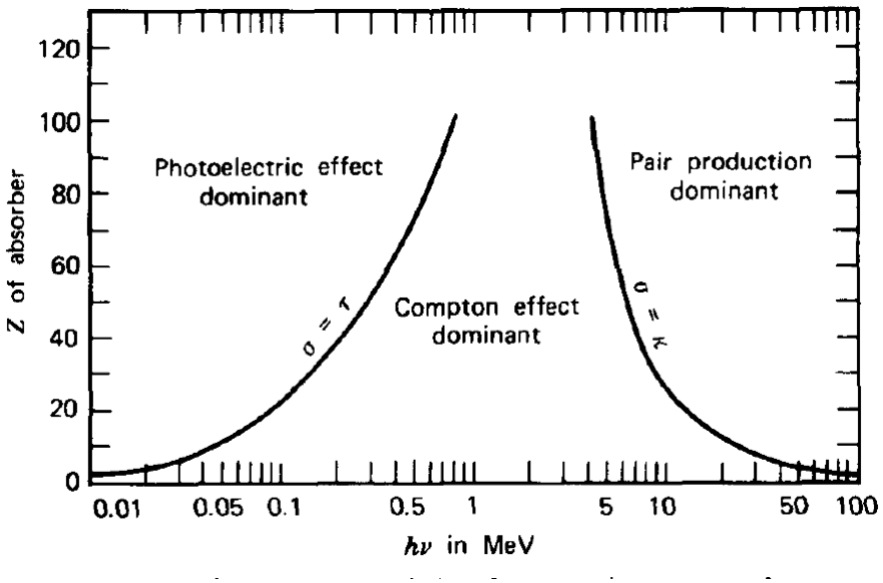

***Figure 1**: Schematic of Gamma-Ray Interactions and their corresponding energy regimes as a function of Z number of the material [16].*

1.1.1.E.i Photoelectric Absorption

Incident radiation of photons (gamma-ray/X-ray) can interact within an atom in the material. The interaction between photons and an atom's nucleus transfers the photon's energy to a bound electron (i.e., photoelectron). This action causes the photoelectron's ejection and is called photoelectric absorption. The photoelectron's ejection leaves a vacancy that once filled emits an X-ray or an Auger electron. Typically, the electron binding energy E_b is significantly lower than the incident radiation, so most incident radiation is close to the photoelectron's energy. There is a higher probability of secondary photoelectric effects within a short-range (100 μm) when a higher orbital energy electron fills the vacancy left from the emitted photoelectron.

In some cases, a characteristic X-ray can also be emitted (Auger effect). There is a higher probability for photoelectric absorption than Compton scattering at lower energies when gamma-ray photons interact in high Z materials. **Figure 1** [16]. Normally, the characteristic X-ray is re-absorbed at a different site. If photoelectric absorption occurs at the surface, an X-ray can escape, as depicted in **Figure 2**. The amount of energy lost by the escape of the X-ray is equal to the X-ray photon energy. On the other hand, if the X-ray photon does not escape, then the detector's gamma-ray is absorbed with energy deposited to the photo-peak [16].

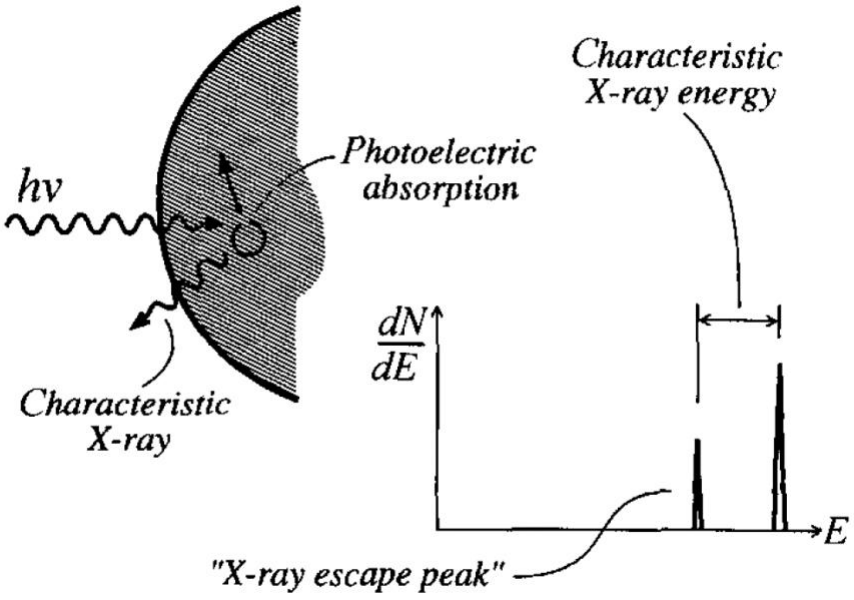

***Figure 2**: Schematic description of how an X-ray escapes from material and its effect on the pulse-height spectrum [16].*

1.1.1.E.ii Compton Scattering

Compton scattering is the second process that can occur during gamma-ray interactions.

In this process (**Figure 3**), the incident gamma-ray photon transfers its energy ($\hbar v$) to an electron called the recoil electron [16]. The recoil electron is deflected or scattered at an angle Φ relative to the incoming amount of energy transferred from the incident photon. Energy transferred between the incident photon and recoil electron also affects the photon. The higher amount of energy transferred from the incident photon to the recoil electron equates to a larger scattered angle θ. As a result, the scattered incident photon has an angle θ and energy ($\hbar v'$). The scattered photon can be mathematically represented by Equation 10 **below**, where m_0c^2 is equal to 511 keV or the electron's rest energy [17].

$$\hbar v' = \frac{\hbar v}{1+\frac{\hbar v}{m_0 c^2}(1-\cos\theta)} \qquad \textit{Equation 10}$$

Compton scattering tends to be a likely process when a secondary gamma-ray interaction occurs with a low scattered photon angle θ. A secondary gamma-ray interaction can lead to further photoelectric capture within the detector or a cascade of Compton scattering events with low-energy gamma-rays [16].

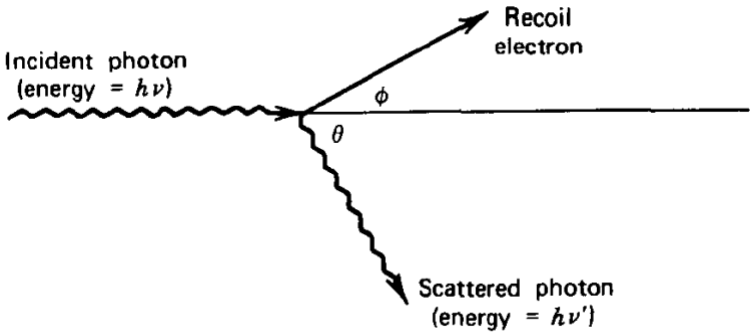

***Figure 3**: Schematic Demonstration of Compton Scattering within a Material between an incoming incident photon (energy= hv) and a material which transfers energy to an electron at a corresponding scattered angle Θ [16].*

The amount of Compton scattering generated within a material is proportional to the number of protons or effective atomic number (Z) inside the atom's nucleus that can absorb the energy from such interaction to emit an electron. Hence, as the Z number increases, more electrons are present in each atom. Therefore, a material with a high Z number has weakly bound electrons and easier to eject. Absorption of incident radiation produces secondary electrons and Compton scattering events. Similarly, Rayleigh scattering can occur when a gamma-ray photon interacts with all the electrons in the absorber material. However, the atom is neither excited nor ionized as the gamma-ray photon keeps all its energy without transferring to electrons. Meanwhile, the photon's direction is different in Compton scattering, prominent at low energies with high- Z materials. The last interaction that occurs at the higher energy regime is called pair production [16].

1.1.1.E.iii Pair Production

At energies exceeding 1.02 MeV in **Figure 1** above**,** pair production is the dominant process. Pair production occurs when an electron-positron pair replaces a previously displaced gamma-ray photon. A positron is an anti-matter particle similar to the electron but having a positive charge. This electron-positron pair gains kinetic energy, but eventually, the positron slows down inside the material's absorbing medium. The slowing down of the positron also generates secondary annihilation photons. A gamma-ray detector can detect when pair production occurred by the signal from the incident gamma-ray photon's energy. Overall, the three main gamma-ray interactions are vital to this research in detecting radiation interactions in the large-area iQID. Primary gamma-rays are challenging to collect via a detector. High energy gamma-rays that generate secondary ionization events or fast electrons can provide information about the incident radiation through the absorber material [16].

1.2.Radiation Detectors: Semiconductors and Scintillators

Overall, a radiation detector can detect all radiation types described above (alpha, beta, photons). Various radiation detectors utilize different radiation interaction mechanisms and deduce information about the radiation type and energy. For the scope of this dissertation, semiconductors and scintillators will be the only radiation detectors discussed further. Semiconductors typically provide the best energy resolution, whereas scintillators are less expensive and more versatile. For imaging, the optimum sensor depends on the application and other parameters such as uniformity, efficiency, spatial and energy resolution, and count-rate capability [20]. Based on the desired application, some of these parameters can have dominating contributions in performance tradeoffs. These parameters will be characterized further in Chapter 3 **below** to use performance metrics to determine a detector's suitability for other application spaces such as national security and international safeguards.

1.2.1. Semiconductors

Semiconductor diodes operate as thermalized electrons and holes migrate with an electric field's assistance to produce an electronic pulse proportional to the incident photon's energy. The solid crystalline material of the semiconductor creates a periodic lattice with energy bands for electrons. Energy bands represent the electron's energy. These energy bands are defined as a forbidden range of energies and specify the type of material. Semiconductors typically have a smaller energy gap than insulator materials. As shown in **Figure 4**, the semiconductors' energy gap is greater than or equal to 1 eV. The lower band, the valence band, represents the outer-shell electrons bound to specific lattice sites within the crystal.

The next upper band is called the conduction band and represents the electrons free to migrate through the crystalline material under an applied electric field. The electrons within the conduction band correspond to the electrical conductivity of the material [16].

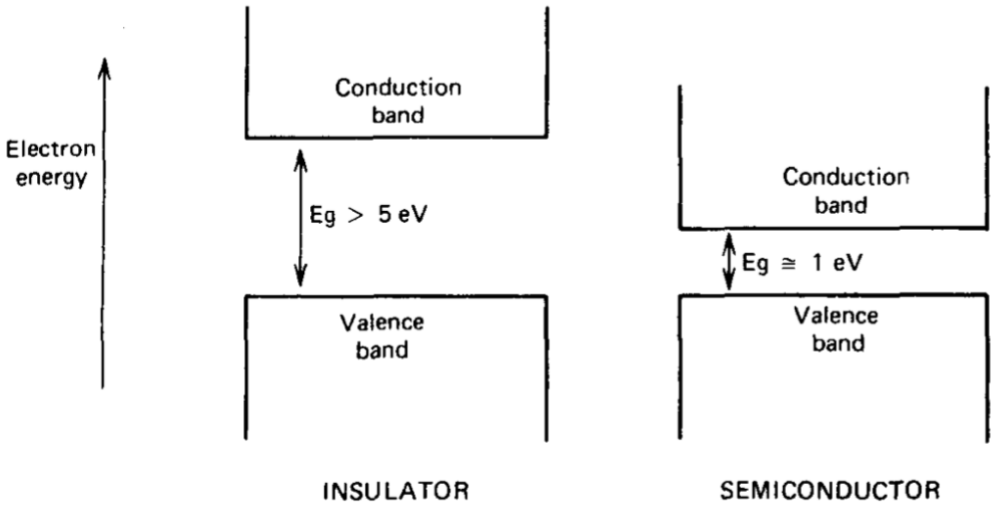

***Figure 4**: Insulators and semiconductor band structure for electron energies [16].*

When a charged particle interacts within a semiconductor, the particle deposits its energy and produces multiple electron-hole pairs along the particle's track (i.e., ionization track). As the incoming charged particle enters and traverses the semiconductor, the particle generates high-energy electrons. High-energy electrons generate more electron-hole pairs along the incident particle's track. The particle's energy deposition leads to the formation of conduction electrons and valence holes within picoseconds along the ionization track. Once a valence electron gains significant thermal energy, the covalently bonded electron is excited across the bandgap into the conduction band (i.e., excitation process). The excited electron leaves a vacancy (i.e., a hole) in the valence band, representing a new positive charge.

The number of created electrons and holes are equal despite whether the semiconductor is pure, intrinsic, doped p-type, or n-type. The amount of average energy expended by the incident charged particle to produce one electron-hole pair is called ionization energy $\in$. Ionization energy is independent of energy and type of incident radiation.

Within the detector's active volume, as the particle comes to a full halt, the number of electron-hole pairs produced is relative to the incoming radiation's incident energy. The active volume of the semiconductor has an applied electric field. Electrostatic forces act on the electron-hole pairs or charge carriers, which cause them to drift in opposite directions. The drifting motion of electrons or holes creates an electric current until the charge carriers arrive at their respective nodes. Electrons travel in the opposite direction towards the electric field vector, whereas the holes will move in the same direction as the electric field. Equation 11 **below** represents the probability per unit time of thermally generated electron-hole pair. T is absolute temperature, E_g is the bandgap energy, k is Boltzmann constant, and C is continuous proportionality characteristics of the material.

$$p(T) = CT^{\frac{3}{2}} exp\left(-\frac{E_g}{2kT}\right) \qquad \textit{Equation 11}$$

The time it takes the charge carriers to be collected is based on drift distances and charge carrier mobilities. The mobility μ for both electrons and holes is defined by Equation 12 **below** where v is the drift velocity proportional to the applied electric field, and ε is the electric field's magnitude. The rising pulse produced by a preamplifier signifies the charge carriers' current integrated on a measuring circuit. A preamplifier processes the counts from the semiconductor detector [16].

$$v_h = \mu_h \varepsilon$$
$$v_e = \mu_e \varepsilon$$

Equation 12

One prominent semiconductor detector class is high purity germanium (HPGe), which possesses advantageous properties useful for radiation spectroscopy such as excellent energy resolution. These semiconductor detectors are commonly manufactured in a four-inch right cylinder, can be expensive, and must be operated at low temperatures, making scintillators more appealing as radiation detectors depending on application [16]. Different types of semiconductors include solid-state, silicon-based detectors, charged-particle, gamma-ray spectrometers, and visible light imaging detectors. This dissertation will focus on semiconductors as imaging detectors. Semiconductors used as digital imaging technology/cameras are typically either charge-coupled devices (CCD) or complementary metal-oxide-semiconductor (CMOS). Traditionally, CCD sensors create high-quality, low noise images with high power consumption, high fill factor, quantum efficiency, and dynamic range. CMOS's imaging technology provides low cost and power consumption with a high capability for radiation hardness, integration, and high-speed readout but generally have more noise in the pixel readout. This research will discuss CMOS sensors in greater detail in the hardware and characterization sections.

1.2.2. Scintillators

There are two main types of scintillators, organic and inorganic, based on their composition. The desired application of the detector determines the kind of scintillator. Beta spectroscopy and fast neutron detection applications prefer organic scintillators. In contrast, inorganic scintillators are favorable for gamma-ray spectroscopy due to the high Z-value of the constituents and high density to stop gamma-rays within the material [16].

The ideal scintillator consists of specific properties: high scintillation efficiency or the ability to convert electron kinetic energy into visible light, high light output linearity to the incident energy (high defined as greater than 25,000 photons/MeV), transparent to scintillation light for excellent light collection, short decay time, ability to manufacture at large sizes, and index of refraction near glass (~1.5) to enhance the coupling of scintillation light to the readout device [16].

1.3.Nuclear Safeguards and Applications

This dissertation proposes adopting a known medical imaging detector to safeguards and nuclear nonproliferation applications. This dissertation plans to detect radiation using digital autoradiography. The International Atomic Energy Agency (IAEA) was established in 1957 to guide international cooperation on nuclear energy and facilities' peaceful uses. The Non-proliferation Treaty in 1970 and Comprehensive Safeguards further expressed this commitment through book auditing and non-destructive and destructive assay methods [21] [22] [23]. Additional information and access from declared states were required by IAEA to strengthen international safeguards and deter nuclear proliferation. Therefore, a legal document was attached to some country's IAEA safeguards agreement and approved in 1997. This additional document was called the Additional Protocol [2] [23]. The Additional Protocol provided the IAEA with further access to verify a state's declared nuclear activities and facilities. This additional access, given by the Additional Protocol, implemented other approved technologies to deter nuclear nonproliferation such as satellite imagery, remote monitoring, and environmental swipe sampling [24]. This dissertation proposes to study an alternative method for its usefulness in ESS analysis by characterizing the large-area iQID imager to prioritize radiation sources with activities below 0.001 Bq to 10^7 Bq for in-field measurements. These source activity ranges are similar to observed activities found on environmental swipe samples (ESS); hence these limits are essential to detect on the large-area iQID.

The current process of environmental swipe sampling by the IAEA has multiple steps. First, an inspector enters a previously declared facility, physically swiping surfaces of interest using 10 x 10 cm square pieces of pure cotton from ITW Mahwah, NJ (TX304 TexWipe) cotton cloths. Next, the inspector places these swipe samples or ESS into two plastic bags to minimize cross-contamination. Both inner and outer plastic bags are four mils (0.020 cm) thick. Thirdly, handheld radiation detection instruments collect ESS dose rates during field collection [5]. These dose rates guide shipment options and which laboratories receive ESS samples. The environmental sample kits are all prepared in the "clean room" of the Environmental Sample Laboratory or "Clean Laboratory" located in Seibersdorf, Austria (**Figure 5**).

***Figure 5**: Image of the IAEA Clean Laboratory in Seibersdorf, Austria [25].*

The sealed sample kits are only opened at the inspection site and contain essential equipment for a field IAEA inspector.

These sample kits consist of two pairs of latex gloves, 6-10 swipes, sample data form, pen, labels, aluminum foil to provide a clean working area, and plastic zip lock bags to collect and store the swipe samples (**Figure 6**). An outer sealed bag ships these double-bagged swipe environmental samples to the IAEA.

***Figure 6**: Image of IAEA cotton swipe kit for environmental sampling [25].*

The IAEA Clean Laboratory, 18 accredited laboratories from 8 IAEA Member States, and the European Atomic Energy Community can analyze the swipe samples. Anonymized swipe samples have the country's identity and collection location removed and screened for radioactivity signatures and elemental composition. Member States such as Australia, Brazil, France, the United Kingdom, and the United States encompass the IAEA Network of Analytical Laboratory (NWAL). Designated laboratories receive swipe samples [4]. Samples are sent to the Nuclear Material Laboratory (NML) if the radioactivity on the ESS samples is above limits for field shipment to IAEA Clean Laboratory. The IAEA Clean Laboratory receives all swipe samples below limits for radioactive field shipment. There are two technical measures used to analyze these swipe samples. Bulk isotopic gamma spectroscopy with high-resolution gamma spectroscopy (HRGS) non-destructively screened swipe samples first. X-ray fluorescence spectrometry (XRF) is the second technical tool. Swipe samples can be screened for alpha and beta to detect actinides or beta-emitting isotopes (i.e., ^{90}Sr, ^{99m}Tc). NWAL may receive ESS after IAEA screening measurements for further analysis [4] [25] [26].

Isotope dilution mass spectrometry (IDMS) method for IAEA measures dissolved irradiated area of the swipe sample. Analyzing a smaller swipe sample area or higher signal noise ratio is preferrable for mass spectrometry. A known quantity of a unique isotope (i.e. spike) is added to the swipe sample solution. The resulting solution is analyzed by a highly sensitive (10^{-15} g) plasma mass spectrometer and pulse counting detector measure swipe samples further [25] [27].

For the first IAEA screening technique, at the Clean Laboratory, several swipe samples (>10 ESS) are placed into the same container for bulk isotopic gamma counting by low-background HRGS. High-resolution gamma spectroscopy has a 90% efficient coaxial germanium detector enclosed in a high purity lead shield (10 cm thick). Several ESS are placed in beakers inside a 15-sample changer and counted for an hour each.

Total gamma activity is corrected to generate a gamma-ray spectrum with an energy range from 5 keV to 3 MeV. If sufficient activity is detected, spectral peaks' emissions compare the swipe sample's activity to individual gamma-emitting isotopes (i.e., ^{60}Co, ^{137}Cs, ^{241}Am) [25].

In addition to HRGS screening, the IAEA also uses XRF screening on swipe samples. Samples with activity from beta emitters, may not be detected by HRGS due to the thickness or type of detector faceplate [25]. Swipe samples are analyzed for trace amounts (scale on nanogram to milligrams) of uranium with an XRF instrument if HRGS detects no gammas. An example of a typical ESS uranium distribution map made with the TRIPOD XRF system is in **Figure 7.** Held by a robotic arm, X-rays (from an X-ray tube) irradiated the plastic bagged swipe sample to emit X-rays. Fluorescent X-rays are detected using a 100 mm^2 Si(Li) detector placed near the swipe sample. Analyzing the detected X-ray fluorescence spectra can determine the elemental composition of radioactive material on a swipe because X-ray photons have a higher penetration power. As sample thickness increases, more atoms are excited by X-ray photons. Therefore, the sensitivity of XRF increases for a larger number of samples. The XRF background mainly comes from low-energy scattered photons from exciting primary energy, while charge particle interactions (alphas and betas) generate a bremsstrahlung continuum [28]. The IAEA XRF instrument (TRIPOD XRF) takes 4-5 hours per swipe to map locations (spatial distribution) of uranium concentrations with a sensitivity of ~ 35 ng/cm^2 [25].

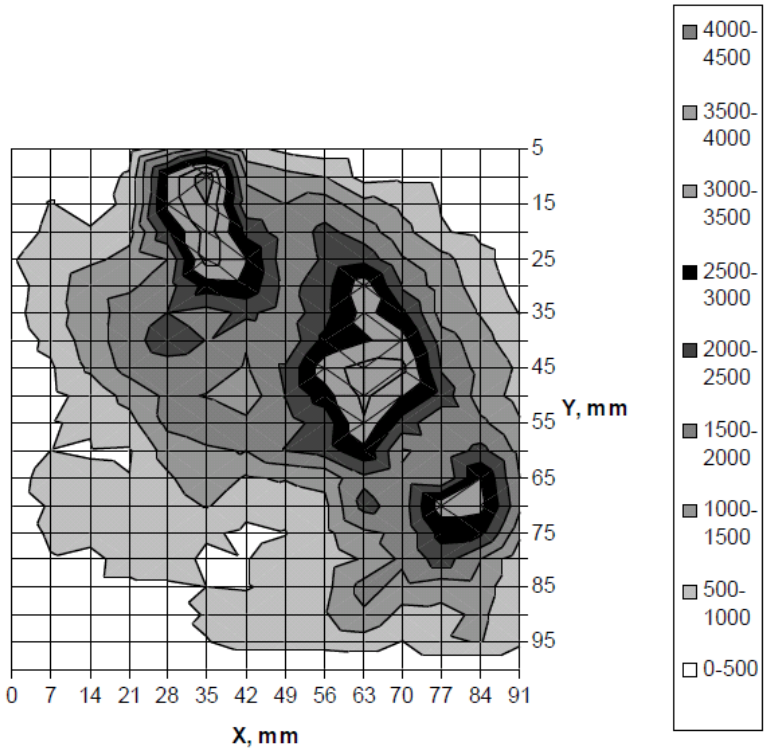

Figure 7: *XRF map produced from the TRIPOD system. Darker colors indicate higher concentrations of Uranium. The scale is given in terms of ng of Uranium. The highest concentrations are where the inspector's fingers pressed against the swipe. The total amount of Uranium on the swipe is 0.32 mg [29].*

HRGS and XRF are two critical techniques used by IAEA for screening and prioritizing swipe samples. Some developments have occurred to improve the XRF instrument's sample processing time and sensitivity limits of the XRF [29]. A newer (2006) system uses a robotic arm that can measure ~30 mm diameter sections of a swipe to capture an aggregate (non-imaging) "one-shot" measurement of a folded swipe in ~ one hour [30]. It is worth noting that the IAEA can detect alpha (i.e., ^{210}Po) or beta isotopes (i.e., ^{90}Sr and ^{99m}Tc) by screening the radioactive swipe samples with a gridded ionization chamber counting system. These samples are adhered to an adhesive carbon disc and measured for one hour in the counting chamber.

This ionization chamber system has a high collection efficiency and sensitivity within the millibecquerel range [25]. IAEA swipe samples are destructively analyzed in bulk or particle analysis once screening measurements are complete. The bulk analysis starts when the swipe matrix (cotton or cellulose) is burned in a furnace at 600^{o}C for four hours. The swipe matrix is dissolved and results in burned ash by adding small amounts of hydrogen fluoride and ultra-high purity nitric acid. IAEA places the dissolved swipe matrix's outcome into two solutions: spiked (^{233}U and ^{242}Pu) and un-spiked portions. Pure uranium and plutonium fractions are determined using a multi-step ion-exchange separation procedure to remove the sample matrix from interfering elements. Final measurements are achieved with an inductively coupled plasma mass spectrometry (ICP-MS) as plasma ionizes the fraction dilutions [25] [28].

Overall, for IAEA environmental swipe sampling, detecting and analyzing radioactive signatures quickly (~weeks) are common themes for almost all screening techniques. Inspectors may collect less than 10 swipe samples (~300 swipe samples per year) during their visit to a nuclear-declared site [31]. Upon collection, inspectors are unaware if these samples have trace amounts of uranium or plutonium. Only in-field dose rates are done before sample shipment using a handheld detector. Radioactive signatures obtained from these swipe samples occur after samples are received, screened, and analyzed at the IAEA Clean Laboratory and NWAL. Reporting bottlenecks can arise if there are more samples awaiting screening and analysis than results determined. In-field imaging techniques may be useful to the IAEA as a pre-screening method for radioactive material or high priority particle samples. Increased signal to noise ratio improves mass spectrometry analysis to isolate radioactive on the swipe samples.

An imaging detector capable of pre-screening swipe samples could reduce IAEA reporting bottlenecks, improve IAEA's technical capabilities, and enhance IAEA's readiness to safeguard and prevent nuclear nonproliferation.

In the IAEA 2018-2023 Long Term Strategy for Research and Development, a technology goal states "to develop and implement methods to detect signatures of nuclear activities in environmental samples ..." [32]. The research discussed in this dissertation offers an alternative to current methods used by the IAEA in analyzing bulk samples. The alternative method is the large-area, real-time, single-photon, event-counting digital autoradiography imager which may assist in prioritizing swipe sample screening. This imager of interest is called Ionizing-radiation Quantum Imaging Detector (iQID). This dissertation aims to enhance the iQID imager's ability to quantitatively measure samples with activities ranging from below 0.0001 Bq to 10^7 Bq. These activities range of swipe samples and hot cell swipe samples are similar to swipe samples but are less common. Safeguards application could adopt this imager if the imager can detect these activity ranges. Chapter 2 **below** will express details regarding the hardware, software, data processing, and performance characterization of iQID**.**

1.4.Digital Autoradiography and Technologies

The digital autoradiography mechanism of iQID is a vital topic to understand how the large-area iQID can image nuclear safeguard samples such as ESS. Autoradiography is the oldest technique used for determining and identifying activity distributions of environmental samples [28]. Autoradiography doesn't involve a source but generates radiation interactions that can be imaged by a detector. Historically, IAEA environmental samples may consist of radioactively hot particles released into the environment by nuclear events such as nuclear reactor accidents (i.e., Chernobyl accident fallout) or nuclear weapons [33, 34, 35]. Historically, radioactive particles were identified in autoradiography using a photographic film sensitive to radiation from beta particles (some alpha particles). Radioactive particles were placed on the film by a circular black spot with a larger size than the particle.

The black area's size corresponded to the activity or number of disintegrations present during film exposure [28, 34]. Radioactive particles could distribute evenly on the sample in which a darken area, rather than a circular spot, would be detected in the film. These black spots or radioactive particles can be localized and detached from the sample for subsequent analyses. Therefore, autoradiography is highly suitable for the pre-screening of samples. In film autoradiography, beta particles are the leading cause for black spots (i.e., activity distributions). Photon interactions influenced activity distributions if the black spots' activity was outside the maximum range of beta particles. In terms of alphas, large black areas may occur without an absorbing material between active material and film. However, most beta particles would mask the effects of alpha particles [34].

Environmental monitoring of airborne radioactive particles can use autoradiography based on novel equipment and methods implemented. Procedures for film processing and analyzing should automate air-borne samples for flexible and fast sample treatment. Film autoradiography advantageously can detect the particle nature of radioactive releases. However, disadvantageous characteristics of film autoradiography consist of long sample preparation and measurement time [34]. The introduction of electronic (digital) autoradiography significantly enhanced the autoradiography technique [28]. These imaging systems fall under the category of real-time digital imaging systems (RTDI), which provides an image of the radioactive particles during a relatively short time when compared to film autoradiography. In other words, RTDIs can replace conventional techniques for identifying radioactive particles. The advantageous characteristics of real-time imaging systems consist of faster methods, easy to determine the position of radioactive particles, and available results in real-time, so there is no need to process the image after exposure.

Two types of digital image systems, scintillator beta camera and silicon-based Bioscope detector, have widely been used in nuclear medicine to identify radioactive particles (U/Pu) in sediment samples [36]. The scintillator (0.3 mm thickness) beta camera emits light through a fiber optic faceplate. The photocathode receives emitted light and generates photoelectrons. Multichannel plates amplify the photoelectrons are emitted from the photocathode. In the camera, the event position and electric signal intensity relates to the incident ionizing particle's energy. The beta camera had a spatial resolution of 0.5 mm with a detector diameter of 40 mm.

On the other hand, the silicon-based Bioscope detector has a 0.3 mm thick double-sided perpendicular silicon strip sensor on both p and n sides (50 μm width). Energy deposited from the ionizing particle is proportional to the particle's kinetic energy as an activity distribution. The Bioscope detector has a sensitive area of 32 x 32 mm^2 and system resolution higher than 50 μm. Likewise, the electric signal is generated from the Bioscope detector using a self-triggering read-out data chip [36]. Overall, the beta camera had a higher sensitivity than the silicon-based Bioscope. The Bioscope detector required a longer counting time (4 times) than the beta camera despite the bioscope having a better spatial resolution.

Another previously reported digital autoradiography technique implemented phosphor and semiconductor array systems [28]. These phosphor image systems can localize radioactive particles from contaminated environmental sites. These images readily identify the location of radioisotopes in the object imaged. The semiconductor pixel array contains a europium-doped BaFBr scintillator with 25 μm resolution and a phosphor plate (20 x 25 cm). Luminescence is photo-stimulated via a HeNe laser and detected via a photomultiplier tube. Emission rates seen by the phosphor is proportional to the radioactivity [28]. The area of radioactivity is limited when imaging (i.e., autoradiography) on thin samples. Autoradiography quantitatively maps the thin object's spatial radioactive distribution (often a tissue slice in medical imaging) without the need of an outside radiotracer to induce radioactivity.

The technique of autoradiography has been widely used in medicine to add to cancer surgery. This dissertation's scope focuses on how implementing autoradiography as an imaging technique for safeguard applications.

Ideally, a digital autoradiography imaging system useful in safeguards for imaging ESS would need the following characteristics: high throughput, scalability, large area for imaging entire area of ESS, the capability of live imaging, single-event counting, and adequate imaging data storage. Several commercial off-the-shelf (COTS) imagers are available, but each has its drawbacks, hence the novelty of the research on iQID expressed in this dissertation [37]. Traditionally, digital autoradiography uses photographic films due to its high spatial resolution at a few microns and low cost. Alternative digital imaging technologies explored replacing film imaging for more image quantification and energy linearity, low sensitivity, limited dynamic range (~10^2), and long exposure times (~days/months) [38]. One technology is phosphor storage plates or photostimulable storage plates (PSPs) [39] [40], which passively accrue dose during sample contact with advantages such as large imaging area, high throughput, yet measures one sample at a time. PSPs can have disadvantageous performance due to upper saturation limits for increased activity and long measurement times. Also, PSPs have no capability for real-time imaging information or examining individual events or decays of short-lived isotopes, hence little ability to discriminate particles and energies. The iQID imager can achieve similar detection efficiency and much-improved alpha/beta discrimination as PSPs improve precise acquisition time and readout noise with real-time and list-mode processing. This dissertation will explore enhancements in iQID, such as imaging for higher-activity samples, beta/gamma discrimination based on event shape, size, intensity, and performance limitations in frame-rate, dynamic range, and event pile-up.

Another technology applicable to digital autoradiography is multiwire proportional chamber systems [41].

One example is an advanced COTS imager called Biospace Beta Imager used previously for biological samples. Some advantages include high discrimination between beta particles and other isotopes based on half-lives emissions and the shape of events and adequate data storage and processing with list-mode data. On the other hand, this imager is heavy (145kg,160cm tall) and requires careful sample preparation as samples are frozen and must be made on custom flat conductive Mylar slides making in-field safeguard sample imaging not ideal. Similarly, a micro-pattern gaseous detector good for alpha/beta discrimination imaging called the Beaver System could be applicable but is less portable/compact and less expensive than iQID [5]. Additional digital autoradiography technologies use beta camera [42] , microchannel plates [43] [44], and solid-state detectors [45] [46]. This dissertation will focus on the last two advanced technologies via an image intensifier and CMOS sensor, respectively, expressed further in the signal processing section of Chapter 2 **below**.

One example of a silicon counting detector commercial off-the-shelf (COTS) digital radiography detector is Widepix (14.3 x 14.3 cm^2) [47]. This new large area detector of 10 x 10 tiles of silicon pixel detectors (each of 256 x 256 pixels with a pitch of 55 μm) read out by Timepix chips. Widepix has promising characteristics such as a large area for ESS and good energy resolution. Still, the disadvantage of a limited frame-rate capability of 10fps is good for measuring beta particles and electrons low efficiency for gamma- rays [47]. iQID can handle up to 400fps at a reduced spatial resolution while leveraging its real-time frame parsing performance with USB 3.0.

A smaller cadmium-telluride (CdTe) imager, LAMBDA, has a higher count-rate capability and better gamma/ electron and energy discrimination than Widepix [48]. This imager is a potential solution for digital autoradiography in safeguards due to its high frame rate, large-area, real-time event processing, and high energy resolution.

However, LAMBDA is expensive and currently has an issue with blurring due to the distance between the window and detector, reducing the image planar spatial resolution, which is not desirable for safeguards application [48]. Additional improvements in a pixelated CdTe with a large area for safeguard samples and fast readout is a solid-state detector called HEXITEC [49]. As a reasonable comparison to iQID, HEXITEC is more expensive and has a smaller imaging area (unless tiled) but can achieve similar imaging performance as iQID. This dissertation will further mention HEXITEC as a benchmark performance comparison for iQID.

Real-time radioisotopes (RRI) imagers (Japan) are the last digital autoradiography imager applicable to safeguards [50]. Some advantages are little sample preparation and the same detector area as iQID (10 x 10 cm^2) based on similar hardware as fiber-optic plates, image intensifiers, and CCD. Unlike iQID, these RRIs are not COTS and integrates CCD frames by acquiring images two minutes at a time. Amongst the different applicable digital autoradiography systems, iQID is distinct because of the following performance characteristics: relatively inexpensive ($50K), real-time, single-event list-mode processing, high spatial resolution, large imaging area with small system footprint, and portable by inspectors (runs on laptop computer and short 12V power supply). The signal processing and characterized performance of iQID will be expressed in Chapter 2.

Chapter 2

Signal Processing and Characterization of scintillation-based iQID Imager

2.1 Introduction

This chapter will describe the full signal processing and mechanism of how the large-area iQID operates. As shown in **Figure 8,** the large-area iQID functions as a multi-step system encompassed by multiple hardware components, defining the detector's performance and limitations. One must understand the signal generation process of the large-area iQID and how certain imaging and post-processing modifications impact its radiation detection response. Later chapters will discuss changes to imaging and post-processing algorithms to adapt the large-area iQID to the safeguards field. This chapter will briefly introduce the signal-generation mechanism of the large-area iQID. The large-area iQID imager can find radioactive regions or particles of interest on ESS or other substrates due to its high spatial resolution. This high spatial resolution could improve the imager's implementation in safeguards for sample prioritization. The peer-reviewed journal article called "Characterization of Large-area iQID for Safeguards Application" contains the performance results of the large-area iQID [9]. This chapter will discuss further details regarding each hardware component of the large-area iQID.

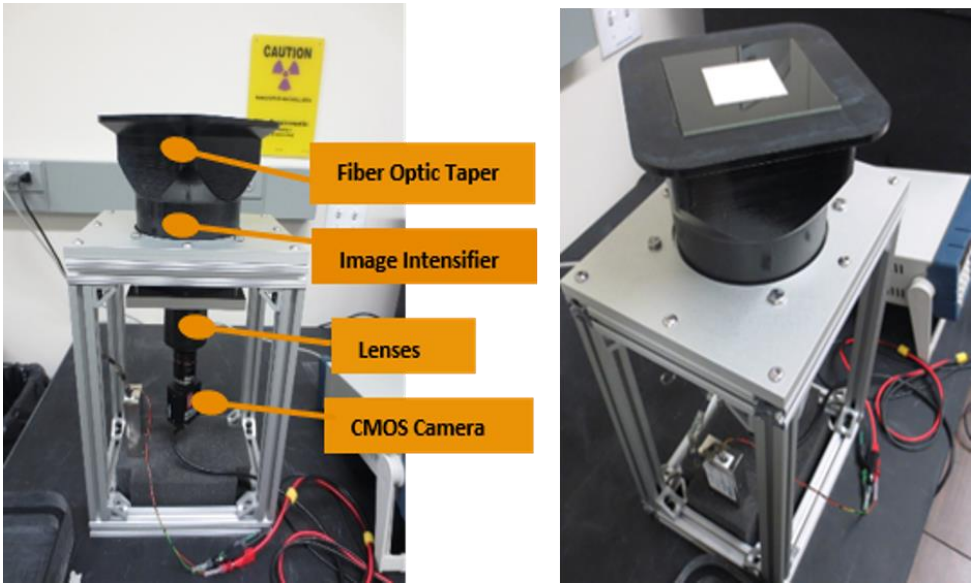

***Figure 8**: (Left): Photograph with labels identifying main large-area iQID system components. (Right): The large-area (10 x 10 cm2) iQID. The fiber optic taper is shown near the top with a smaller phosphor screen. [9].*

2.2 Signal Processing of the large-area iQID

2.2.1 Phosphor Screens and Scintillators

The first part of the system, which is in contact with the radioactive sample, is a scintillator or phosphor screen. Particle interactions of radiation such as alpha, beta photons generate light within the scintillator. Each radiation type produces scintillation light differently, as described above in Section 1.1 **above**. As shown in **Table 1**, different scintillators and phosphor screens can be used on the large-area iQID to maximize signal-to-noise for different particle types and energies. The large-area iQID used ZnS:Ag scintillator for the alpha measurements due to its high light output for alphas and low sensitivity for high energy betas and gammas. ZnS: Ag (EJ-440, Eljen Corporation) contains a 25 µm-thick phosphor layer deposited on a 250 µm-thick transparent polyester plastic sheet.

I did not use screens with 100 µm-thick plastic layers despite their availability and improved spatial resolution. For beta/gamma measurements, a gadox-based phosphor screen (Gd_2SO_3:Th), BioMax TranScreen LE (Carestream Health), was used due to its ability to detect low-energy beta particles. TranScreen LE has a total thickness of 102 µm (2 µm thick cover, ~50 µm phosphor layer of gadox, and ~50 µm plastic base). Properties of the phosphor screens used during large-area iQID imaging is shown in **Table 1**.

***Table 1**. Properties of Phosphor Screens Used for Large-area iQID*

	Eljen EJ-440 (ZnS:Ag)	BioMax TranScreen LE (Gd_2SO_3:Th)
Est. Density (g/cm^3)	4.09	7.34
Thickness (µm)	700	102
Areal Density (mg/cm^2)	286	75
Decay Time (µm)	0.1-10	3
Light Yield (Photons/MeV)	52,000	32,000
Max Emission Wavelength (nm)	450	510
Index of Refraction at Max Wavelength	2.36	Not found
Size (cm^2)	10 x 10	10 x 10

Based on the light distribution generated from particle or photon interactions, iQID directly forms an irradiance pattern. The microchannel plate of the image intensifier amplifies the event's spatial distribution using electro-optical gain. The image intensifier's operation is vital to the performance of the large-area iQID and discussed further in Section 2.2.3 **below**.

2.2.2 Fiber Optic Taper

The next hardware component in the signal generation process of the large-area iQID is a fiber-optic taper. More frequently, fiber optic tapers are implemented as additional hardware to enlarge or reduce the system imaging area. The addition of fiber optic tapers occurs in imaging applications: X-ray crystallography, nondestructive testing (NDT), high-resolution x-ray imaging, and medical radiography. Fiber optic tapers are a fused block of parallel fibers (i.e., boule) pressed together in multi-fiber bundles through a series of fiber-drawing and assembly operations. Each boule is customized in a precisely controlled machine using heat and stretching to create its unique tapered design with minimal distortion and desired cross-section. The finished boule is asymmetrically hourglass-shaped, cut into two tapers, and polished, either flat or curved, based on the application. Overall, a fiber optic taper is a bundle of clad optical fibers used to transmit high-resolution images in which multi-fibers carry an elemental portion of the image [51].

The Incom fiber-optic taper used in the large-area iQID is a 105 mm^2 square front face and a 28.3 mm^2 round end face with an image magnification ratio of 3.7:1. The image magnification of a fiber optic taper is the taper's diameter ratio's large and small ends. The benefit of a fiber- optically coupled taper to CMOS camera, as in the large-area iQID, is expressed in terms of collection efficiency in **Figure 9**. A taper can operate as a magnifier or minimizer, considering light can theoretically pass through the taper in either direction. The fiber optic taper's large face, near the scintillator, generates the image from scintillation light. Next, this irradiance image is further transferred through the taper to its smaller end, optically coupled to the image intensifier. As for the large-area iQID, fibers within the taper carries individual portions of the irradiance image to pixels of other readout devices like CCD (charge-coupled device) or CMOS (complementary metal-oxide-semiconductor) [51].

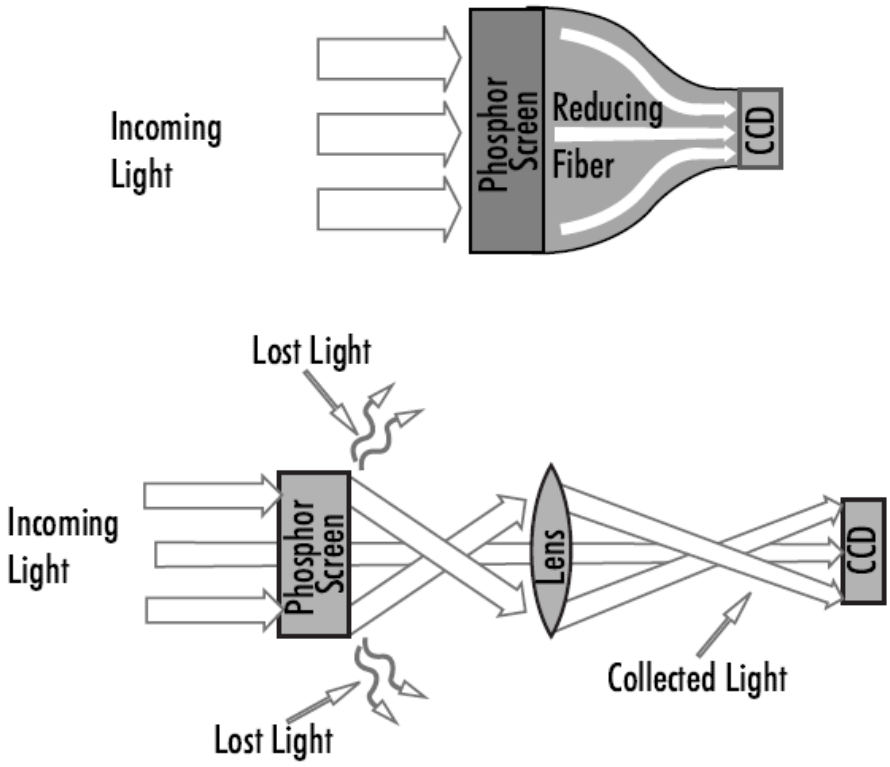

Figure 9: *Schematic demonstrating the difference in light collection efficiency between fiber-optically coupled CCD cameras (top) and comparable lens-coupled CCD cameras (bottom). The incident image from scintillation light is maintained and delivered to CCD more efficiently in systems fiber-optically coupled with tapers [51].*

The fiber optic taper's imaging performance in terms of scintillation light transmission can be maximized by individual cladding fibers to trap light by total internal reflection. Total internal reflection (TIR) (**Figure 10**) is the complete reflection of scintillation light between two transparent media in which incident light travels through the medium with a higher index of refraction if the incidence angle is greater than the limiting critical angle [52].

The taper's spatial resolution is mostly a function of fiber size at both ends and expressed in limiting resolution (lp/mm). One method for calculating the taper resolution is to divide 500 by the fiber diameter measured in mm [51]. For the large-area iQID, the taper's fiber size is 15-18 μm, which implies a resolution of approximately 28-33 lp/mm.

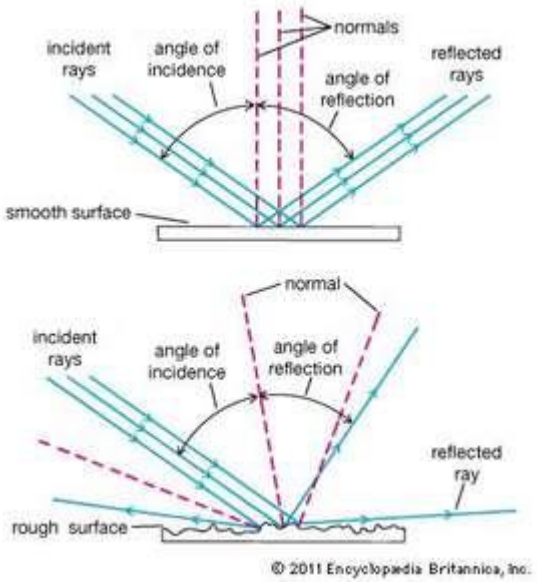

***Figure 10**: Schematic operation of total internal reflection [52].*

As light enters a fiber at an angle steeper than the TIR desired slope, the light will leak into the cladding, reducing the light collection efficiency. A stray-light absorber called an extramural absorption (EMA) can be added to the fiber optic taper to control the number of light leaks, not the cladding, or escapes from the fibers. The scintillation light transmits down a TIR taper based on the maximum incidence angle and numerical aperture (NA). Both are a function of the refractive indices of the cladding glasses and core. Scintillation light travels down fiber bundles to strike the inside of the fiber wall multiple times.

If the fiber optic taper acts as a minimizer, then the incident angle gets steeper with each successive reflection as light moves from the taper's large end to its small end. The incident angle is larger than the critical angle for TIR. This larger angle reduces the overall NA of the fiber optic taper. Equation 13 below, the fiber optic taper has an effective NA related to the fiber's geometry and establishes the taper's light transmission limit. Light traveling beyond this angle escapes through the fiber walls to the extramural absorber [51].

$$NA_{eff} = NA_{max} * \frac{D_{min}}{D} \qquad \textit{(Equation 13)}$$

where

$$D_{min} = smallest\ diameter$$

$$D = larger\ diameter$$

$$NA_{max} = \sqrt{n_1^2 - n_2^2}$$

$$n_1 = index\ of\ refraction\ of\ core\ (\sim 1.81)$$

$$n_2 = index\ of\ refraction\ of\ cladding\ (\sim 1.52)$$

A fiber-optic taper has an inherent performance disadvantage due to distortions and blemishes introduced during manufacturing. Despite improved manufacturing technology over the years for designing tapers with minimal distortions, absolute uniformity is not realistic. Tapers can have different types of blemishes such as spot (burned or broken fibers), line (chicken wire), and image distortions (i.e., shear and gross). These distortions can be offset using processing techniques and software acquisition and were mentioned for completeness but will not be further explored explicitly [51].

2.2.3 Image Intensifier

This section will describe the image intensifier or the next important hardware component of the large-area iQID. The large-area iQID has an image intensifier optically connected to the small end of the fiber optic taper previously discussed above. In the large-area iQID, the image intensifier is an evacuated microchannel plate electro-optical device used to increase visible light intensity in an imaging system, hence promoting enhanced image reproduction. This component has been historically useful in low light applications such as night-vision goggles. Therefore, techniques, such as an image intensifier, advantageous in enhancing image quality and resolution are vital when only a few photons are detected [53]. This dissertation will explore only modifications to the CMOS camera that can enhance the overall count-rate capability of the large-area iQID.

Image intensification can be achieved and controlled by two different hardware components, image intensifier and CMOS sensor, and their corresponding timing behavior. Such timing behavior is chosen based on the desired exposure time or defined as how long the aperture window is open and exposed to light. Two methods manipulate light exposure time for the large-area iQID. Either through gating with the image intensifier or via the shutter ratio (shutter/aperture time) of the CMOS sensor. Section 2.2.6. **below** will discuss further the shutter ratio of the CMOS sensor.

Gating provides an ultra-fast ability to switch the potential between the photocathode and input window of MCP from +80 V (OFF) to -180V (ON), as shown in **Figure *11*** [53]. Gating in the large-area iQID system is controllable by providing a low voltage TTL signal to the power supply to gate down to 1 μS windows. Despite gating, quantitative imaging with an image intensifier is essential by maintaining low light leakage into the readout device. Light leakage is not desired during imaging with the large-area iQID and refers to background light getting into the system.

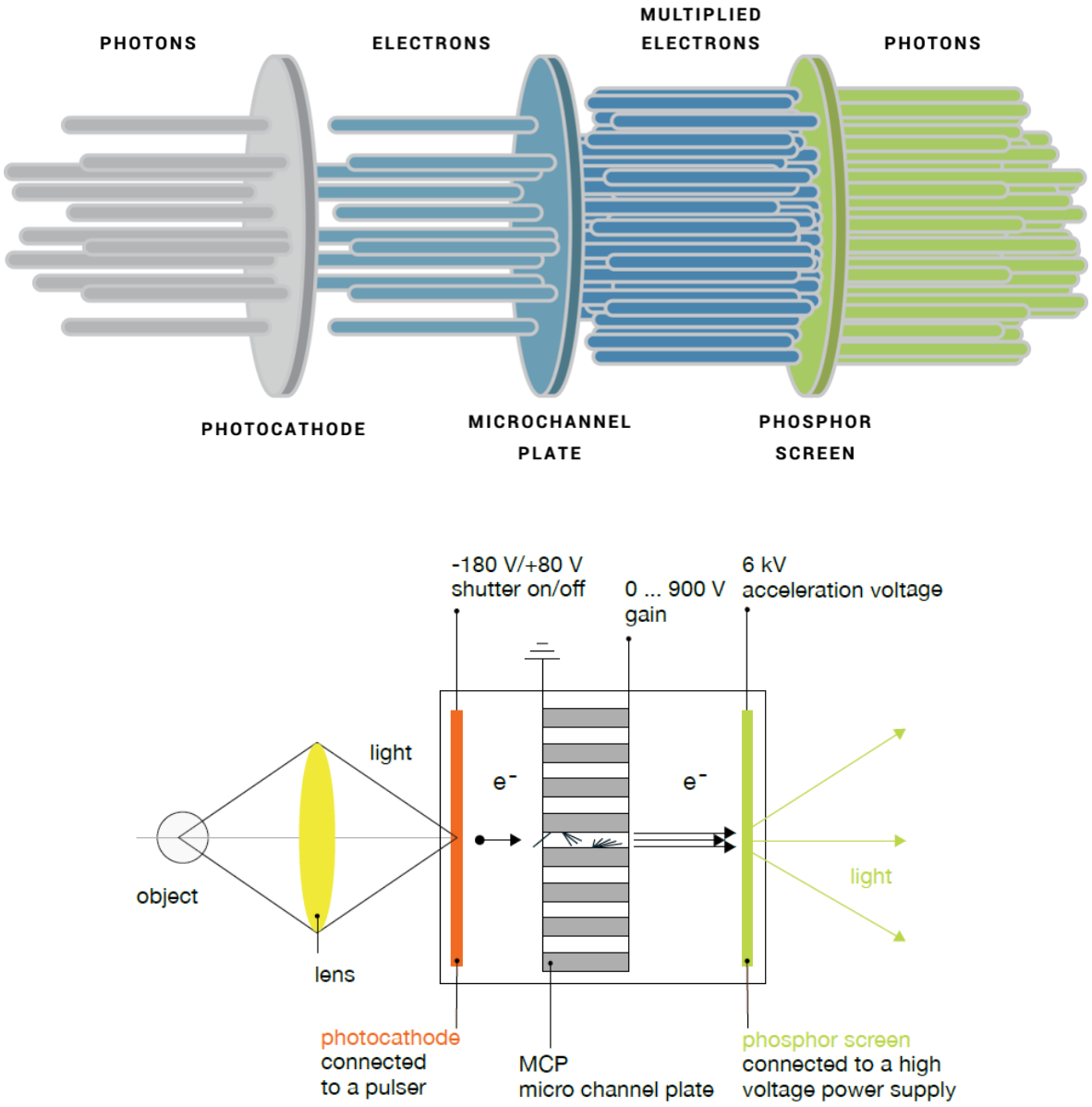

Figure 11: (Top): Signal processing schematic of an image intensifier in terms of an irradiance image pattern undergoing photoelectric absorption at the photocathode to create photoelectrons (electrons), emitting and exiting amplified photons at MCP and phosphor screen, respectively *[54]*. (Bottom): Schematic design of the how a gated image intensifier functions *[53]*.

The leakage rate corresponds to the proper synchronization of imaging components and how the light signal path travels throughout the iQID imager. Therefore, image intensification can occur at short exposure times on the scale of a few nanoseconds through gating, which is about six orders of magnitude faster than typically CMOS readout times.

As discussed further in Section 2.2.6 **below**, the readout device of interest for the large-area iQID is a CMOS sensor. Typical CMOS readout times are on the order of a few microseconds (ms) due to the time it takes to clear prior pixels before the next photoelectron accumulation. Shorter response times of 50 ns can improve the latency period of an image intensifier's photocathode or the time it takes to change from closed to open. The image intensification process can capture optical events missed by the CMOS sensor due to short decay times [53]. The image intensification process in a micro-channel plate (MCP) takes about 1-2 ns to detect and amplify photons, output the signal, and be ready for the next flux of radiation. Thus, the current limiting time factor to the image intensifier used in the large-area iQID is the phosphor screen, a decay time of ~1 ms. A P46 image intensifier could reduce the phosphor screen's decay time in a P43 type by 200 ns. However, this was out of the scope of this dissertation due to cost.

Previous studies have reported image intensifiers having low energy resolution as an additional performance limitation. A previous study states the reduced resolution could be due to multiple reasons: the depth of interaction (DOI) effect and attenuation (scattering and absorption) inside the scintillator, the Poisson statistics of photo-electric interactions, image intensifier gain variations, and use of a suboptimal photon-energy-estimation algorithm during image post-processing [8]. Chapter 4 of this dissertation explores how current hardware components control the performance of the large-area iQID. Additionally, Chapter 4 will investigate how optimizations in shutter exposure time can overcome current decay time limitations in the image intensifier.

An image intensifier's low energy resolution will be re-investigated in Chapter 5 to determine if the large-area iQID can distinguish between beta and gamma events using improved particle and energy discrimination algorithms.

2.2.3.A The Principal Operation of an Image Intensifier

In the case of the large-area iQID, the electron-amplification process of an image intensifier (Proxivision, MCP-Proxifier) starts by receiving an image of the irradiance pattern from the optically coupled small end of the fiber optic taper. This irradiance light pattern passes through the quartz faceplate to the entrance face of the image intensifier. The image intensifier in the large-area iQID has a 40 mm input and output diameter. **Figure 11** shows an image intensifier comprises three main components: the photocathode, a microchannel plate (MCP), and the phosphor screen. Each hardware sub-part is vital to understanding the electron-amplification process and its performance limitations regarding count-rate capability, spatial resolution, and particle and energy discrimination.

2.2.3.B Photocathode

The first hardware part inside the image intensifier is the S20 photocathode. The photocathode is responsible for receiving photons from the irradiance pattern and converting it to electrons. The S20 photocathode inside the image intensifier is on a quartz input window. The quartz material limits the photocathode's spectral response at shorter wavelengths (165nm) [55]. Gating at the photocathode allows for the time it takes to generate electrons from the irradiance pattern to be controlled. Controllable gating at the photocathode is vital to the gated image intensifier's performance because photoelectric absorption occurs at the photocathode.

This dissertation is investigating how a gated signal affects the count-rate capability of the large-area iQID. The count-rate capability of the large-area iQID may increase with a gated image intensifier. Shorter exposure times (~50 ns) can improve a photocathode's latency period, so the CMOS sensor's missed optical events are collected by image intensification [53]. The shutter time is highly dependent on other factors, such as the wavelength of the incident scintillation light, photocathode material, and the decay time of the CMOS sensor. Therefore, other methods, besides gating, can optimize the shutter time. In Chapter 4 **below**, this dissertation will demonstrate that longer decay times of CMOS sensors can also maintain count-rate capability through the unique signal processing of the large-area iQID. Thus, the larger imaging area, high spatial resolution, and longer decay times of CMOS sensor promote quantitative imaging (low spatial pileup) with large area iQID will broaden its relevance in other applications such as safeguards. Through characterization measurements, experimental quantitative imaging will be validated in Chapter 3 **below** and implemented to discriminate between particle types and energies of radiation interactions in Chapter 5 **below**.

2.2.3.C Micro-channel Plate (MCP)

The microchannel plate (MCP) is the second component of the image intensifier and acts as an electron multiplier. Photoelectrons are accelerated and multiplied as they enter the tapered MCP channels (**Figure 12**). Tapered MCP channels allow for photoelectrons to hit the MCP walls faster, hence releasing additional electron multiplication. The maximum possible gain of the MCP is the ratio between the channel diameter and the channel's total length.

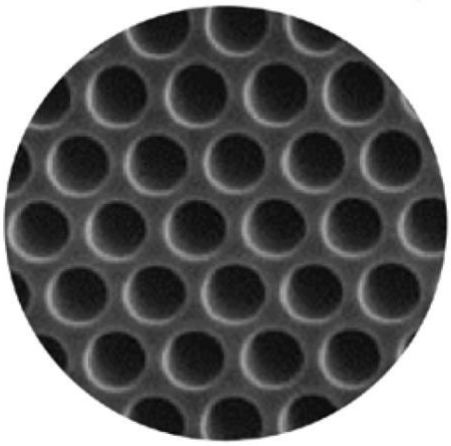

***Figure 12**: (Top) Microscopic image of a high resolution MCP with a thin 6 µm array of glass channels are visible [53]. (Bottom) Electron amplification process in single channel of MCP.*

Driven by bias voltages, each channel in the MCP operates as an independent electron multiplier. The MCP in large-area iQID consists of 2 plates in V-stack assembly with a bias voltage between input and output entrances of (+12 V) to (+1800 V), respectively, and a control voltage at (+5 V).

Therefore, due to the -200V to +12V bias voltage between the MCP photocathode and input window, these converted photoelectrons are amplified to the input window of the MCP channels. Likewise, due to the (+12 V) to (+1800 V) bias voltage within the MCP, photoelectrons are further accelerated by hitting the channel walls [53]. These high-energy photoelectrons produce multiple secondary electrons traversing across the MCP channel to create optical gains from 10^4 to 10^6 (depends on the number of MCPs) while preserving spatial information. This optical gain generates many electrons. These electrons are emitted out of the MCP's output window and accelerated under (+6 kV) bias voltage to the phosphor screen. iQID imaging generates an irradiance image from different types of radiation types. The MCP in iQID imaging is unlike PMT imaging detectors. Single radiation events cause photons to spread across an array of PMTs [6]. According to the manufacturer Proxivision, overall, the image intensifier in the large-area iQID has a limiting resolution of 24 lp/mm (0.042 μm) and a gain of 1,253,000 W/W at 480 nm. At this preferred wavelength of 480 nm (blue), the image intensifier of the large-area iQID has an approximate quantum efficiency of 16.5% and a spectral cathode sensitivity of 60 mA/W. Maintaining these settings and low resistance (20-30 MΩ) are essential to performance because the high gain of electronic signals can deplete electrons' micro-channel walls. The low resistance allows high strip currents the necessary time for a short reloading time during repetitive operations. MCP channels will be electron depleted if the MCP resistance is too high or if the gating frequency is too fast. As a result, images will have spatially reduced gains or inverted intensity distributions [53].

2.2.4 Phosphor Screen

The phosphor screen is the third component of the image intensifier, responsible for the optical output. The bias voltage (+6 kV) on the phosphor screen's input window accelerates the high-energy electrons exiting the MCP's output face at +1800 V. The phosphor screen's function is to absorb these highly accelerated electrons (6kV static voltage) and convert back to photons as an amplified irradiance image. The phosphor screen has a thin layer on the inner side of the output window. The phosphor screen is selected based on specific requirements: optimal brightness, decay time (the time it takes the phosphor light emission to decrease after excitation), and the emission range that matches the quantum efficiency curve of the CMOS sensor [53]. For the large-area iQID, the phosphor screen in the image intensifier is fiber-optic P43. P43 has a homogenous grain size and smoother and brighter light emission curve than P46 phosphor, made of yttrium aluminum garnet (YAG).

2.2.5 Lens

Double lens or tandem lens are coupled between the microchannel plate's phosphor and CMOS readout device. The double lens receives intensified photons collected on the phosphor screen and passes the image to the CMOS. Imaging with a single lens of focal length (f) consists of an object located at a distance (g) and a detector at an image distance (b). The relationship between the image and object distances can be related at first order by a well-known Equation 14 **below**.

$$\frac{1}{f} = \frac{1}{b} + \frac{1}{g}$$ *Equation 14*

The phosphor screen's transmission efficiency to the readout device for a single lens coupling system is calculated based on Equation 15 **below** where d is the lens diameter.

$$H = \frac{1}{4k^2(1+\beta)^2+\beta^2}$$ *Equation 15*

where

$$\beta = \frac{b}{g}; k = \frac{f}{d}$$

Imaging with a single high aperture 50 mm lens with F1.0 leads to just 5.9% transmission efficiency for a 1:1 imaging ratio. **Figure 13** shows a schematic of a lens imaging system.

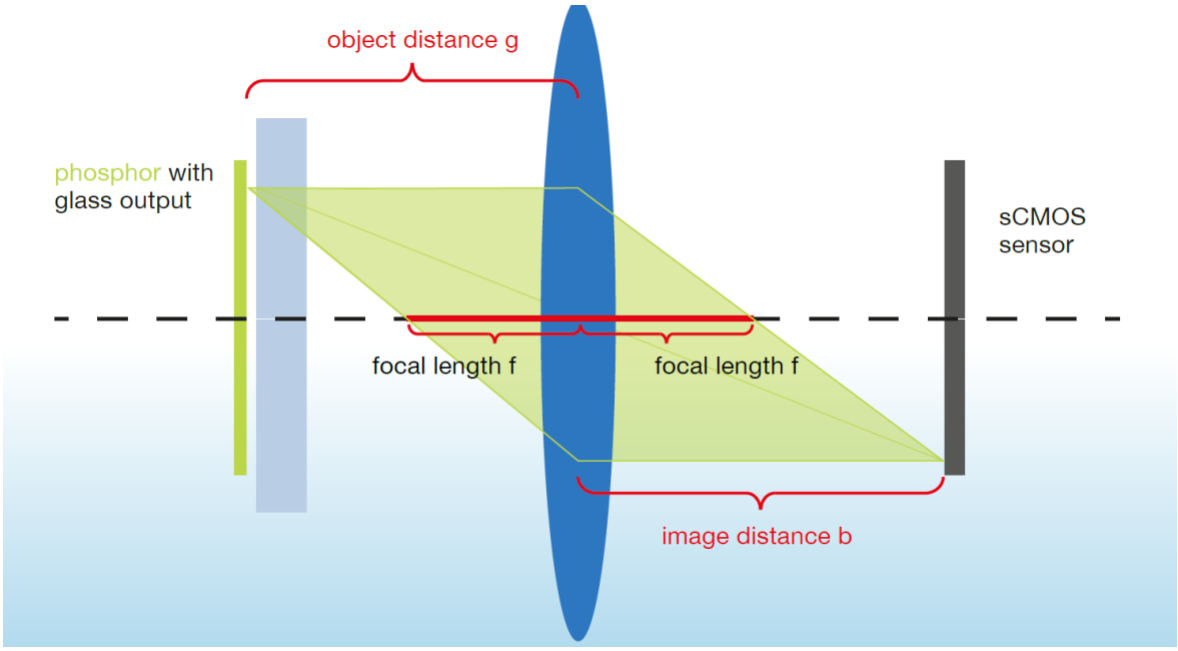

***Figure 13**: Schematic design of single lens optical imaging system with from a phosphor screen output window to CMOS readout device [53].*

On the contrary, a tandem lens system consists of an imaging path from the first lens (L1 = collimator lens) to the second lens (L2 = imaging lens) to infinity, as shown in **Figure 14**. A parallel bunch of photons originates from emitted photons emitted at L1. Focused on infinity, the L2 focuses the parallel bunch of photons to a single image point in the focal plane of the readout device's location.

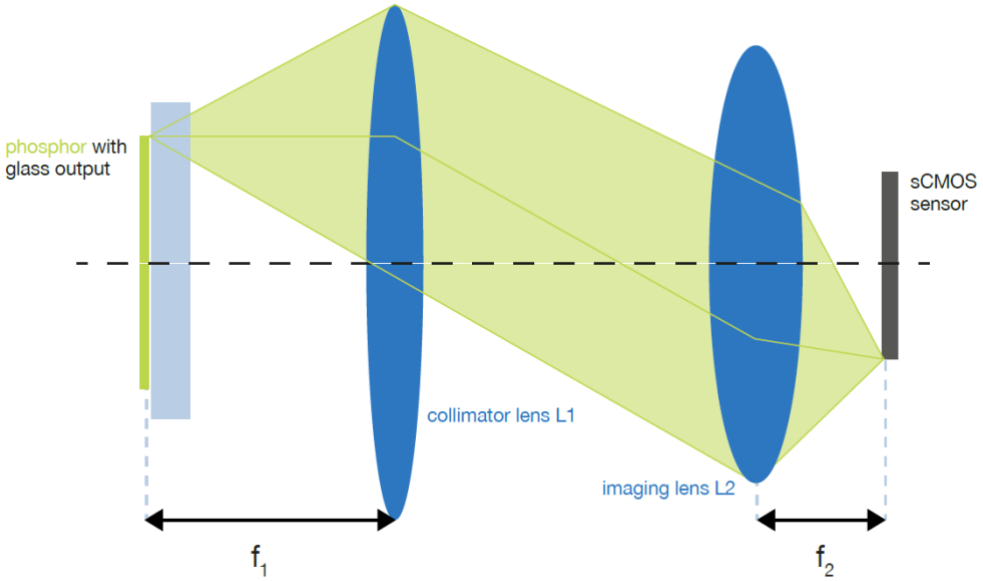

***Figure 14**: Schematic of tandem lens imaging system from the phosphor screen on the MCP to the CMOS readout device as in the large-area IQID [53].*

The image intensifier's phosphor screen has a glass output so that the lens can focus on the phosphor plane through the glass. Therefore, the transmission efficiency of a tandem lens system can be improved to 31.2% using the Equation 16 **below** with a tandem lens system of an F1.5 collimator lens of 100 mm focal length and F0.85 imaging lens of 53 mm focal length with d_1 and d_2 being the aperture of L_1 and L_2.

$$\eta = \frac{1}{4k^2\beta^2+\beta^2} x \frac{d_2^2}{d_1^2}$$ *Equation 16*

where

$$\beta = \frac{f_2}{f_1}; k = \frac{f_1}{d_1}$$

In other words, the optical signal conversion between a tandem lens imaging is optimized for a single imaging task within a narrow spectral range from the focal plane to infinity from infinity and to another focal plane. Adapting the proper imaging scale between the phosphor screen diameter and its image on the detector is ruled by the ratio of the two lenses' focal lengths. This optimization promotes high transmission efficiency and enhanced image quality with minimal signal contamination, such as imaging artifacts [53].

2.2.6 CCD/CMOS Sensor

The complementary metal-oxide-semiconductor (CMOS) camera is the hardware component related to the phosphor screen's brightness during illumination for the desired exposure time. A multi-tandem lens system optically couples intensified scintillation events from the image intensifier's phosphor output to the CMOS camera. The shutter ratio's exposure time is how long the shutter is open for constant and continuous illumination at -180 V(ON) until switching to +80V (OFF).

The CMOS sensor's performance is quantified by image resolution, dynamic range, frame rate, and count-rate capability. Some promising CMOS technology can be enhanced to create intensified image data rates more significant than the capabilities of CCD sensors in terms of sensitivity, resolution, speed, and dynamic range. The size of the CMOS image sensor is the effective area chosen to capture the image intensifier's phosphor screen output that dictates the imaging path scale of the multi-tandem lens system [53].

The 40 mm image intensifier in the large-area iQID is optically coupled to a 2448 x 2048 CMOS sensor (GS3-U3-51S5M-C, SN 15405699) that can achieve up to 75 frames per second (FPS) with a shutter up to 4 seconds. Based on the CMOS frame rate and source activity, multiple events counted as one event (spatial pileup) can occur within an image frame of the CMOS sensor. Therefore, the CMOS frame rate can be adjusted to minimize spatial pileup so that only events that interact within the same temporal window are collected on the image frame. This chosen frame rate is 20 FPS. Chapter 4 will investigate spatial pileup at higher frame rates and longer shutter settings.

The timing limitation of the CMOS sensor is the shutter or aperture window/time. The CMOS sensor in the large-area iQID has a global shutter mechanism in which each pixel is exposed to light simultaneously to ensure light collection starts and ends simultaneously for all pixels in the CMOS imaging sensor. All pixels' exposure stops simultaneously and transfers its charge to a non-photosensitive transistor while holds at the end of each row. Digitization occurs as analog-to-digital conversion (ADC) clocks through each sensor to digitize each row individually. This digitization decreases the detection of overlapped events.

On the contrary, delayed digitization also decreases the frame rate in half. A global clear eliminates any accumulated charge before the next exposure. In other words, every pixel is simultaneously exposed equally. This mechanism function is very beneficial when an image changes from frame to frame, which occurs with the large-area iQID. Overall, this global shutter mechanism is vital to the decay time (i.e., shutter time) of the CMOS sensor. Other parameters that play an essential role in the event rate of most photon-counting CCD/ CMOS detectors are decay times of the scintillator/phosphor screens, CMOS sensor frame rate, and cluster size or the number of pixels per cluster. Previously, CMOS image transfer time or frame overhead time (~ 45 μs per frame) was negligible in iQID imaging due to the maximum shutter time for each pixel set to 1/FPS [6].

In this dissertation, count-rate capability and spatial pileup of LAiQID will be investigated further (Chapter 4).

2.2.7 Image Processing

Once the irradiance pattern is amplified and imaged onto a CCD/CMOS camera sensor, the resulting image and corresponding data are saved into a list-mode file for further post-processing. Post-processing analysis can occur due to high-performance graphics processing units (GPUs) by NVIDIA and multi-core computer processing units (CPUs) for real-time event detection and location estimation. This mechanism compresses data to a smaller size to account for computer storage/memory for later use but contains relevant information for further processing. This list-mode file includes 2D position estimate, timestamp, summed pixel values within an event cluster or cluster intensity, area covered by event clusters or cluster area, the shape of cluster events, or eccentricity, and other associated event pixels. LABVIEW is an acquisition software coupled to the CMOS sensor to acquire the raw images for further processing. Image data from the MCP's phosphor screen is required to be appropriately synchronized with the image acquisition software LABVIEW to capture the intensified image on the CMOS sensor. ***Table 2*** shows the imaging parameters set in LABVIEW. During post-processing, a separate 2D image can be generated from the list-mode file to estimate each event cluster's centroid in real-time, based on pixel values that have reached a certain imaging threshold. This entire post-processing mechanism is referred to as frame parsing. As shown in **Figure 15**, an example of an event cluster collected within a 21 x 21-pixel image until the entire 2448 x 2048 CMOS image is processed and saved as a list-mode file.

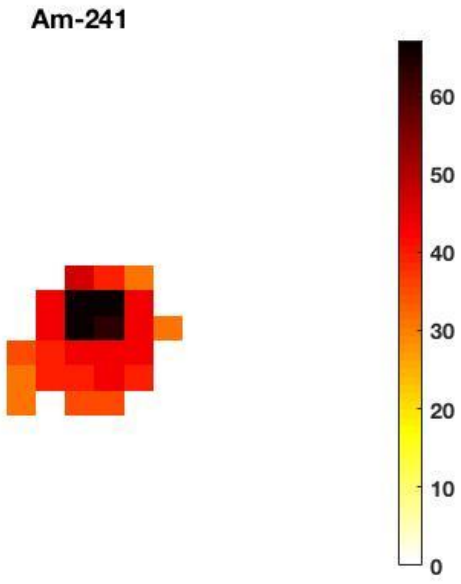

***Figure 15**: Example 21 x 21 event cluster large-area iQID image of a Am-241 gamma source. Imaging parameters were set a nominal setting of a threshold of 60, intensifier gain of 0.07V, CMOS shutter time of 49ms.*

***Table 2**: Current Operating Settings of LA-iQID*

DAQ Parameter	Value
CCD Frame rate (fps)*	20
Shutter (ms)*	49.7497
CCD gain (dB)*	47.9943
Cluster size*	21 × 21
Filter type	Median 3 × 3
CCD pixels	2448 × 2048
Threshold*	55 to 85

The frame parsing algorithm consists of four main steps that will be discussed in detail here. Firstly, raw CCD frames are acquired from radiation interactions within the scintillator above the required imaging threshold. This dissertation sets the minimum threshold necessary for an event to be collected to 60 pixels. Secondly, a 3x3 median-filter is used to remove any "noisy", "dead," or small-island pixels from the CMOS sensor out of the image. Thirdly, this filtered image with individual particles is identified as event clusters based on a connected component labeling algorithm. This dissertation describes an event cluster as 4 pixels connected with an intensity of more than 10 pixels using the MATLAB connected component algorithm. Lastly, necessary information, as described above, is saved to a list-mode file for further processing. These list-mode files allow for post-processing analysis based on its performance in terms of spatial resolution, energy response, minimum detectable activity (MDA), detector uniformity, and count-rate capability. Chapter 3 **below** will discuss these results.

Additional studies regarding an advanced frame parsing algorithm have occurred, which provided flexibility for event estimation and removed noisy pixels from the central spot background from XX1332 image intensifiers [8].

Chapter 3

Characterization of LA- iQID

This chapter will describe the full characterization measurements conducted on the large-area iQID to investigate its baseline performance based on the current hardware components. Characterizing the large-area iQID based on specific metrics will determine its applicability to the safeguards field. Characterization metrics are spatial resolution, energy response, minimum detectable activity, detection uniformity, and count-rate capability. This chapter will present its methods, notable findings, and significant conclusions useful for each metric. Therefore, these results will quantify the performance tradeoffs of the large-area iQID. As imaging parameters change, such as the CMOS aperture time, these characterized baseline measurements will be used to determine which changes had the most significant impact on the detector's performance. These metrics will be revisited further in Chapters 4 and 5 to quantify imaging limitations in count-rate capability and how different radiation interactions such as alpha, betas, and photons response in the detector, respectively.

3.1. Spatial Resolution-Line Spread Function

In terms of digital imaging, spatial resolution is a measure of the smallest object that can be resolved by the sensor or imager of interest or the linear dimension of the ground area represented by each pixel for the instantaneous field of view (IFOV) of the sensor [56]. In other words, spatial resolution consists of the number of pixels used to reconstruct an image in which images with higher spatial resolution have a larger number of pixels than those of lower spatial resolution.

3.1.1. Methods

This dissertation estimated the intrinsic spatial resolution of the large-area iQID by measuring the line spread function (LSF) using commercial off the shelf (COTS) slits (LenoxLaser). First, the MATLAB post-processing script read in the centroid image of the irradiated slits. Centroid calculations via MATLAB estimated each alpha event's interaction location. A radon transformation or projections of the image matrix as a set of line integrals computed the best rotation angle over 360^{o} with fine estimation. Once the best rotation angle is calculated, the LSF from the slit is calculated. The metric for spatial resolution was the full width at half maximum (FWHM) of the LSF, determined by a least-squares Gaussian fit as previously done for a similar system [6]. The pixel size was modified to 60 μm (effective pixel size of LAiQID).

Measurements with the LAiQID were conducted for both alpha and beta imaging modes and their corresponding imaging parameters are displayed in **Table 3**. Alpha spatial resolution measurements used a ZnS:Ag scintillator and both 5 μm tungsten and 10 μm glass slits. On the other hand, TranScreen LE phosphor screen and 10 μm glass slit were used for LAiQID beta spatial resolution measurements. All alpha and beta imaging setups consisted of three pieces: scintillator, slit, and source. The scintillator or phosphor screen was directly on the fiber-optic taper window. Next, on top of the scintillator, a 115.1 nCi ^{239}Pu alpha calibration source (*Eckert & Ziegler Isotope Products, Inc.)* or a 9 μCi ^{14}C beta source was placed on the chosen slit. Based on their material composition and thickness, slits were chosen for alphas (^{239}Pu) to penetrate and attenuate betas (^{14}C). A 5 μm (slit width) x 3 mm x 50 μm tungsten and 10 μm (slit width) x 3 mm x 0.2 mm glass slits were selected.

3.1.1. Results

Table 3 shows alpha and beta spatial resolution results from the 5 µm tungsten slit and 10 µm glass slit. The alpha spatial resolution is 94.7 µm LSF FWHM with the 5 µm tungsten slit and 25 µm thick ZnS:Ag phosphor layer scintillator. Similarly, the alpha spatial resolution with the 10 µm glass slit is 94.9 µm (**Figure 16**). **Figure 16** also demonstrates an irradiated slit with a ^{239}Pu source. The best rotation angle of the radon transform was 2.075° for imaging.

***Table 3**: Results of alpha and beta spatial resolution measurements for each slit.*

Source	Phosphor	Slit Material	Slit Width [µm]	LSF FWHM [µm]
^{239}Pu	ZnS:Ag	Tungsten	5	94.7
^{239}Pu	ZnS:Ag	Glass	10	94.9
^{14}C	TranScreen LE	Glass	10	142.0

The effective pixel size for spatial resolution measurements was 60 µm based on the CMOS pixel size magnification. The spatial resolution for alphas is approximately ×1.5 of the effective pixel size. A ^{90}Sr/^{90}Y source, which emits high-energy beta particles and bremsstrahlung, did not provide an image with adequate contrast with the available slits. ^{14}C, which emits lower-energy-beta particles, was measured at 142.0 µm LSF FWHM. No uncertainty calculations were conducted for these spatial resolution measurements.

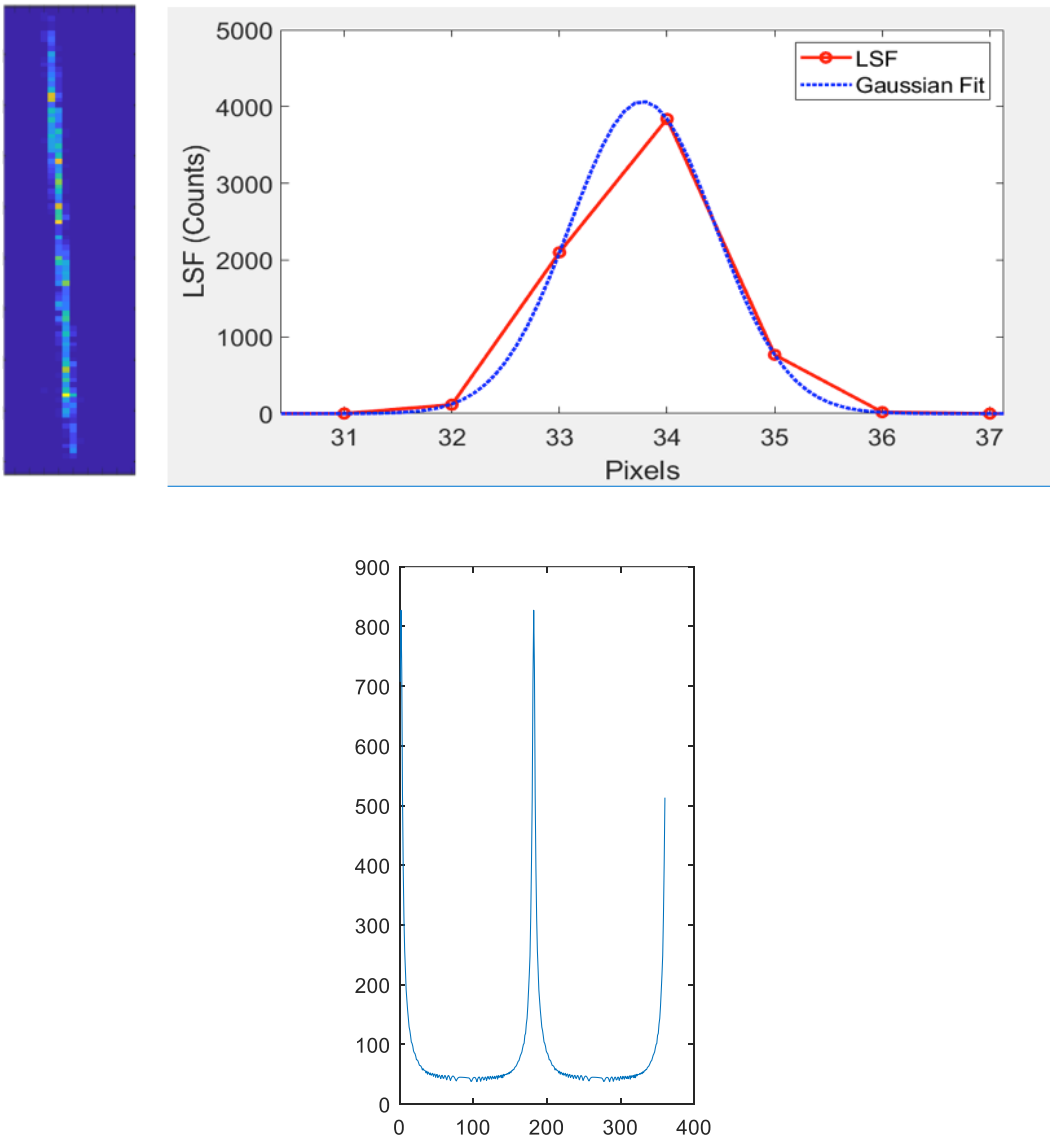

***Figure 16**: (Left) An image of irradiated 10 µm glass slit with ^{239}Pu source. (Right) LSF plot (red) with a Gaussian fit (blue). (Bottom) Radon transformation over 360^{o} during alpha imaging.*

3.1.2. Discussion

Slit measurements and corresponding LSF FWHM data demonstrate differences in phosphor and plastic substrate thicknesses between ZnS:Ag and TranScreen LE, which may account for resolution differences; beta particles also travel farther than alphas, which reduces spatial resolution [37].

3.2. Energy Response

3.2.1. Methods

This dissertation measured the energy response of the large-area iQID for three isotopes: ^{239}Pu, ^{241}Am, and ^{14}C (**Figure 19**). ^{239}Pu primarily undergoes alpha decay, emitting a 5.2 MeV alpha particle. ^{14}C and ^{241}Am were both measured during beta/gamma imaging modes of LAiQID. For these measurements, ^{241}Am emits a 60 keV gamma-ray and ^{14}C is a pure beta emitter that emits a 50 keV beta particle. ^{241}Am and ^{14}C sources were measured individually on the large-area iQID with the TranScreen LE phosphor screen, whereas alpha events from ^{239}Pu were measured using ZnS:Ag. The fiber optic taper's imaging performance in terms of scintillation light transmission can be maximized by clad individual fibers to trap light by total internal reflection (TIR). Total internal reflection (TIR) is the phenomenon of complete reflection of scintillation light between two transparent media in which incident light travels through the medium with a higher index of refraction if the incidence angle is greater than the limiting critical angle [52]. TIR is further described in **Figure 17**. The spatial resolution of the taper is largely a function of fiber size at both ends and expressed in terms of limiting resolution (lp/mm). One method for calculating the taper resolution is to divide 500 by the fiber diameter measured in mm [51]. For the large-area iQID, the taper's fiber size is 15-18 μm which implies an image resolution of approximately 28-33 lp/mm.

The fiber optic taper's imaging performance in terms of scintillation light transmission can be maximized by individual cladding fibers to trap light by total internal reflection. Total internal reflection (TIR) (**Figure 17**) is the complete reflection of scintillation light between two transparent media in which incident light travels through the medium with a higher index of refraction if the incidence angle is greater than the limiting critical angle. The taper's spatial resolution is mostly a function of fiber size at both ends and expressed in limiting resolution (lp/mm). One method for calculating the taper resolution is to divide 500 by the fiber diameter measured in mm [51]. For the large-area iQID, the taper's fiber size is 15-18 μm, which implies a resolution of approximately 28-33 lp/mm.

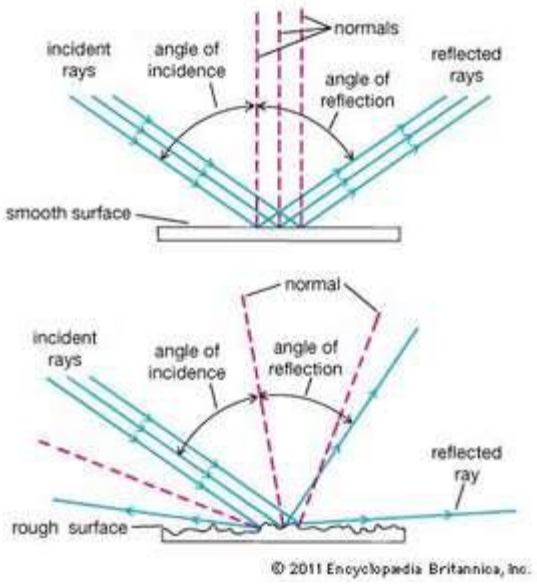

***Figure 17**: Schematic operation of Total Internal Reflection (TIR)*

Summing and histogramming event clusters within a 21×21-pixel region generates response graphs for an extensive collection of events. **Figure 18** is an example image of an event cluster for alpha and beta/gamma interaction. The intensifier gain is 0.05 V for alpha imaging and significantly lower than beta/gamma imaging (0.7 V).

The lowered intensifier gain adjusts the dynamic range such that detected highly energetic alpha particles occur within the dynamic range of the CMOS sensor. A small signal from beta and gamma events at this lower gain setting provides alpha measurements with low background.

3.2.1. Results

As shown below in **Figure 19**, ^{14}C and ^{241}Am have similar responses; ^{239}Pu (α source) has a distinct energy signal. TranScreen LE phosphor screen collimates alphas from ^{241}Am during beta/gamma imaging modes due to alphas' low incidence angle. On the other hand, the TranScreen LE phosphor screen doesn't collimate betas from ^{14}C and gammas from ^{241}Am.

3.2.2. Discussion

Emitted betas (^{14}C) and gammas (^{241}Am) have similar energy responses (**Figure 19**). These response similarities may make beta/gamma discrimination difficult with the large-area iQID. Typically, particles emitted from a radioactive source are detected based on their incidence angle. If the particles' angle is lower than normal incidence (90°), then the particles' path is more extended than incident particles along with normal incidence. Therefore, these particles with lower (less than 90°) incidence angle have a lower energy resolution because particles lose energy through interactions with air and absorbing layers. Collimation can improve energy resolution to identify radionuclides [57].

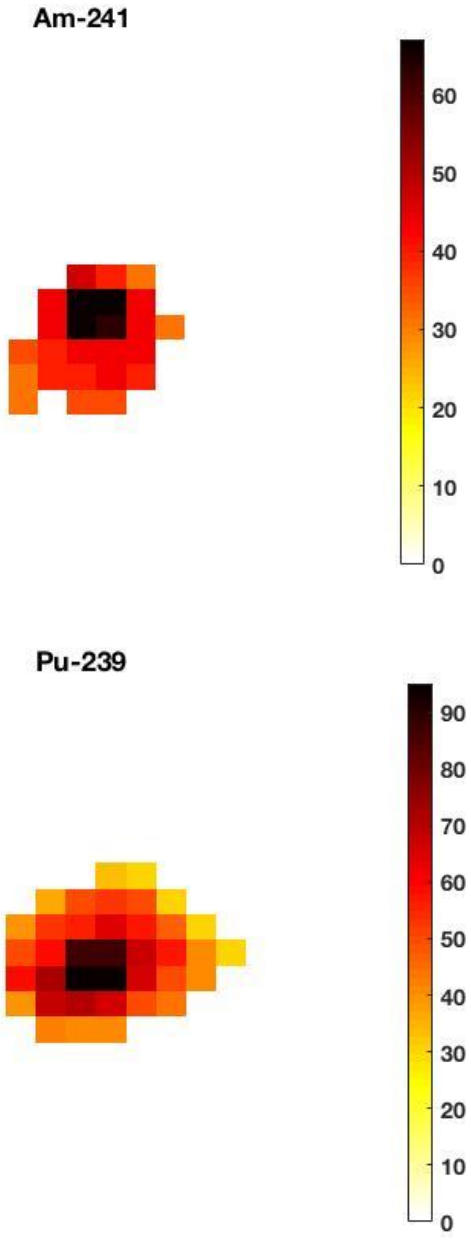

***Figure 18**: Example of one event cluster image (21 x 21 pixels) for beta/gamma and alpha interactions of ^{241}Am (top) and ^{239}Pu (bottom), respectively.*

Beta imaging of ^{14}C nor gamma imaging of ^{241}Am used a collimator. Instead, these sources were placed directly on the TranScreen LE phosphor screen and relied on its high sensitivity for low beta collimation. The lack of collimation degraded the low energy betas' energy response from ^{14}C (average ~50 keV) and low energy gamma from ^{241}Am (~60 keV). Post-processing data cuts may improve the large-area iQID imager's ability to discriminate between these emissions (Chapter 5). ZnS:Ag scintillator can easily differentiate the distinct response of alphas from betas and gammas. This alpha response is due to collimated ^{239}Pu alphas (~ 5 MeV) and ZnS:Ag scintillator's high light output for alphas and low sensitivity for high energy betas and gammas. Alphas were not measured in beta/gamma mode as betas/gammas do not register as events in alpha mode imaging (0.05 V intensifier gain). Therefore, alphas provide a saturating signal in beta/gamma imaging mode which makes their presence easy to discriminate from betas/gammas. This result is further expressed in Dr. Miller et al study that demonstrates how alpha mode imaging in iQID is blind to betas/gammas [58].

3.3. Detection Uniformity

3.3.1. Methods

To assess the detection efficiency's uniformity across the imaging area, a ZnS:Ag (ZnS) scintillator was exposed to the overhead lights and then imaged on the iQID system for 1 minute. The post-processing software (LABVIEW) of large-area iQID integrated raw CCD frames together. Typically, the large-area uses frame parsing or list-mode imaging. This experiment did not use this method because 'counting' rates would have been too high for the frame parsing algorithm.

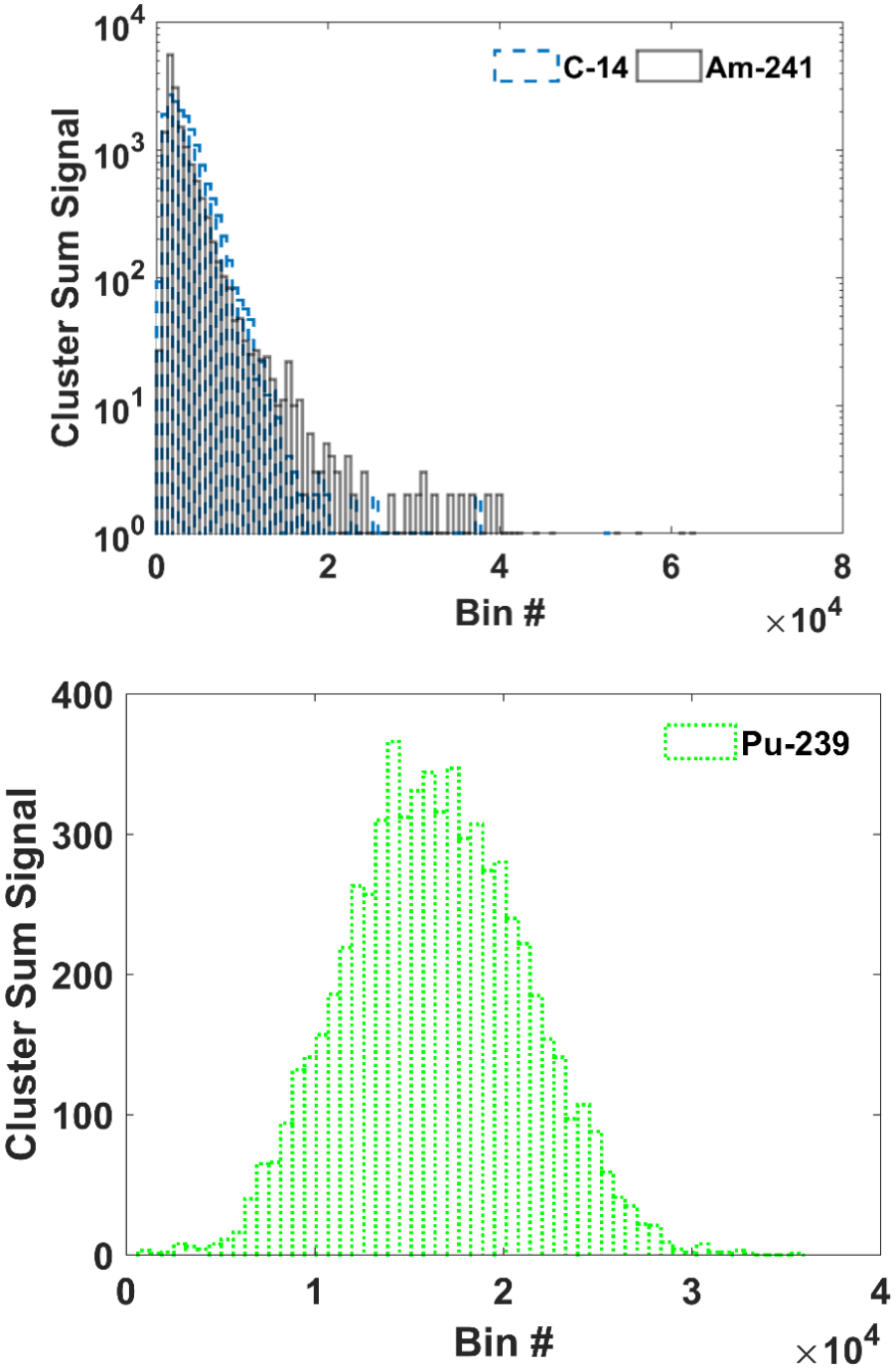

***Figure 19**: (Top): Energy response from ^{14}C (blue) and ^{241}Am (black) at 0.7 V. Y-axis on a log scale with same bin widths of 630. (Bottom): Energy response from ^{239}Pu (green) at 0.05 V for alpha imaging. Bins are equal to the sum of the 21 x 21 cluster signal (each pixel ranges from 0-255, so max value is 112,455).*

3.3.2. Results

Figure 20 represents the detection uniformity results of the large-area iQID. The overall light collection efficiency dropped by a factor of two from the center to the edge of the taper. A similar system that didn't include a fiber optic taper had much better uniformity [7]. Section 3.3.1 **above** further investigated the light collection efficiency drop via measurements of four beta sources at different locations on the scintillator.

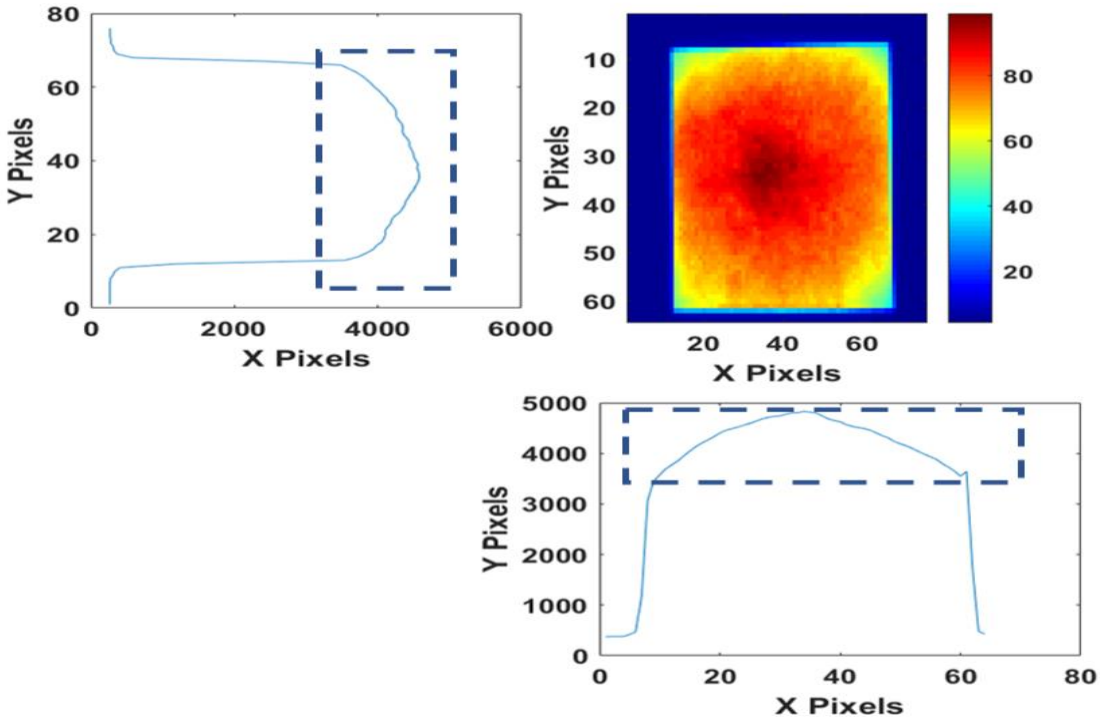

***Figure 20**: (Top-right) Graph showing the uniformity of the large-area iQID with a ZnS scintillator exposed to room lights. Line profiles are from the horizontal (top-left) and vertical (bottom-right) centers of an image. X-axis and Y-axis labels for all graphs represent the pixel intensity values. The dashed box in the line profiles display the location of the uniformity graph. Collection efficiency for LAiQID drops by about two from the center of the taper to the edge.*

3.3.3. Discussion

Tapers typically operate as a light guide by transferring light collected by the scintillator. The large-area iQID imager transmits collected light to the image intensifier and CMOS camera (for iQID imaging). The bundle of clad fibers that encompasses the taper transfers the elemental portion of the high-resolution irradiance image via multi-fibers. The taper's threads carry elementary parts of the image to the CMOS camera's pixels. The scintillator collects light or irradiance images before reaching the CMOS camera. Blurring occurs across the scintillator's area when light enters a fiber at an angle steeper than the total internal reflections' desired slope. As a result, light leaks into the cladding and reduces light collection efficiency [51].

Figure 20 demonstrates the non-uniformity in the collection efficiency of the large-area iQID. This reduction in light collection efficiency is likely from light leakage and variations in the fiber-optic taper and blurring across the ZnS scintillator. The non-uniform light collection across the fiber-optic taper could be corrected using a flat-field correction. However, this dissertation did not conduct a flat-field correction because the measured count-rates and absolute efficiencies weren't affected much by the non-uniform overall light collection efficiency. These results are demonstrated in **Figure 21;** absolute efficiencies of four button sources were measured on different taper parts to validate results. Absolute efficiencies, as opposed to integrated light, didn't change from center to edge of the scintillator because the intensity scintillation flashes were brighter enough to pass the lower detection threshold. For LAiQID, the lower detection threshold is the number of pixels above threshold (60 pixels).

3.4. Detection Efficiency & Minimum Detectable Activity

3.4.1 Methods

This dissertation calculated the minimum detectable activity (MDA) of the large-area iQID imager. Simultaneously, the large-area iQID imaged four beta-emitting button sources (^{14}C, ^{99}Tc, ^{210}Pb/^{210}/Bi, ^{90}Sr/^{90}Y) 4-hours. Absolute efficiency and MDA (used standard Currie equation) were the metrics for characterization. In the standard MDA Currie equation (numerator of Equation 17 below), minimum number of counts detected from source occurs at a false-positive rate no greater than 5%. This false-positive rate is possible when operating at a critical level $L_C = 2.326\sigma_{NB}$ [16].

$$MDA = \frac{4.653\sigma_{N_B} + 2.706}{f\varepsilon T} \qquad \textbf{Equation 17}$$

Equation 17 **above** represents the minimum detectable activity with a false-positive rate no greater than 5%. Additional factors to consider include uncertainty in the background σ_{N_B} , radiation yield per disintegration f, absolute detection efficiency ϵ, and counting time per sample t. Characterized ^{239}Pu results from **Figure 19** assisted in comparing beta and alpha MDA results. Computed absolute efficiency used background-subtracted image data and ROI analysis for each source. To help in these calculations, the source manufacturers provided the known number of betas escaping all pure beta emitters (^{14}C, ^{99}Tc, ^{210}Pb/^{210}/Bi, ^{90}Sr/^{90}Y) into 2π per second. Proper decay corrections ensured the accurate number of betas emitted in 2π geometry.

3.4.2 Results

Figure 21 below shows the sources' image, and **Table 4** below shows the efficiency and MDA results. The lower background rate for alphas means lower MDAs than for betas and gammas.
As the energy of the beta particles increases, so does the absolute efficiency. The highest achievable absolute efficiency for the current large-area iQID is 50% for a 2π geometry.

3.4.3 Discussion

Based on the sources evaluated for this study, the lowest efficiency was measured for ^{14}C, which emits the lowest-energy betas (~50 keV average, 156 keV end-point) and no gamma x-rays. The low absolute efficiency for low energy betas demonstrates the large-area iQID's low sensitivity for detecting low energy betas. This result supports the common findings as MCNP modeling results (Appendix) validated this same conclusion. Based on the manufacturer BioMax, TranScreen LE has a high sensitivity towards detecting low-energy beta particles. One exciting finding is selecting TranScreen LE as the scintillator did support the large-area iQID's ability to improve the absolute efficiency of low-energy betas. This finding supports all beta imaging results.

For example, ^{210}Pb emits low-energy beta particles (~63.5 keV average energy, 63.5 keV end-point), and a low-yield 46.5 keV (4.25%) gamma-ray. The high absolute efficiency (43.6 %) result from $^{210}Pb/^{210}Bi$ is likely due to the gamma-ray's detection of all summed energy events. Moreover, ^{210}Pb is in secular equilibrium with another beta-emitter, ^{210}Bi (0.389 keV average, 1.1614 MeV end-point), and this isotope provides most of the detected signal.

Next, ^{99}Tc is the next-highest pure beta emitter and with an efficiency of ~ 31%. ^{99}Tc emits a low/medium- energy beta particle at 294 keV. Modeling results (Appendix) show as the detected beta particle's energy increases, so does the theoretical efficiency of the large-area iQID.

These trend results are validated by the absolute efficiencies for ^{14}C (156 keV, 10%), ^{99}Tc (293 keV, 31%), and $^{90}Sr/^{90}Y$ (48%, 546 keV to 2280 keV).

***Table 4**: Alpha and Beta MDA results of iQID imager, average background counts per area, and MDA measurements for several isotopes*.

Source	Absolute Efficiency [%]	End-Point Energies [MeV]	MDA [Bq/cm^2]	Average [CPM/cm^2]*
^{14}C	10.1 ± 0.7	0.156	0.14	-
^{99}Tc	30.9 ± 0.6	0.292	0.05	-
^{210}Pb /^{210}Bi	43.6 ± 1.2	0.0635/1.1614	-	-
$^{90}Sr/^{90}Y$	47.6 ± 0.6	0.546/2.27	0.02	-
^{239}Pu (α)	50.0 ± 0.1	~5	0.004	-
Background (α)	-	-	-	0.011 ± 0.0014
Background (β/γ)	-	-	-	1.76 ± 0.02

*CPM=counts per minute.

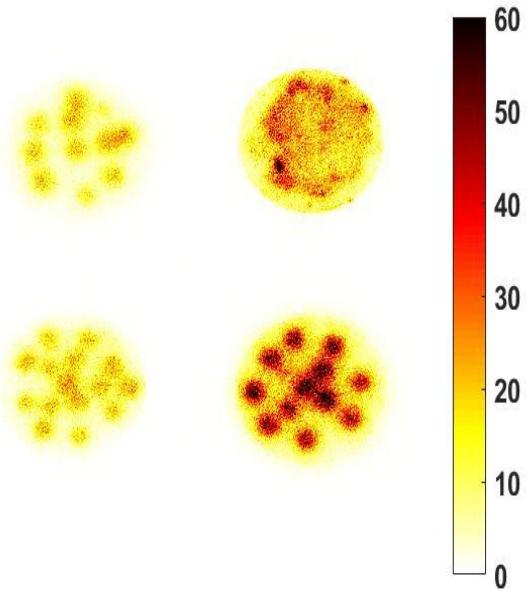

***Figure 21**: Image of four beta-emitting button sources measured on the iQID system (four hours). Radionuclides starting at top left and naming clock-wise are ^{210}Pb /^{210}Bi, ^{14}C, $^{90}Sr/^{90}Y$, ^{99}Tc. The color bar units are in counts/pixel.*

3.5. *Count-rate Capability*

The count-rate capability was investigated for the large-area iQID to determine its baseline performance for safeguards applications. The range of activities found on ESS can range between 0.001 Bq – 10^7 Bq, from very weakly radioactive samples to hot cell samples [59]. The probability density distribution and spatial pileup data were calculated based on prior work at the University of Arizona [14] [60], for the large-area iQID, and compared with a smaller-area iQID configuration.

3.5.1 Methods

This experiment analytically compared two different iQID systems (with and without a fiber-optic taper). The purpose of this study is to investigate the count-rate capability for the large-area iQID and the taper's effect. Currently, the CMOS sensor of the large-area iQID operates at a frame rate of 20 frames per second (fps) and a shutter speed of 13.2 ms. One must investigate any performance limitations before imaging at faster rates (75 fps). A previous study derived an analytical solution (**Eq. 11** of Ref. [14]) of the probability density for which two events occur within the detector at a specific distance D apart [14]. The large-area iQID evaluated this analytical solution and compared the iQID system with a smaller area (no taper). These results assumed a uniformly illuminated irradiance and a circular detector area; no error was associated or reported for these calculations (**Equation 18 and 19**).

$$pr(\hat{R}) = pr\left(\frac{R}{L}\right) = 2\frac{\hat{R}}{l}\left[1 - \frac{\hat{R}\sqrt{4-\hat{R}^2}}{2\pi} - \frac{2\arcsin\frac{\hat{R}}{2}}{\pi}\right] \qquad \textit{Equation 18}$$

Equation 18 **above** contains the analytical solution for the probability density function of two-photon event interactions occurring on the detector separated by distance R in pixel units.

Solved with normalized equation ($\hat{\hat{\mathrm{R}}} = \mathrm{R}/\mathrm{L}$) (**Eq. 2.6** of Ref. [60]), this solution demonstrates a dimensionless variable to map probability density into units of detector side length. L is the circular detector radius in detector pixel units. For both systems, the event cluster's size has an estimated radius of 10 pixels. Hence, the main difference between both methods is the increased detector area due to the fiber-optic taper.

3.5.2 Results

As shown in **Figure 22** below, from Equation 18 above, the probability that two photons interact in a certain distance (R) decreases with the fiber-optic taper's addition. The probability density function of two-photon interaction distances has a broader distribution with the fiber-optic taper. **Figure 23** below plots the number of photons with overlapping spatial positions (overlapping clusters) versus the number of photons (clusters) per frame. **Figure 23** shows the small-area iQID system with only an image intensifier (ø25 mm) has approximately 17 overlapped events at 100 events per frame [60]. The LAiQID has six overlapping events at 100 events per frame, hence a lower spatial pileup. **Figure 23** compares the spatial pileup results for both systems using Equation 19 below**.** Equation 19 below represents the spatial pileup expectation value N_{PU} of the number of photons (pileup events) affected by overlapping spatial event clusters (spatial pileup) during an integration period for N number of events (0-1000) in an image frame (**Eq. 13** in Ref. [14]). D_{PU} is the separated distance of events with overlapping events of less than 10 pixels. In other words, for both iQID imagers' configuration, events occurring less than ten pixels apart would be considered spatial overlapping event clusters.

$$\langle N_{PU} \rangle = N[1 - (1 - P(|\Delta \boldsymbol{r}| \leq D_{PU}))^{N-1}] \qquad \textit{Equation 19}$$

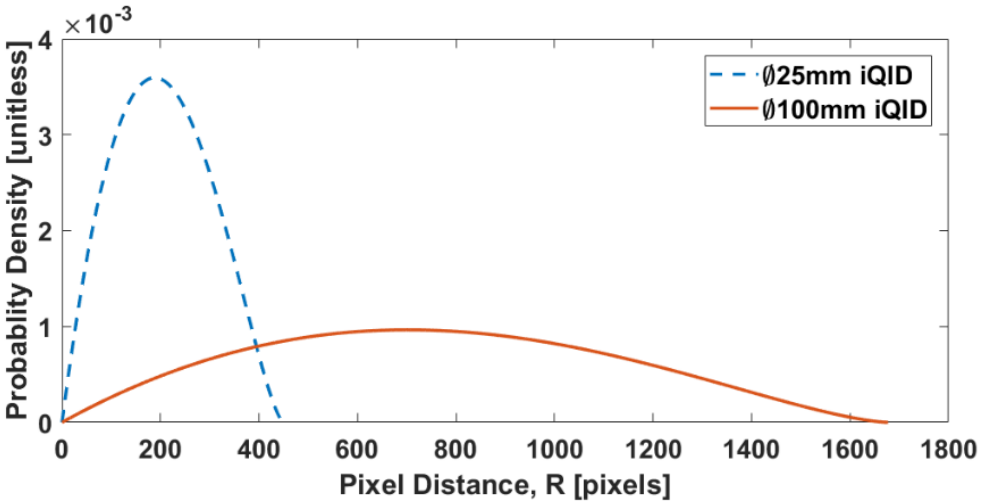

***Figure 22**: Image compares the calculated probability density distribution. Two configurations for iQID imagers are 25mm iQID (only an image intensifier) [6] and 100mm large-area iQID imager that contains a fiber-optic taper and image intensifier.*

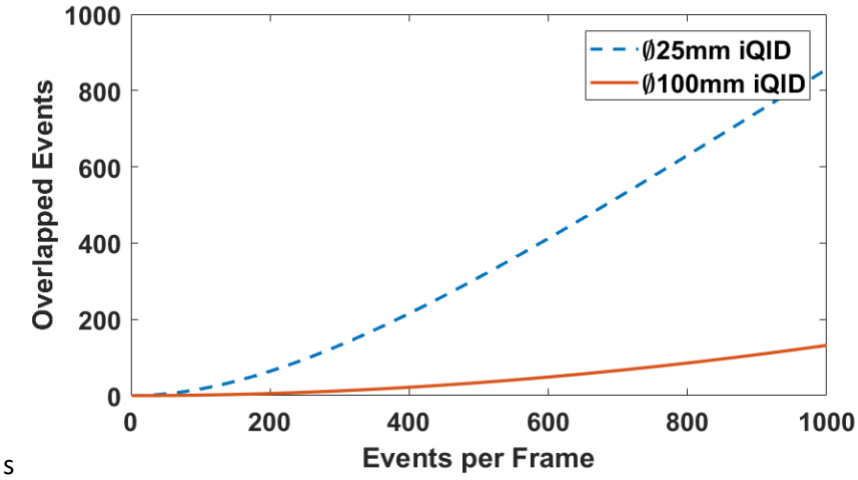

s

***Figure 23**: Spatial Pileup comparison between two iQID systems. iQID configurations either has an image intensifier [6] or a large-area iQID imager with a fiber-optic taper and image intensifier.*

3.5.3 Discussion

At 1,000 events per frame, the large-area iQID would have 132 overlapped events, whereas the smaller iQID 856 overlapped events. If 132 overlapped events were an acceptable fraction (~13%) of total events per frame, at 20 fps this translates to 20 kcps. The frame rate for the current CMOS camera can be increased to 75 fps, implying a count-rate capability up to 75 kcps, assuming no other timing bottlenecks in the system, such as the image intensifier. The upper activity sample ranges for the large-area iQID can be quantitatively imaged using experimental data with an analytical algorithm. With the current setup, we have made quantitative measurements on sources emitting up to several thousand particles/s-cm^2 (~4,000 Bq alpha source).

3.6. Dead Time

Dead time is the minimum amount of time required to separate two events as two separate events. These events represent the random nature of radiative decay. If events occur quicker than the imaging device can quantitively collect, then these actual events are lost, hence called dead time losses. There are two dead time models, paralyzable and non-paralyzable, implemented to describe the timing behavior of the large-area iQID. Detector behavior of counting systems depends on the detector's physical processes or delays in post-processing and reading electronics. There are two time periods in a detector: when events are detected and counted, called the “live” period and when events are not collected, called the “dead” period τ. In the paralyzable model, actual events occurring within the “live” period have a fixed dead time τ. Events happening in the “dead” periods do not have a fixed length of time. However, actual events occurring in the “dead” period extend the dead time by another τ period following the subsequent actual event.

If the dead time is extended for another τ period, then detection efficiency could be improved. For a paralyzable model, the rate of occurrences of time intervals between actual events that exceed τ, m, is represented in Equation 20 **below** where n is the real event rate and τ represents a fixed time interval assumed to follow each actual event that occurs during the "live" period.

$$m = ne^{[-n\tau]} \qquad \textit{Equation 20}$$

In a non-paralyzable model, lost events occur within the "dead" period and do not affect the detector's behavior. Due to the fixed dead periods, the fraction of time the imager is "dead" is represented by $m\tau$ and the rate for actual lost events denotes as $nm\tau$. The non-paralyzable model is further demonstrated mathematically in Equation 21 **below**.

$$n = \frac{m}{1-m\tau} \qquad \textit{Equation 21}$$

In other words, only "dead" events detected in a paralyzable system can delay the detector's timing behavior and decreases dead time losses. The same first-order losses take place in both models but have different actions at high actual event rates. **Figure 24** below represents both models.

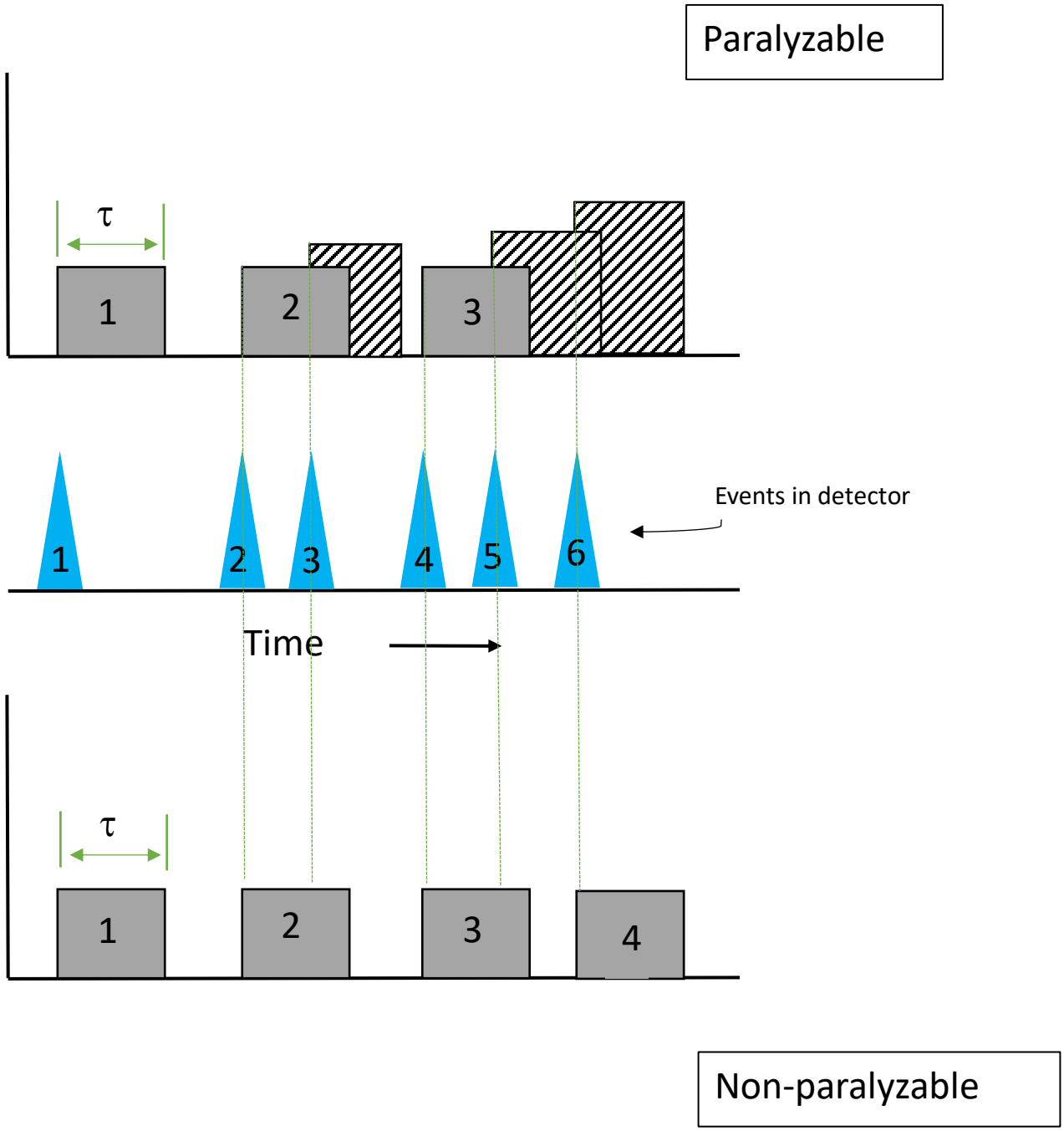

***Figure 24**: Schematic of paralyzable and non-paralyzable models of dead time.*

Figure 24 above shows the different timing behavior for each dead time model and the number of detected separate events inside a detector. In this example, six total events occurred within an imager, but only 3 and 4 events were recorded in the paralyzable and non-paralyzable model, respectively. In the paralyzable model, second and third events (same as the fourth and fifth event) coincide, extending the dead time by another τ. Simultaneous events cause the detector to record these events as one, therefore losing three actual events (event 3, event 5, and event 6). In the non-paralyzable model, there are only two real lost events (event three and event 5) with a fixed timing behavior.

3.6.1 Methods

Computing corrected live times using knowledge of the system's dead time can improve the quantitative accuracy of a detector's performance. Calculated decay corrected live times achieved using knowledge of a limiting property of the system, such as a fixed resolving time of an electronic circuit. For the case of the large-area iQID, the image intensifier would be a limiting electronic property of the detector. The current limiting time factor is the image intensifier's phosphor screen with a decay time of 1 ms. This study investigated the dead time of the large-area iQID. **Table 5** below demonstrates the typical operating settings. Other parameters such as CCD frame rate and gain, shutter, cluster size, and threshold will be changed to determine its role in dead time and count-rate capability of LA-iQID. Chapter 4 **below** presents these results.

***Table 5**: Current Operating Settings of the large-area iQID*

DAQ Parameter	Value
CCD Frame rate (fps)*	20
Shutter (ms)*	49.7497
CCD gain (dB)*	47.9943
Cluster size*	21 × 21
Filter type	Median 3 × 3
CCD pixels	2448 × 2048
Threshold*	55 to 85

*Represents the main imaging parameters

The large-area iQID dead time was measured using the two-source method [16]. Two beta sources previously characterized by the large-area iQID, ^{99}Tc and ^{90}Sr/^{90}Y, were used to determine the dead time of large-area iQID. The scintillator used was TranScreen LE. The measurement process for the two-source method occurs into five parts consists of 1) place source 1, ^{99}Tc, onto the scintillator and measure the observed rate denoted as m_1, 2) place source 2, ^{90}Sr/^{90}Y nearby ^{99}Tc, and measure the observed count rate represented as m_2, 3) measure combined observed rates indicated as m_{12}, 4) remove ^{99}Tc without moving the location of ^{90}Sr/^{90}Y and 5) measure the observed rate of ^{90}Sr/^{90}Y only denoted as m_2. There is a possibility of scattered radiation when the first source is not present. The system dead time is evaluated using background and source observed event rates from the two-source and dead-time model types. Equation 22 **below** expresses the solution for a non-paralyzable dead time model where m_b is the measured background rates without both sources [16].

$$\frac{m_{12}}{1-m_{12}\tau}+\frac{m_b}{1-m_b\tau}=\frac{m_1}{1-m_1\tau}+\frac{m_2}{1-m_2\tau} \qquad \textit{Equation 22}$$

Simplifying Equation 22 **above** into variables X, Y, and Z can represent the system's dead time, as shown in Equation 23 **below** which calculates the dead time of a detector.

$$\tau = \frac{X(1-\sqrt{1-Z})}{Y}$$

where *Equation 23*

$$X = m_1 m_2 - m_b m_{12}$$

$$Y = m_1 m_2 (m_{12} + m_b) - m_b m_{12}(m_1 + m_2)$$

$$Z = \frac{Y(m_1 + m_2 - m_{12} - m_b)}{X^2}$$

3.6.2 Results

The actual event counting rates for background and individual combined source rates were determined using the observed rates in **Table 6** and substituted into Equation 23 above. These results provided insight into the characterized timing behavior (i.e., dead time model) of the large-area iQID. **Figure 25** demonstrates the results of the two-source dead time measurement for the large-area iQID. One significant development is the large-area iQID detector's timing behavior follows a non-paralyzable system (**Figure 26**). The dead time for the large-area iQID imager is 2.3 ms. **Table 6** expresses the associated observed event rates for each step of the two-source dead time measurement.

Table 6: Observed Results from the Two-Source Dead Time Measurement

Source	**Recorded Counts**	**mi, Recorded Rate [CPS]**	**Fraction Time LA-iQID is Dead**	**n_i, True Interaction Rate w/ Losses**
background	18159	60.53	0.1370	70.13718649
Sr-90 (2)	67460	224.87	0.5089	457.8507133
Tc-99 + Sr-90 (12)	108436	361.45	0.8180	1985.517008
Tc-99 (1)	114440	381.47	0.8632	2789.405637

X	Y	Z	Dead Time, Tau [secs/count]
-63900.368	-22931538.785	1.035	0.0023

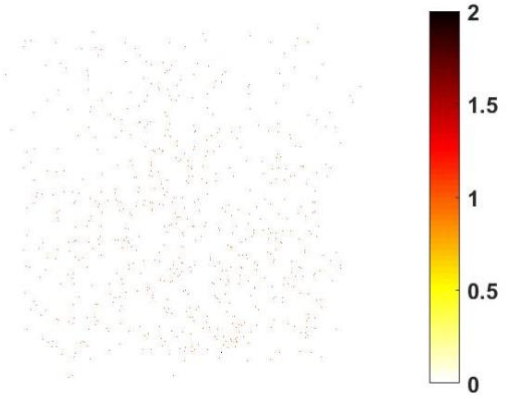

Figure (A): Background

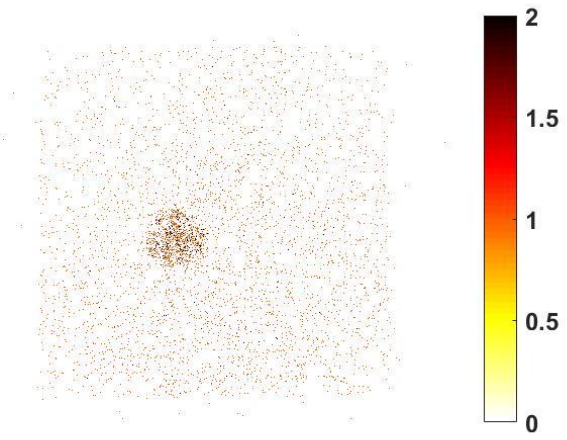

Figure (B): ^{99}Tc only

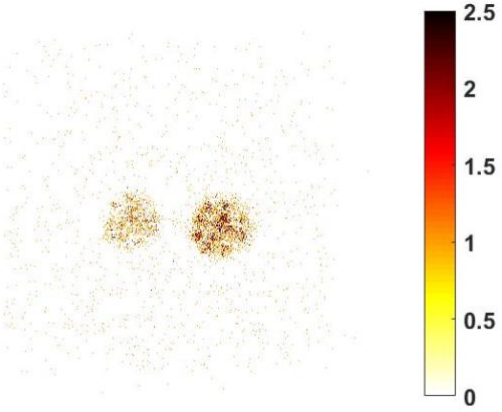

Figure (C): Sources measured ^{99}Tc (left) and ^{90}Sr/^{90}Y (right)

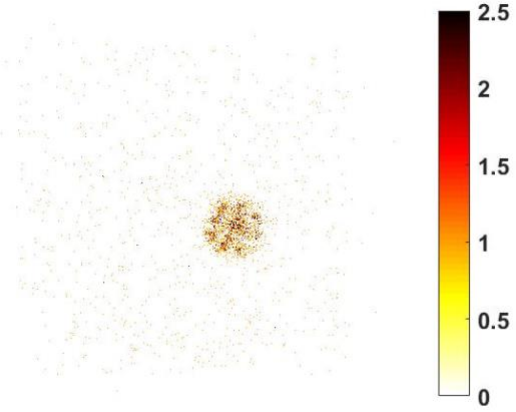

Figure (D): ^{90}Sr/^{90}Y source measured

Figure 25*: Images of the two-source measurement results. Data includes beta/gamma background, ^{99}Tc as source 1, and ^{90}Sr/^{90}Y as source 2, with both measured at 5 minutes with TranScreen LE phosphor screen.*

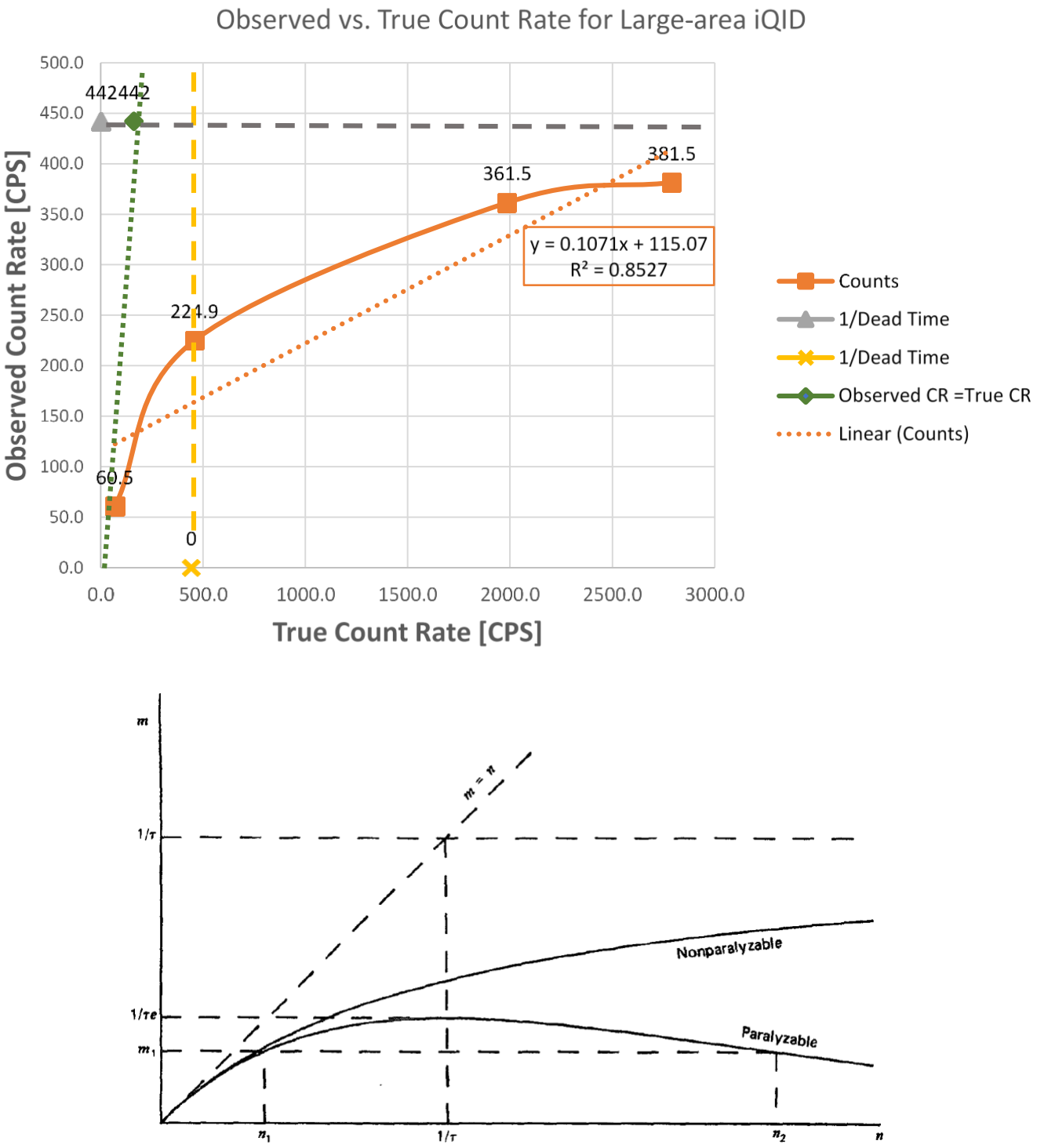

***Figure 26**: (Top) Non-paralyzable Dead Time Measurement of large-area iQID (Bottom) Graphical representation of the two types of detector dead time models [16].*

3.7. Chapter Conclusions

Characterized metrics for large-area iQID are spatial resolution, energy response for alpha and betas/gammas, detector uniformity, MDA, count-rate capability, and dead time. The system's intrinsic alpha and beta spatial resolution is between 100-200 μm depending on the phosphor screen and particle type. In Chapter 5, I explore how energy response data may help discriminate beta and gamma interactions via post-processing data cuts in future efforts. Non-uniformity from the large-area iQID detector's fiber-optic taper dropped the light collection efficiency by a factor of 2. The dropped light integration occurs across the scintillator from the center to the edge. The absolute efficiency didn't follow the same trend because the intensity scintillation flashes were larger than the lower detection threshold (i.e. number of pixels above 60 pixel threshold).

The large-area iQID is sensitive to a range of particles and energies, from >50 keV electrons and gammas to 6 MeV alpha particles. The MDAs range from 0.01-0.1 Bq/cm^2 for β emitters and 4 mBq/cm^2 for α-emitters and the intrinsic efficiency for alphas and high-energy betas is nearly 100%. Lastly, the large-area iQID has a broader count-rate capability (lower spatial pileup) than a previous small-area iQID system without a fiber-optic taper. Next, an evaluation of whether the large-area iQID can detect an extensive range of ESS activities (up to 10^7 Bq) and associated hardware performance limitations. Experimental source count-rate data from the large-area iQID assisted in this evaluation while investigating the imager's hardware components' performance limitations.

Chapter 4

Quantitative Imaging and Pileup Analysis Study at Faster Count-rates

This chapter investigates whether count-rate bottlenecks are present in two configurations of the large-area iQID imagers. The baseline iQID imager containing a fiber-optic taper and a non-gated image intensifier is the first configuration. Possessing a fiber-optic taper also, the iQID imager of the second configuration has a gated image intensifier. This chapter will assess performance limitations for the count-rate of both imagers. First, the derived analytical solution of the spatial pileup of the large-area iQID (Section 3.5.2 **above**) helped to develop a MATLAB Monte Carlo simulation algorithm (MC algorithm). Upon completion, a validated Monte Carlo algorithm is the outcome. A detector with higher count-rate capability, HEXITEC, helps create and benchmark this MC algorithm for further use. Next, this algorithm will stimulate the spatial pileup of large-area iQID and compare its result against HEXITEC. Detector area and cost are the leading performance tradeoff disadvantages between HEXITEC and the large-area iQID. **Figure 27** represents the HEXITEC (high-energy X-ray imaging technology) is a 1 mm thick Cadmium Telluride (CdTe) semiconductor detector. We chose HEXITEC due to its smaller event cluster size (1 vs. 10) and higher count-rate capability than the large-area iQID. Stimulating an event cluster size of 1 (for HEXITEC) vs. 10 (for large-area iQID) was significantly easier to benchmark for the MC algorithm. This algorithm was later adapted for the large-area iQID and compared to the spatial pileup analytical solution in **Figure 23**. As a result, the MC algorithm and analytical results compared favorably with the measured spatial pileup levels.

This MC algorithm was implemented to determine the average number of events with spatial - pileup for LAiQID when measured with 505 μC ^{241}Am source.

Two imaging parameters were adjusted to investigate the imaging limitations for the large-area iQID: the CMOS shutter (aperture) time and the CMOS frame-rate. CMOS shutter time and frame-rate were modified to determine how these parameter changes affect the large-area iQID imager's detection performance. Modifications made to imaging parameters are mostly independently based on particle types and interactions. These imaging studies use low to medium-energy beta interactions from ^{99}Tc and low-energy gammas ^{41}Am. Imaging settings for baseline large-area iQID imager occur only at 20 frames per second (fps) and 49ms CMOS shutter.

Observed count-rates, detected activity, absolute efficiency, and average events per frame were the evaluation metrics for both large-area iQID imager experiments. These experiments aimed to determine the feasibility of quantitative imaging with different radiation interactions and different imaging settings. A spatial pileup analysis assisted in these quantitative imaging experiments to demonstrate the effects of varying imaging settings. Different imaging settings tested are as follows:

a. Fixed CMOS frame-rate at 20 fps and CMOS aperture time ranging from 2.8ms to 49ms,
b. High CMOS frame-rate up to 75fps at reduced CMOS aperture time from 49ms to 2.8ms,
c. CMOS imaging at 75 fps with a short aperture time of 2.8 ms,
d. Gated image intensifier with a controllable pulse width

***Figure 27**: Example pictures of a CdTe HEXITEC semiconductor detector [61]*

4.1. Spatial Pileup Analysis

A spatial pileup analysis was conducted for the large-area iQID and HEXITEC to investigate count-rate capability further. Both detectors have different detector properties expressed in **Table 7** below.

Table 7. Comparison of the large-area iQID imager and HEXITEC in terms of the essential detector properties

System	Large-area iQID	HEXITEC
Sensor Material/Readout	Phosphor Screen/ CMOS USB 3.0 Camera	1mm thick CdTe/ HEXITEC ASIC
Number of Pixels	2448 x 2048	80 x 80
Frame Rate (FPS)	20-75 FPS	100 - 9,000 FPS
Active Area (cm^2)	100 cm^2; fiber-optic taper	4 cm^2
Particle Types	α, β, γ, n, and fission fragments	γ
Spatial Resolution (μm)	α: 20-60 μm* α: 94 μm β: 142 μm	γ: ~250 μm
Energy Resolution (FWHM)/Threshold	~5 keV min threshold	0.8 keV @ 60 keV
Pixel Size (μm)	60 μm (effective)	250 μm
Data Processing	Frame parsing algorithms enhanced with GPU	Large file sizes with no "on-the-fly" frame parsing algorithm
Cost ($/$cm^2$)	~400	~8500
Portability	Portable, runs on a laptop	Portable, runs on a laptop
Typical Cluster Size (pixels)	10	1

*Properties of smaller iQID configuration system (4 cm)

It is worth mentioning that both imagers have comparable advantageous properties such as sizeable active imaging and easy transport. When directly compared to HEXITEC, data processing, spatial resolution, and cost are critically valuable properties of the large-area iQID. This analysis chose HEXITEC as a comparable detector based on better energy resolution, smaller cluster size, faster readout device, and higher count-rate capability. The research aims to benchmark the derived analytical MATLAB Monte Carlo algorithm for analyzing the spatial pileup of HEXITEC.

As a result, the analytical algorithm for spatial pileup calculates the average number of events per frame detected on the CMOS sensor. This chapter provides insight into the quantitative imaging ability for how other radiation interactions respond within the large-area iQID imager.

4.1.1 Imaging with HEXITEC and large-area iQID

4.1.1.A Methods

A MATLAB analytical and Monte Carlo simulation algorithm for HEXITEC and the large-area iQID was derived. The MC algorithm calculated spatial pileup based on its detector structure and readout device. Dr. Lars Furenlid et al. 's peer-reviewed journal article for "Spatial Pileup for pixelated gamma-ray detectors" developed a spatial analysis framework [14]. HEXITEC has a circular detector diameter of 80 pixels and an event cluster separating distance of 1.4 pixels. On the other hand, the large-area iQID has a detector diameter of 1677 pixels but a complex detector structure. This complexity in the imaging structure of the large-area iQID is due to the different geometries of the fiber-optic input window/ taper and image intensifier and CMOS sensor (square vs. circular). The basic framework of the MATLAB Monte Carlo simulation is circular. Section 3.5.1 **above** expresses the equations for the analytical solution.

Next, a MATLAB Monte Carlo simulation algorithm for HEXITEC was developed and compared against the analytical solution to validate its successful performance. Once validated, the MC algorithm used characterized ^{241}Am count-rate data to calculate spatial pileup for the large-area iQID. The process steps of the MC algorithm operated as follows:

1. A random number of trials were selected to determine how many times the readout device should detect simulated events. The algorithm for HEXITEC selected 100 trials.

2. Create a mask for the active imaging area of the detector of choice. 80 x 80 pixels for HEXITEC, and the large-area iQID is 2448 x 2048 pixels.
3. A connected component algorithm in MATLAB calculated the allotted number of events per frame. This algorithm sets the number of connected events.
4. For HEXTIEC, any two event clusters less than 1.4 pixels apart were considered overlapped and counted as spatial pileups. Whereas 14.14 pixels apart was the minimum distance for the large-area iQID.
5. The MATLAB analytical and Monte Carlo algorithm plotted the number of spatial pileup events clusters versus the average number of events clusters per frame for both detectors.

4.1.1.B Results

The MC algorithm calculated the spatial pileup for HEXITEC (**Figure 28**) and the large-area iQID (**Figure 29**). This algorithm plotted the number of overlapped events clusters or spatial pileup vs. the average number of events per frame. **Figure 28** shows the analytical solution of spatial pileup per the average number of events for HEXITEC is closely aligned with MC algorithm for HEXITEC. Note the analytical solution for spatial accumulation previously calculated and demonstrated in **Figure 23**. This result validates the functionality of the MATLAB simulation algorithm and applicable to the large-area iQID. The imaging area is adjusted to resemble the CMOS readout sensor by increasing the minimal distance for spatial pileup to 14.1 pixels. In contrast, the imaging area for HEXITEC is 1.4 pixels.

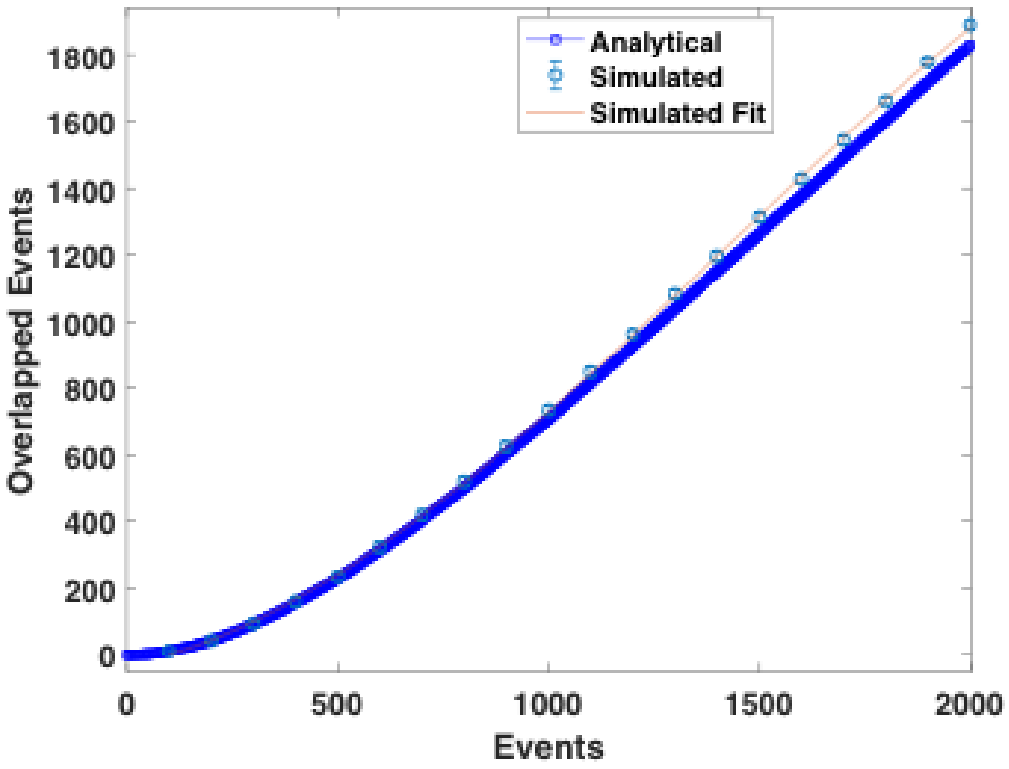

***Figure 28**: Image shows the spatial pileup per average number of events per frame results for HEXITEC CdTe semiconductor detector. Represented data for the derived analytical solution and Monte Carlo simulated algorithm.*

As expected, **Figure 29** shows a close agreement between the derived analytical solution and MC algorithm of the spatial pileup for the LAiQID. This demonstrates that the MC algorithm can characterizes the spatial pileup of the large-area iQID. Assuming a circular detector diameter instead of the square detector geometry could attribute to the slight deviation between both curves (**Figure 29**). In other words, the LAiQID imager can use this MC algorithm further to analyze the imager's spatial pileup using experimental data of a 505 μC ^{241}Am source.

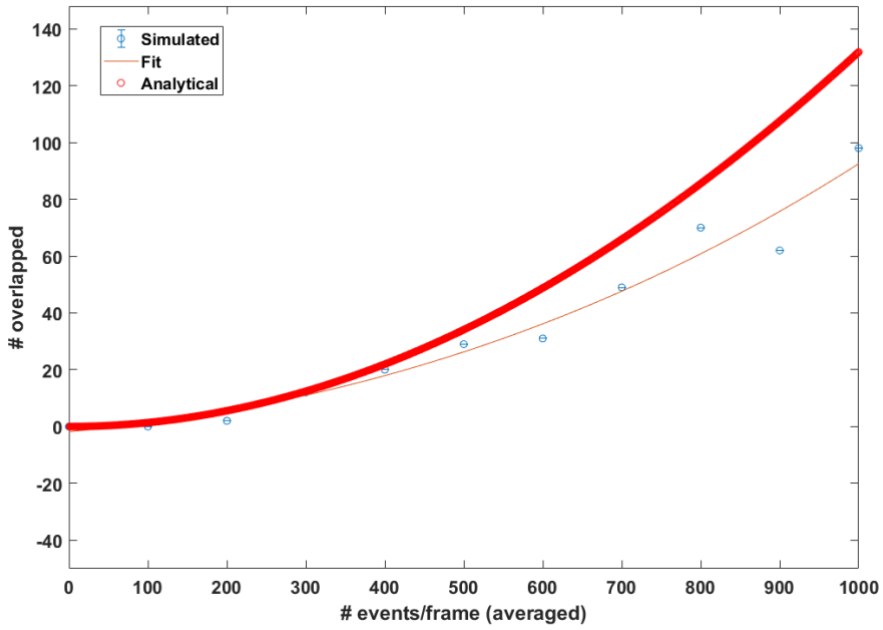

***Figure 29**: Analytical derived and Monte-Carlo simulated data for LA-iQID results of spatial pileup vs. average number of events per frame.*

4.2. Quantitative Imaging at Higher Count-rates

Two different scenarios investigated the quantitative imaging of the large-area iQID. All methods will provide insight into whether the CMOS camera or the image intensifier has the most significant count-rates limitation. The first scenario will observe the relationship between count-rate and image intensifier will be observed by introducing gating at the photocathode of the imager intensifier. Gating allows a snapshot of the flux from the source to be measured, potentially reducing events' spatial pileup. First, new baseline measurements will be conducted for this new gated large-area iQID imager using ^{99}Tc. Measurements will consist of background, count-rates/event-rates, energy response (i.e. cluster intensity), and event cluster dispersion (i.e. cluster area). Likewise, measurements will be conducted with different gating waveform settings (i.e., pulse widths). These measurements will characterize the new gated large-area iQID imager to determine which imaging settings provide the highest count-rates and absolute efficiency and how to set gating parameters for a given source activity properly. The second scenario will investigate the relationship between count-rate and activity from data in the previous method. This will demonstrate whether our detected count-rates are linearly related to the source (surface) emission rate.

4.2.1. Scenario 1: Effect of gating image intensifier on count-rate

The gated image intensifier of the large-area iQID is controlled by four main imaging parameters. These parameters consist of gating frequency, gating amplitude, DC offset, and duty cycle.

According to the vendor, Proxivision, these gating signal parameters are controlled via an external TTL input pulse ("Pulse Follow mode") connected to the photocathode. This was experimentally achieved by using a waveform generator to set the required imaging parameters. The first imaging parameter, gating repetition rate or frequency, should match the CMOS camera's frame-rate speed of the large-area iQID. For these measurements, the gating frequency will be 20 Hz and gating times similar to the scintillator, Transcreen LE, of 1 μs to 1 ms. An example of the recommended TTL input signal/waveform is expressed in **Figure 30**, where gating at the photocathode occurs after the TTL input signal is applied.

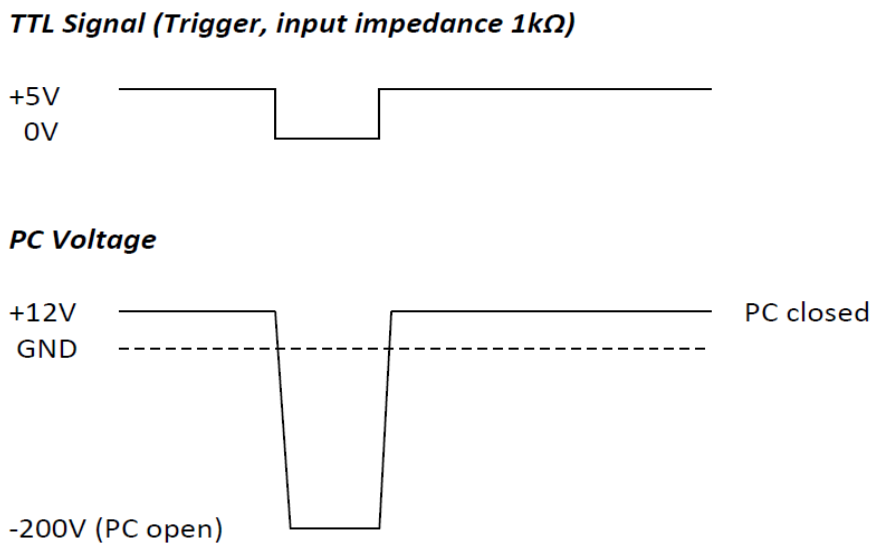

***Figure 30** : (Top) Recommended Vendor Waveform from Proxivision vendor with TTL signal trigger voltages of +5V and 0V. These correspond to photocathode (PC) voltages of +12V and -200V of closed and open, respectively.*

The second gated imaging parameter is amplitude, which is the maximum displacement of a wave measured from its equilibrium position [62]. As shown in **Figure 30**, the gating amplitude is $+5V_{pp}$ (peak-to-peak) and equal to the microchannel plate's control voltage. If the TTL input pulse is +5V, then the gated photocathode (PC) is set to an input voltage of +12V. In other words, the gated photocathode at +12V is not sensitive to light. The gated photocathode is only sensitive to light at -200V after receiving a TTL input pulse of 0V. The third gated imaging parameter, DC offset, is the mean amplitude displacement of a waveform gating signal from zero. For these gated large-area iQID measurements, the DC offset will be constant at +2.5V. The fourth gated imaging parameter, the duty cycle, is the focus of this section. The duty cycle is the percentage of time when the gating signal is "ON" and can be defined by Equation 24 **below**. As shown in Equation 24 **below**, the duty cycle is determined by pulse width and period. Pulse width is the time from a 50% threshold of the pulse's rising edge to a 50% threshold of the next falling edge. The period is the reciprocal of the gating frequency (20Hz), as previously discussed above [63].

$$Duty\ Cycle\ [\%] = \frac{100\ x\ (Pulse\ Width)}{Period} \qquad \textit{Equation 24}$$

In this first scenario, the duty cycle was adjusted according to the CMOS shutter's pulse width of 50 ms. The gating signal was repeated at the same gating frequency (20 Hz) as the CMOS frame-rate (20 FPS). At a 50 ms CMOS shutter, the duty cycle was 100% by using Equation 24 **above**. In other words, the gating frequency of the image intensifier matched the frame-rate of the CMOS sensor. To have the image intensifier "on" for half the CMOS shutter (i.e., 25 ms), the duty cycle would be reduced to 50%. An example image of a square wave at normal polarity and 50% duty cycle is expressed in **Figure 31**.

This idea of lowering the duty cycle of the gated large-area iQID down to 0.01 % was further investigated **below**. This demonstrated the effectiveness of the gated image intensifier on the count-rates of the large-area iQID. Hence, providing insight into the signal generation process of image intensifier and CMOS sensor.

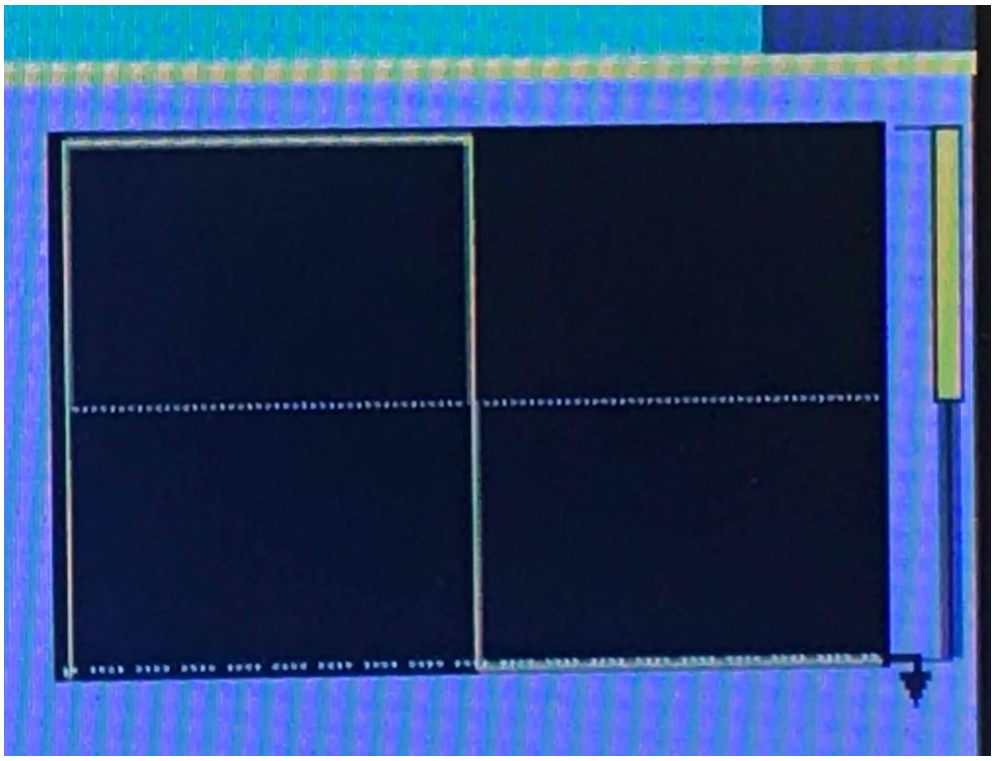

***Figure 31**: Example of a square waveform at normal polarity and 50% duty cycle*

4.2.1.A Methods

In this second scenario, gated measurements were tested with ^{99}Tc at constant frame-rates (20 FPS) and CMOS shutter times (50 ms). First, characterization measurements were conducted in alpha and beta imaging mode. Scintillators used for alpha and beta imaging mode were ZnS:Ag and TranScreen LE scintillator, respectively. The alpha characterization measurements consisted only of background measurements. On the other hand, beta characterization measurements consisted of background and source measurements with ^{99}Tc. This was achieved by calculating three different metrics for the non-gated and gated background and source (^{99}Tc) baseline measurements (beta imaging mode only). Metrics included count-rate, source and non-source ROI analysis, and data cuts using cluster intensity and area. New non-gated large-area iQID baseline background (**Figure 36**) and ^{99}Tc baseline measurements (**Figure 39**) were first conducted. This preliminary step was required because gated background count-rates were currently unknown since this was a new configuration for large-area iQID imager. To match the specifications of the Vendor (Proxivision), characterization of gated ^{99}Tc baseline measurements occurred at an inverted polarity and 99% duty cycle. The remaining gated imaging parameters were fixed at a gating frequency of 20 Hz, TTL gating amplitude of +5Vpp, and a DC offset of +2.5V. Since the waveform generator could introduce normal or inverted wave polarities, both polarities were tested to determine their effect on count-rate. This step was used as an operational validation because it was hypothesized that the inverted polarity would produce the highest count-rates. I hypothesized this because Proxivison vendor stated the recommended TTL signal was inverted polarity (**Figure 30**). Waveforms of the different polarities and duty cycles for the newly source, non-gated, and gated backgrounds were tested.

Figure 32 shows the waveform for the newly non-gated baseline background measurements and **Figure 33** displays the waveform for baseline measurements conducted at an inverted polarity with a 99% duty cycle.

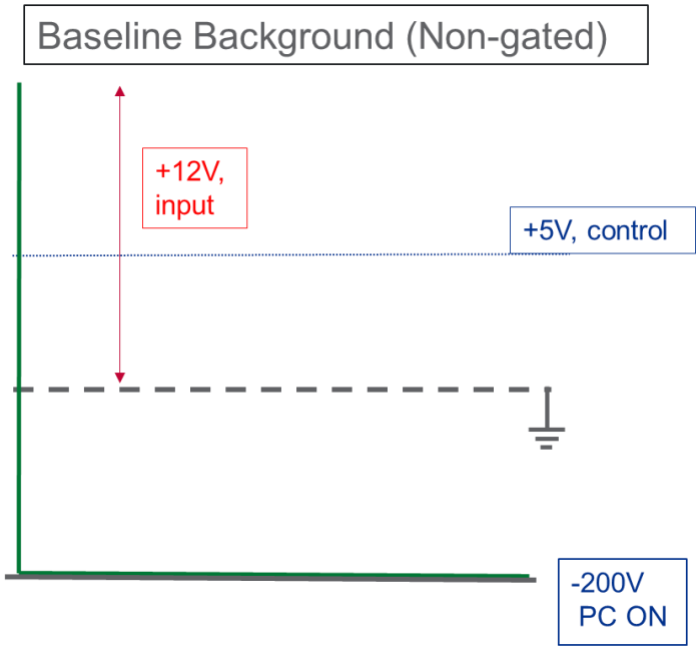

***Figure 32**: Schematic of the new baseline (non-gated) signal within the gated image intensifier's microchannel plate.*

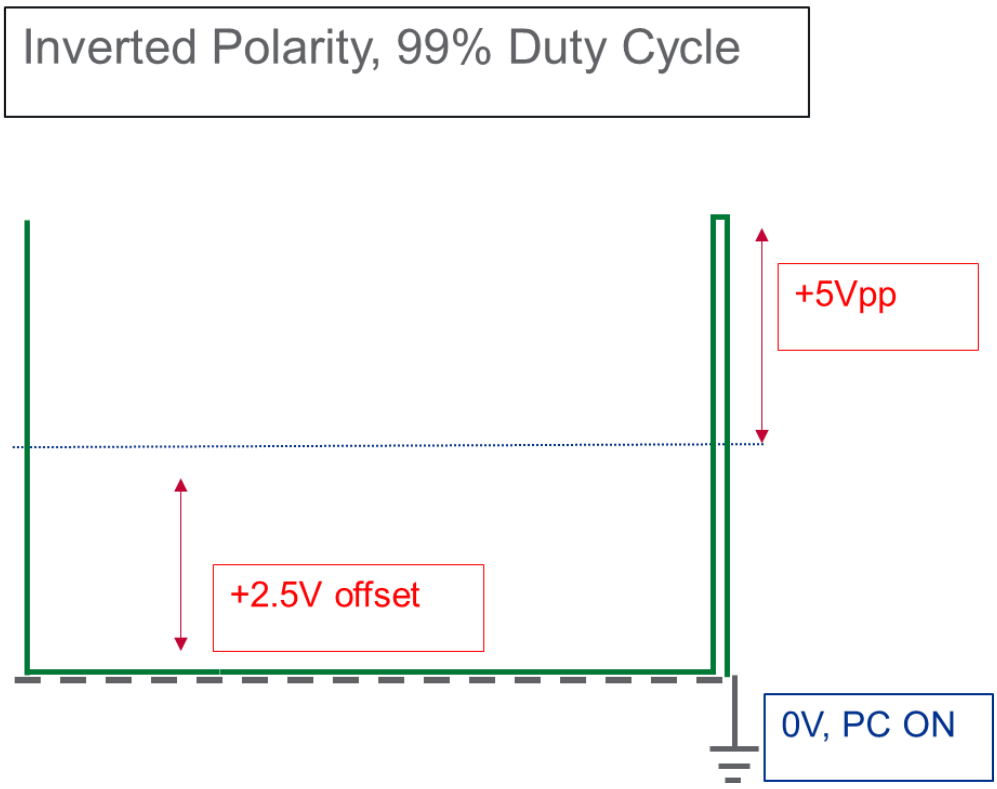

***Figure 33**: Schematic of the new baseline (gated) signal within the microchannel plate of the gated image intensifier at 99% duty cycle and an inverted polarity.*

The gated LAiQID is a new iQID imager configuration so the absolute efficiency of ^{99}Tc must be re-calculated as the new characterized baseline for the gated LAiQID. The purpose of this experiment was to determine the impacts of the gated imaging parameters on count-rate capability. As for the new baseline measurements, examples of the different duty cycles and wave polarities to characterize the gated image intensifier are expressed in **Figure 34** and **Figure 35**.

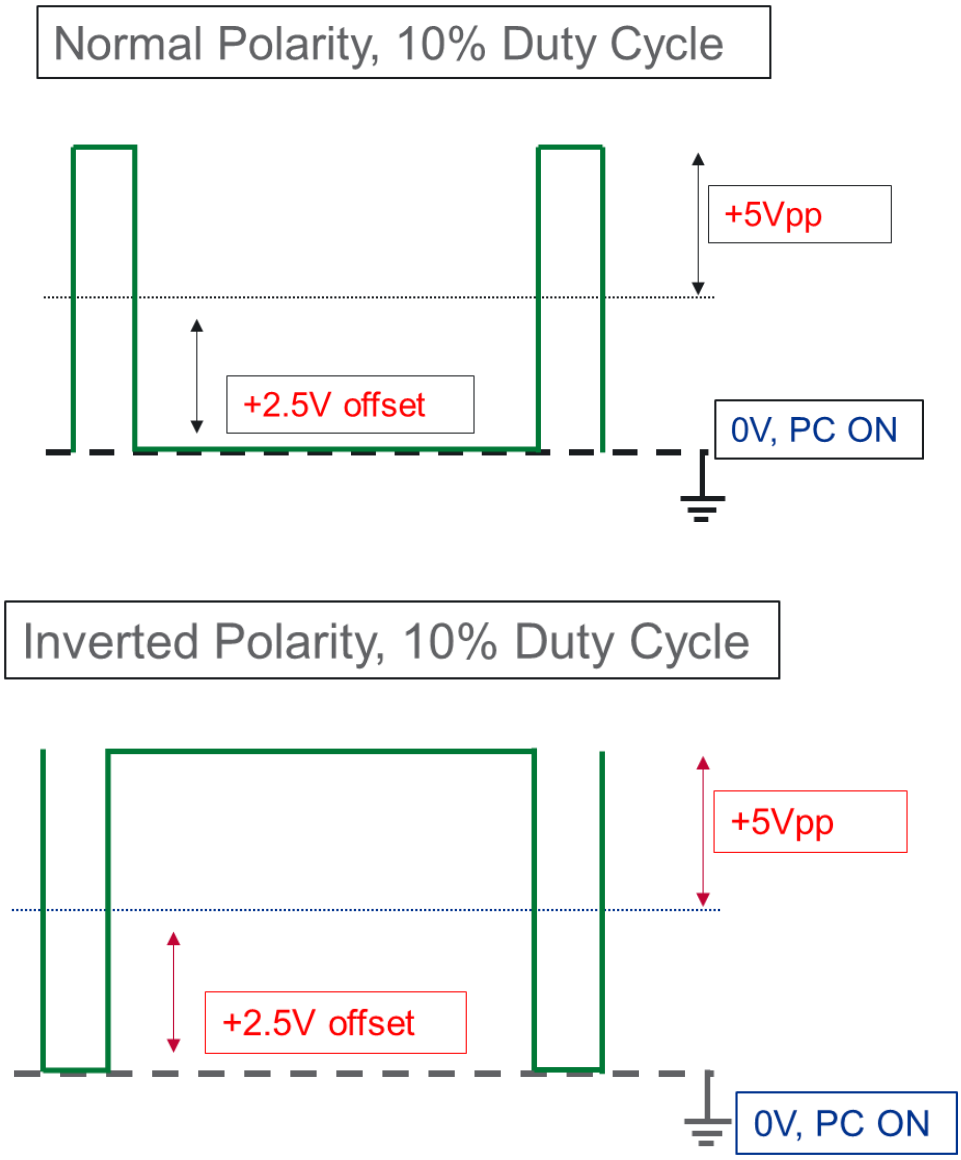

***Figure 34**: Schematic of the gating signal within the microplate at 10 % duty cycle and normal polarity (top) and inverted polarity (bottom).*

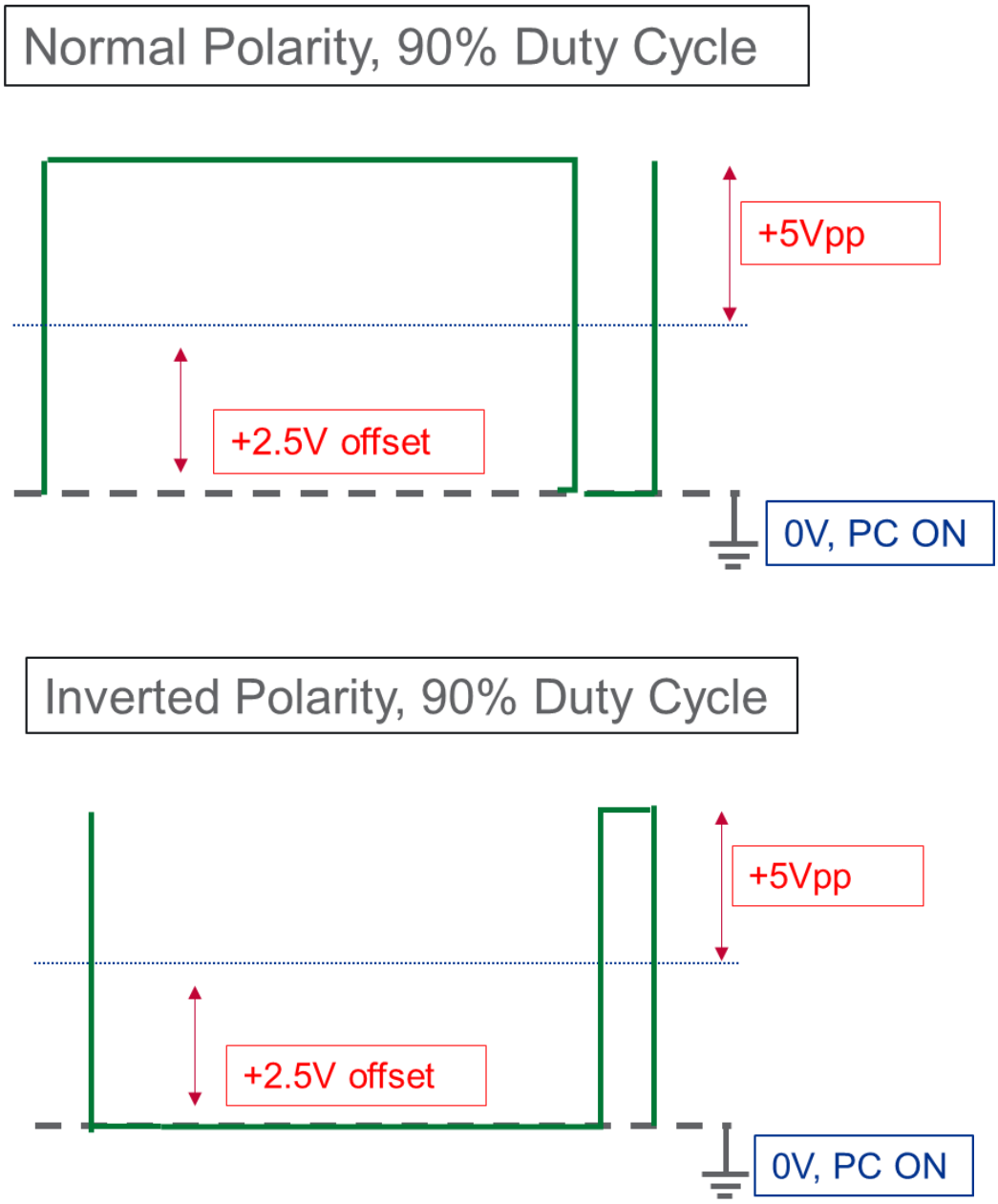

***Figure 35**: Schematic of the gating) the signal within the microchannel plate at 10 % duty cycle and normal polarity (top) and inverted polarity (bottom).*

4.2.1.B Results: Beta Imaging Mode

New baseline background measurements of the gated large-area iQID imager were conducted to characterize the new system. All measurements were made for 5 minutes, and all ROIs consisted of 400 x 400 pixels in the centroid image.

i) Non-gated Background Measurements

The centroid image of the non-gated background is expressed below in **Figure 36**. The total counts detected in this centroid image was 5,461 counts for a total count-rate of 1,092.2 counts per minute (CPM). The average event-rate for this non-gated background measurement was calculated and found to be 0.92 events per frame.

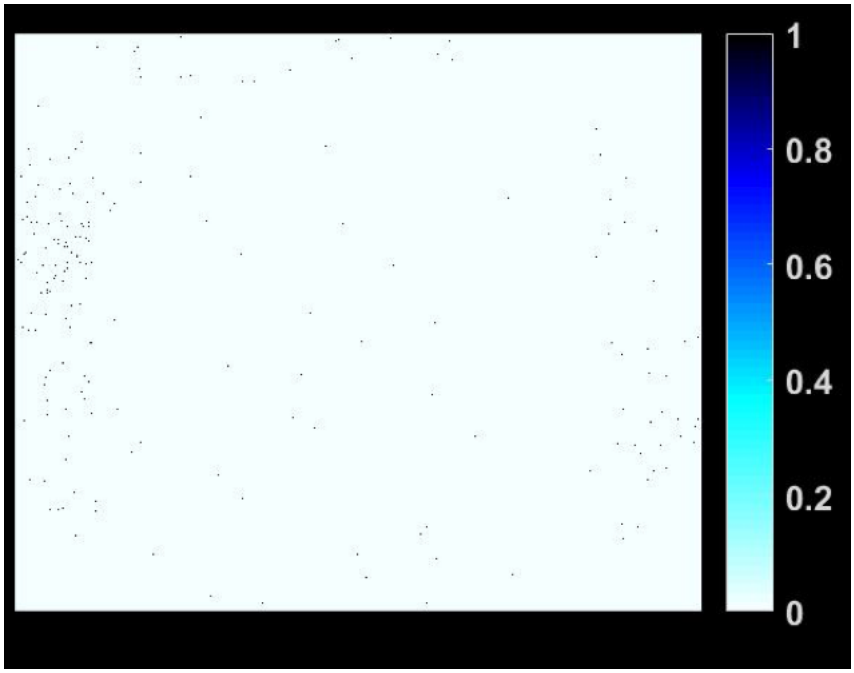

***Figure 36**: Centroid images processed from the large-area iQID imager of the new non-gated background measurement of 1092.2 counts per minute. Images are the same, just in a different colormap for viewing purposes.*

As shown in **Figure 37**, the total event-rate is constant during the full acquisition time. There were a few pikes of high event-rates with an average of 8 events per frame within the first minute of acquisition. As the LABVIEW acquisition continues, the average event-rate is reduced and leveled out at approximately 4 events per frame.

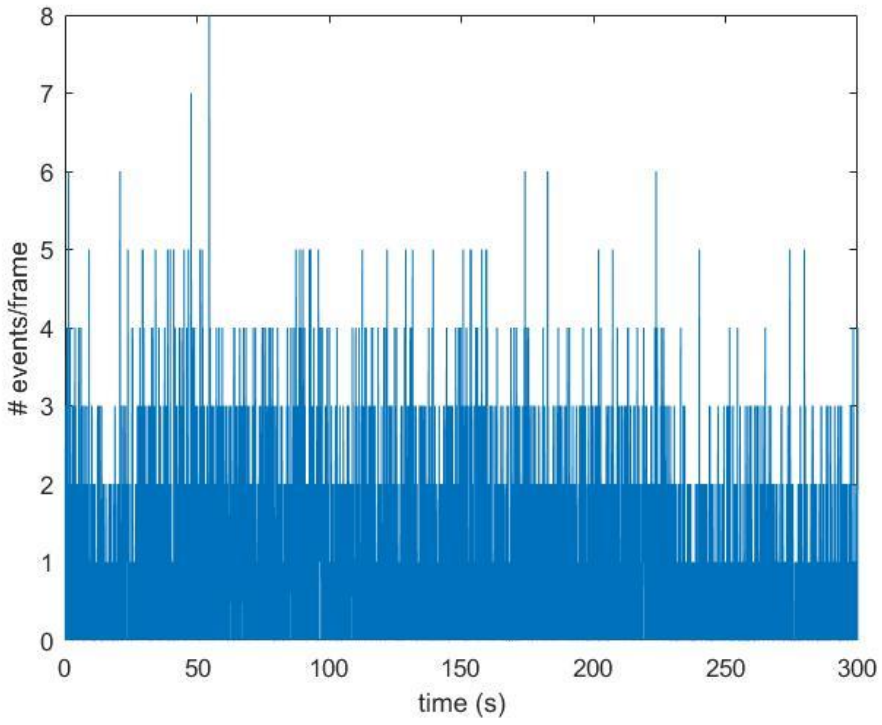

***Figure 37**: Average number of events per frame detected within a 5-minute acquisition for the non-gated background measurement.*

Center and upper left background ROI analysis were conducted and found to have 58 and 53 total counts, respectively. This corresponds to an 11.6 CPM source ROI count-rate and 10.6 CPM non-source ROI count-rate. It should be noted that the counts in source ROI were calculated over the area where the source was located on the scintillator.

The counts in the non-source ROI were calculated over the same area as the source ROI, but in the left-hand corner of the scintillator. Based on the detected counts, histograms for cluster intensity and location (i.e., area) were calculated and shown in **Figure 38**. As cluster intensity and area increased, a sharp exponential-like decrease in counts occurs at cluster intensities between 300-1,500 counts and cluster areas less than 150 pixels. There is a peak in cluster areas located between 0-50 pixels. However, the maximum cluster intensity and area were 46, 966 counts, and 370 pixels. As shown in **Figure 38**, the peak of cluster intensities for non-gated background measurements occurs between 0-0.25 $x10^4$ counts and cluster areas between 10-30 pixels.

ii) Non-gated ^{99}Tc Baseline Measurements

Baseline measurements for ^{99}Tc were conducted for non-gated and gated imaging settings of the large-area iQID imager. First, non-gated imaging of ^{99}Tc was performed and became the baseline for the ^{99}Tc gated measurements. The total detected counts were calculated at 29,479 counts with a total count-rate of 5,895.8 CPM. This is roughly 5x the total count-rate of the non-gated background measurement discussed above. The centroid image for the ^{99}Tc non-gating results is shown in **Figure 39**.

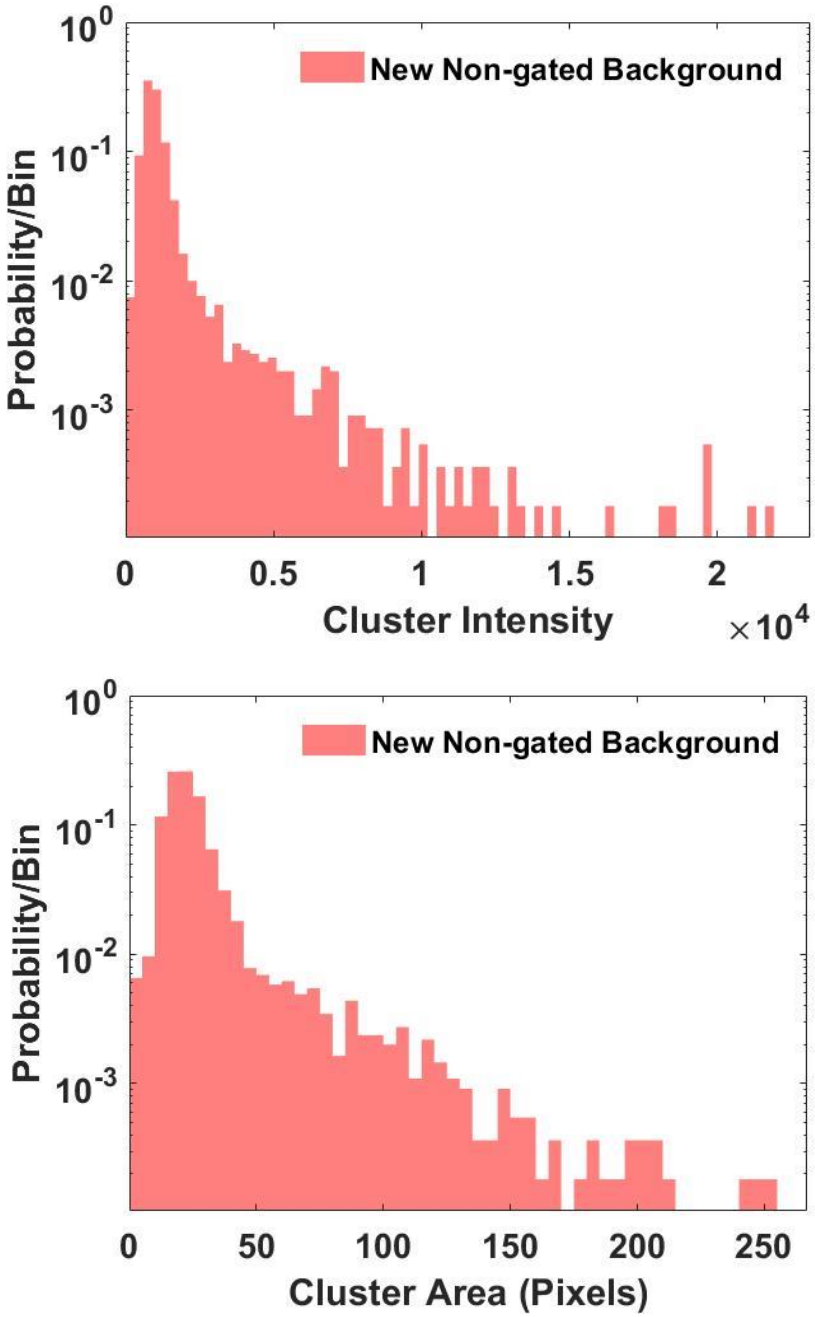

***Figure 38**:Histogram of cluster intensity (top) and cluster area (bottom) for new non-gated background measurement at 99% inverted polarity, 20 Hz, +5Vpp, +2.5V DC offset.*

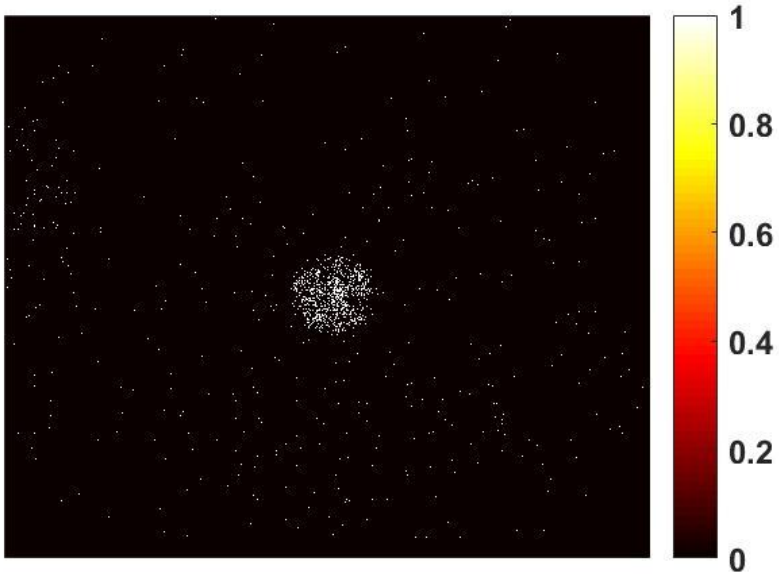

***Figure 39**: ^{99}Tc Centroid Image from non-gated large-area iQID with a total count-rate of 5,895.8 CPM.*

The average event-rate for the non-gated ^{99}Tc baseline was calculated and found to be 4.93 events per frame. As expressed in **Figure 40**, the total event-rate for non-gated ^{99}Tc is less constant than the non-gated background measurement at 0.92 events per frame. This can be observed as events per frame vary between 0-23 events during the full acquisition of 5 minutes. This average event-rate for the non-gated ^{99}Tc baseline can be compared to the 0.92 average event-rate for the non-gated background. In other words, the average event-rate for the ^{99}Tc non-gated baseline is 5x more than the average event-rate of the non-gated background. Next, ROI analysis was conducted to determine the differences between the detected counts and count-rates of source and non-source ROI. The total counts from the ^{99}Tc and non-source ROI were calculated to be 19,197 counts (3,839.4 CPM) and 7,953 (318.12 CPM) counts.

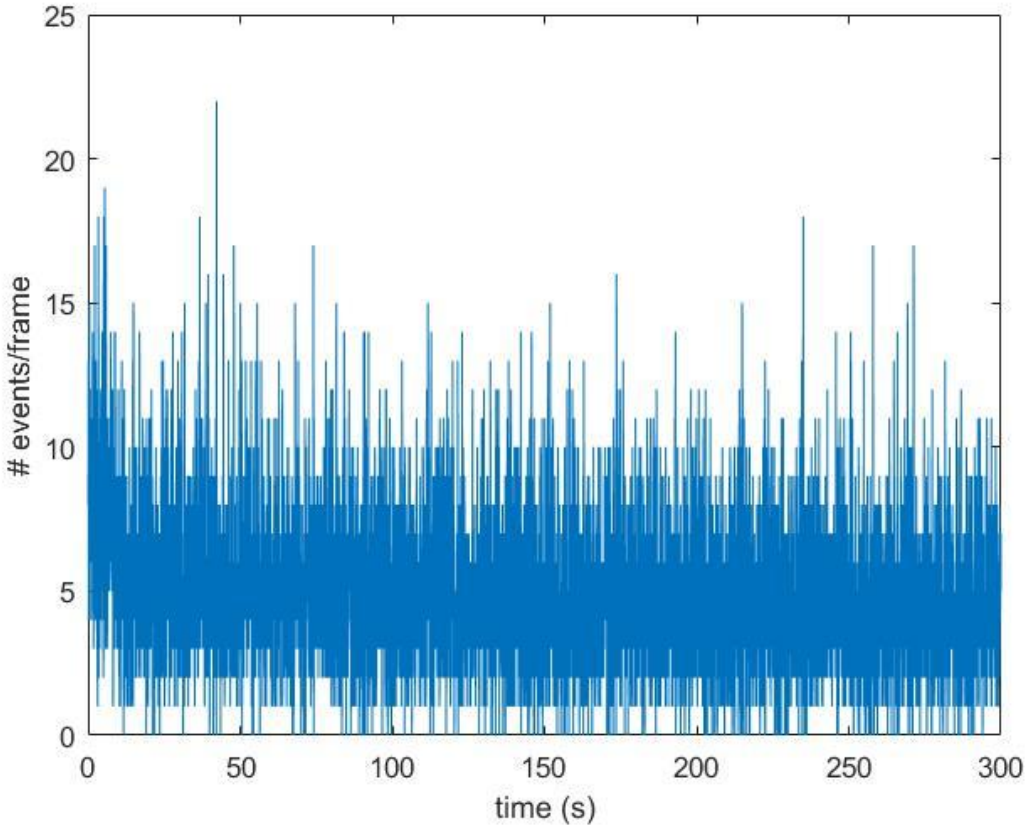

Figure 40: *Average number of events per frame detected within a 5-minute acquisition for the non-gated ^{99}Tc baseline measurement.*

Next, in **Figure 41**, cluster intensity and area histograms were calculated for the non-gated ^{99}Tc. The maximum detected cluster intensity and the cluster area was 34,595 counts and 305 pixels, respectively. However, there seems to be an exponential-like decrease in counts at cluster intensities less than 1.5 x 10^4 counts with a peak between 400-1,400 counts. A similar trend occurs at cluster areas less than 240 pixels with a spike between 10-30 pixels. These limits for cluster intensity and cluster area are identical to histograms reported in the non-gated (**Figure 38**) and gated (**Figure 44**) background measurements.

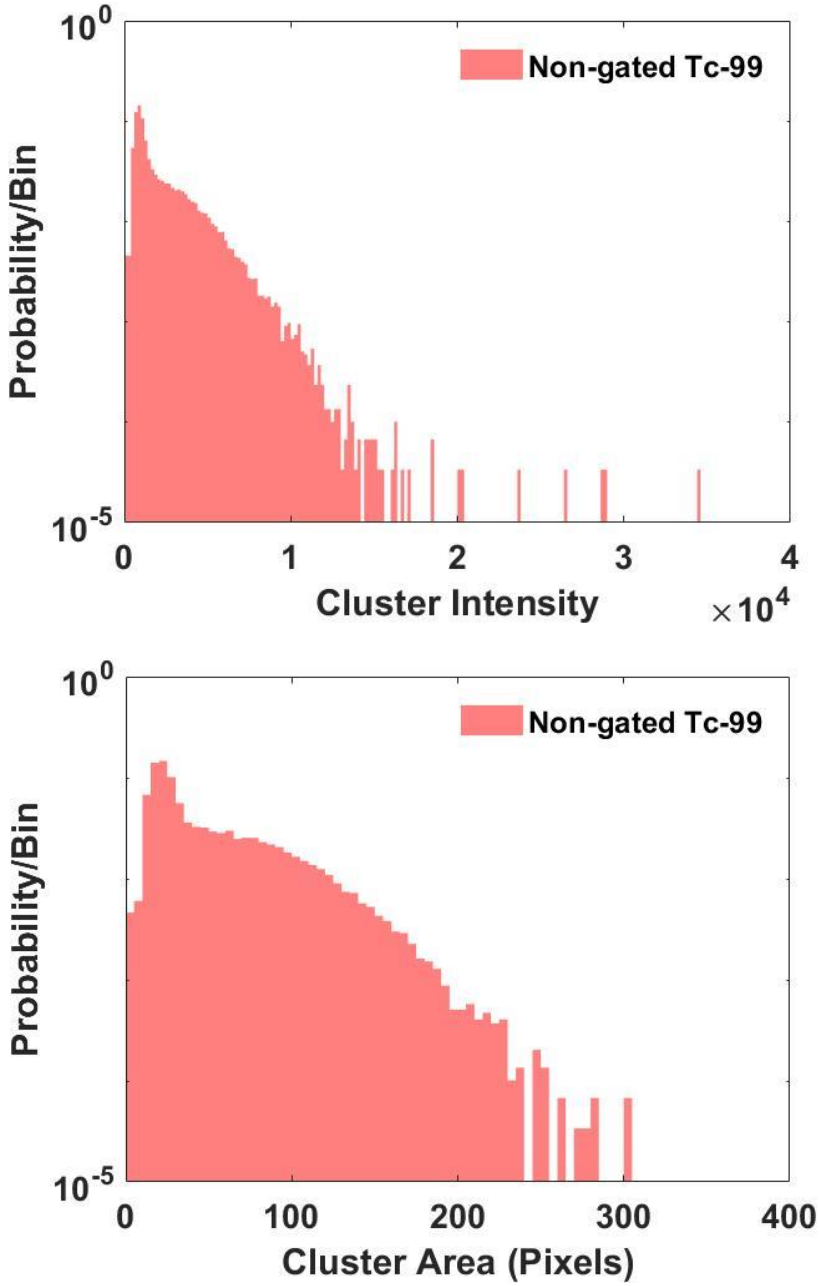

Figure 41: *Histogram of cluster intensity (top) and cluster area (bottom) for new non-gated ^{99}Tc measurement at 99% inverted polarity, 20 Hz, +5Vpp, +2.5V DC offset.*

iii) Gated Background Measurements

This analysis was repeated for the gated background measurements and compared to the non-gated background measurements above. As in **Figure 33**, these gated measurements were imaged at a 99% duty cycle, inverted polarity, 20 Hz gating signal, +5Vpp, and +2.5V DC offset. The centroid image of the new gated background measurements is expressed in **Figure 42** and detected a total of 10,386 counts or a total count-rate of 2,077.2 CPM. The average event-rate for gated background measurement was calculated and found to be 1.74 events per frame.

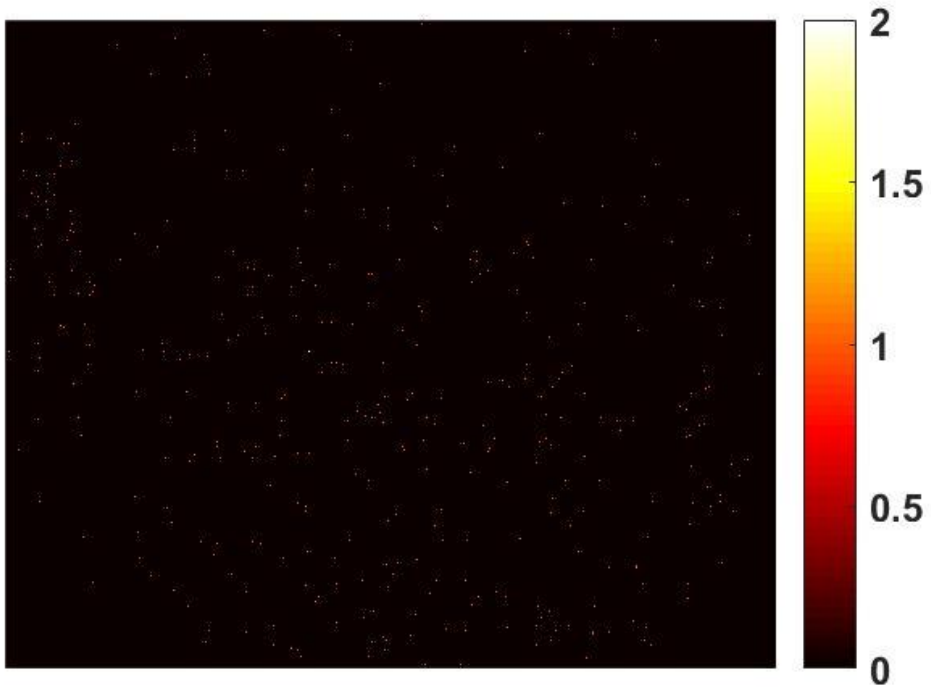

***Figure 42**: Centroid image of the new gated background measurement with total count-rate of 2077.2 CPM.*

This average event-rate is slightly more than the non-gated background measurement at 0.92 events per frame. As shown in ***Figure* 43**, total events per frame during acquisition are less constant than the non-gated background measurement. This can be seen in the several high peaks between 10-13 events per frame within the first 15 seconds of acquisition. These high peaks in event-rates can be due to detector noise upon starting the waveform generator. As the run continues, event-rates decrease and vary between 0-9 events per frame.

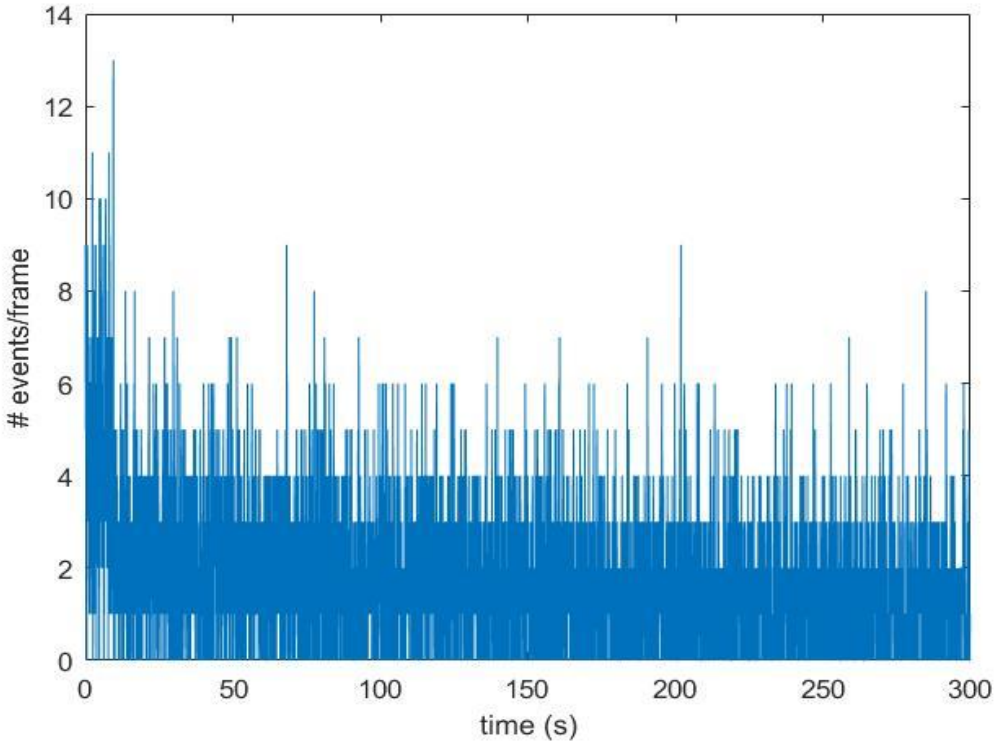

***Figure 43**: Average number of events per frame detected within a 5-minute acquisition for the gated background measurement.*

Using ROI analysis, gated background count-rates were calculated. The center and upper left counts were found to be 578 and 573 counts, respectively. This corresponds to a source count-rate of 115.6 CPM and a non-source count-rate of 114.6 CPM. By comparing this to the non-gated background measurements above, the gated background's total count-rate doubled from 1,092.2 CPM to 2,077.2 CPM. Hence, the gated background center and upper left count-rates were found to be 10x more than the non-gated background count-rates (using the same ROIs). The increase in background rates could be due to the addition of the waveform generator. More acquisition steps are introduced to apply the TTL external pulse and could add more noise into imaging before the counts stabilize.

Next, the histograms of the cluster intensity and area were also calculated for comparison and are expressed in **Figure 44**. As shown in **Figure 44**, a steeper exponential-like decrease in counts as cluster intensity and area increases. This exponential decrease in counts occurs at cluster intensities less than 1.0×10^4 and cluster areas less than 160 pixels. Compared to the non-gated background histograms (**Figure 38**), the steeper decrease in counts detected in the gated-background histograms could also provide more insight into the rapid change in counts during acquisition using an external TTL pulse. It is worth noting that the maximum detected cluster intensity and the area is 42,326 counts and 390 pixels, respectively.

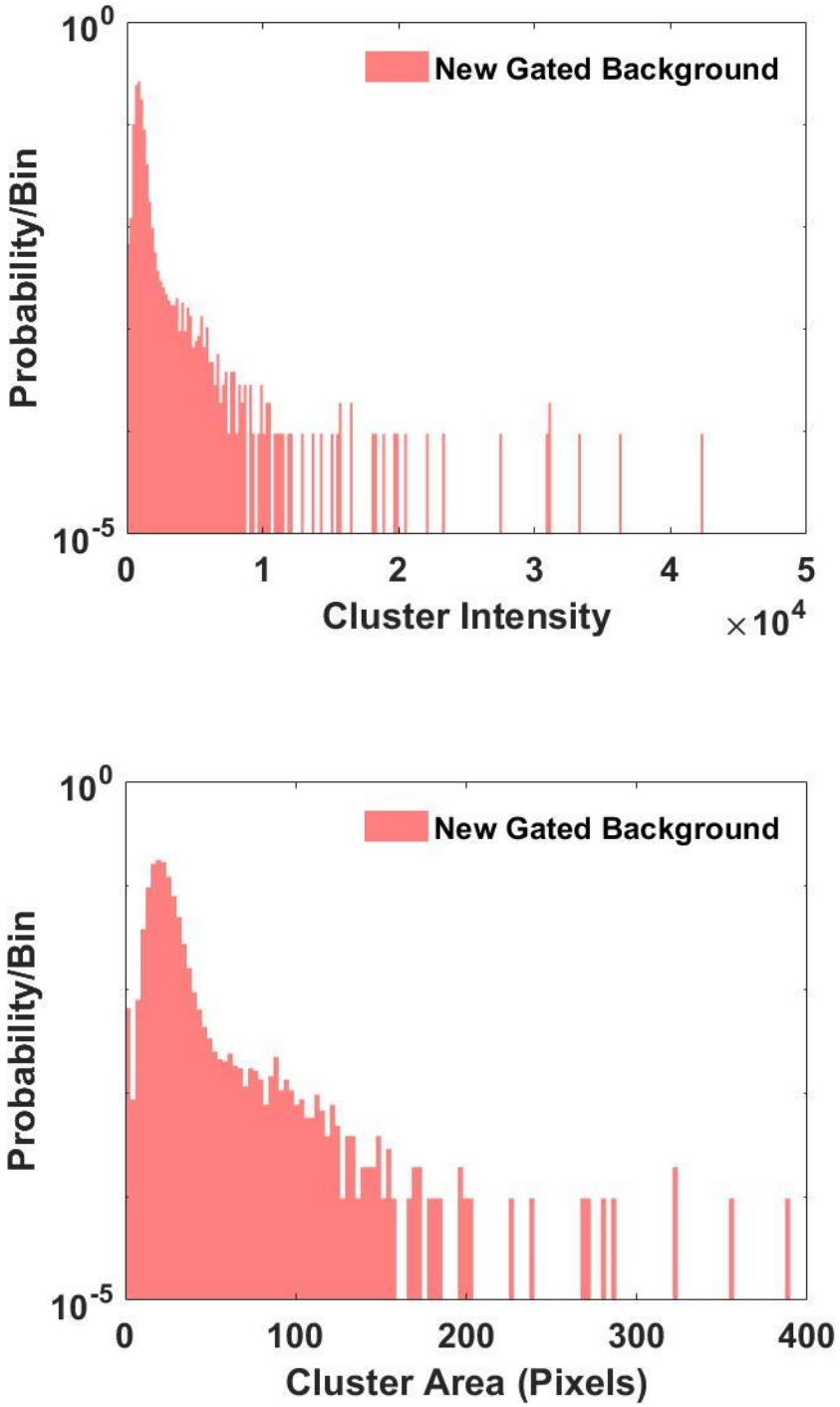

***Figure 44**: Histogram of cluster intensity (top) and cluster area (bottom) for new gated background measurement at 99% inverted polarity, 20 Hz, +5Vpp, +2.5V DC offset.*

iv) Gated ^{99}Tc Baseline Measurements

Similarly, count-rate ROI analysis was repeated for the gated ^{99}Tc measurements and compared to the ^{99}Tc non-gated measurements. These gated ^{99}Tc measurements were used further to characterize the gating component of the large-area iQID imager. As previously shown in **Figure 33**, ^{99}Tc was measured at 99% duty cycle with an inverted waveform polarity, 20 Hz gating frequency, +5Vpp, and +2.5V. In **Figure 45**, the gated ^{99}Tc centroid image detected a total of 27,358 detected counts or a total count-rate of 5,471.6 CPM. Using ROI analysis, this corresponded to a source and non-source ROI count-rate of 18,082 CPM and 2,335.6 CPM, respectively.

The average event-rate for the gated ^{99}Tc baseline was calculated and found to be 4.57 events per frame. As shown in **Figure 46**, the total event-rate over time for non-gated ^{99}T had a slight exponential decay. This is more apparent than the average event-rates calculated in non-gated and gated background measurements in **Figure 37** and **Figure 40**, respectively.

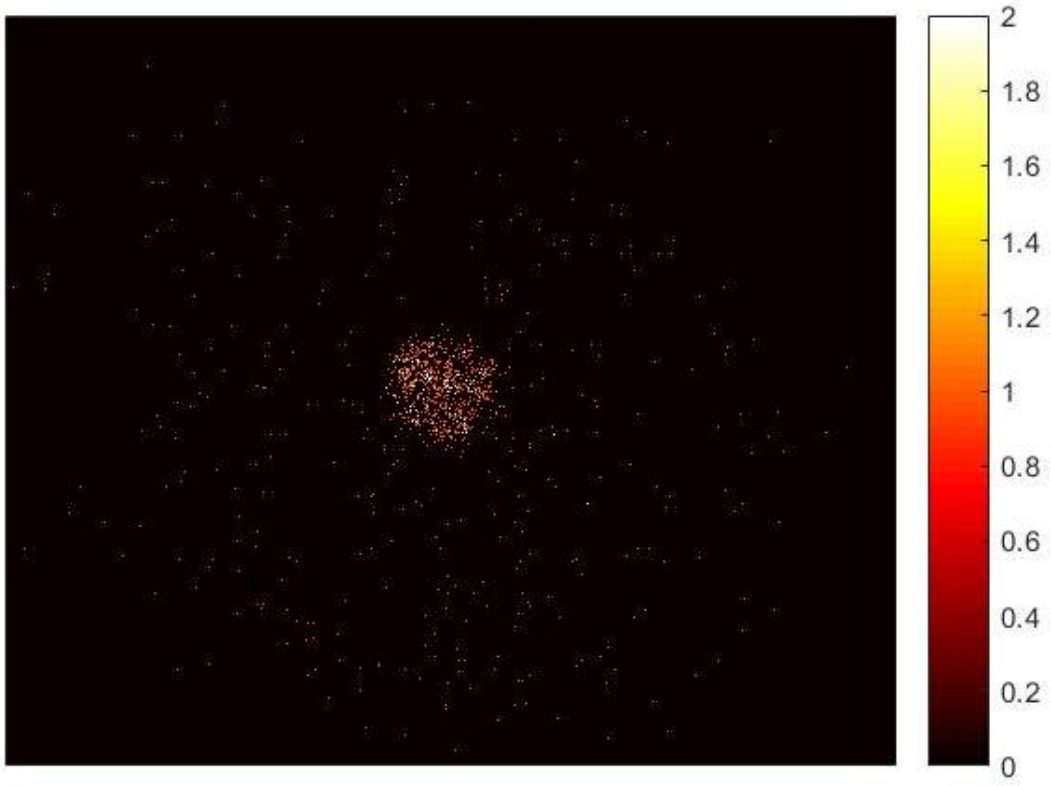

***Figure 45**: ^{99}Tc Centroid Image from the gated large-area iQID. Imaging occurred at a 99% duty cycle, receiving an inverted polarity gating signal of 20 Hz, +5 Vpp amplitude, and +2.5V DC offset.*

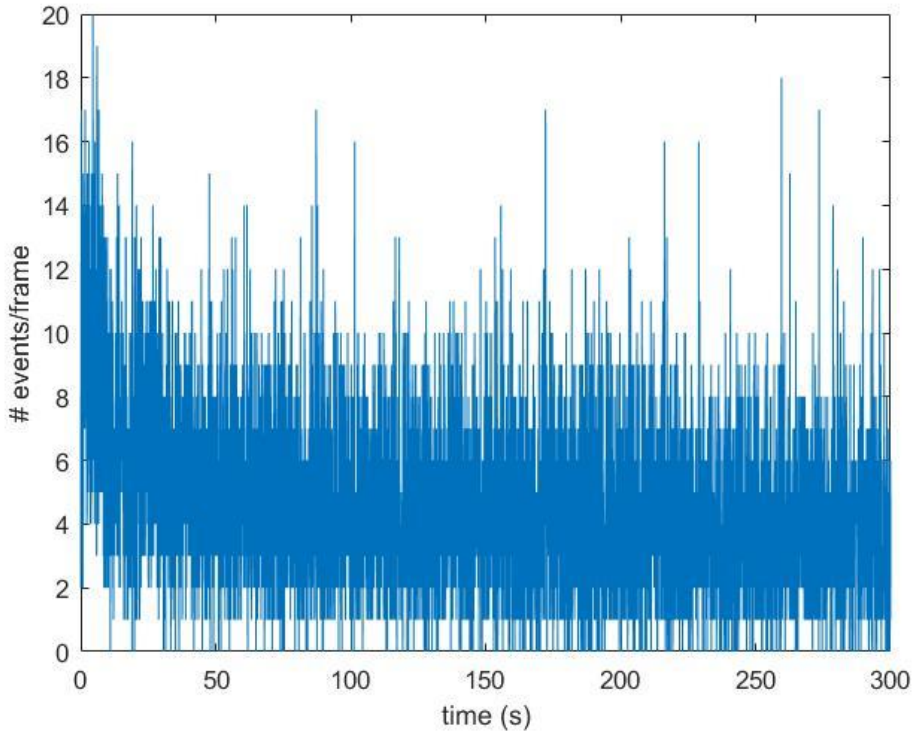

Figure 46: *Average number of events per frame detected within a 5-minute acquisition for the gated ^{99}Tc baseline measurement.*

To further investigate the effect of gating on count-rates, cluster intensity, and area histograms were calculated for the gated ^{99}Tc data. These histograms are expressed in **Figure 47**. According to the cluster intensity and cluster areas histograms, there seems to be a steep exponential decrease in counts. This occurs at cluster intensities less than 1.3×10^4 and cluster areas less than 250 pixels. Overall, all the cluster intensity and area histograms from the non-gated/gated background and non-gated/gated ^{99}Tc are summarized in **Table 8**.

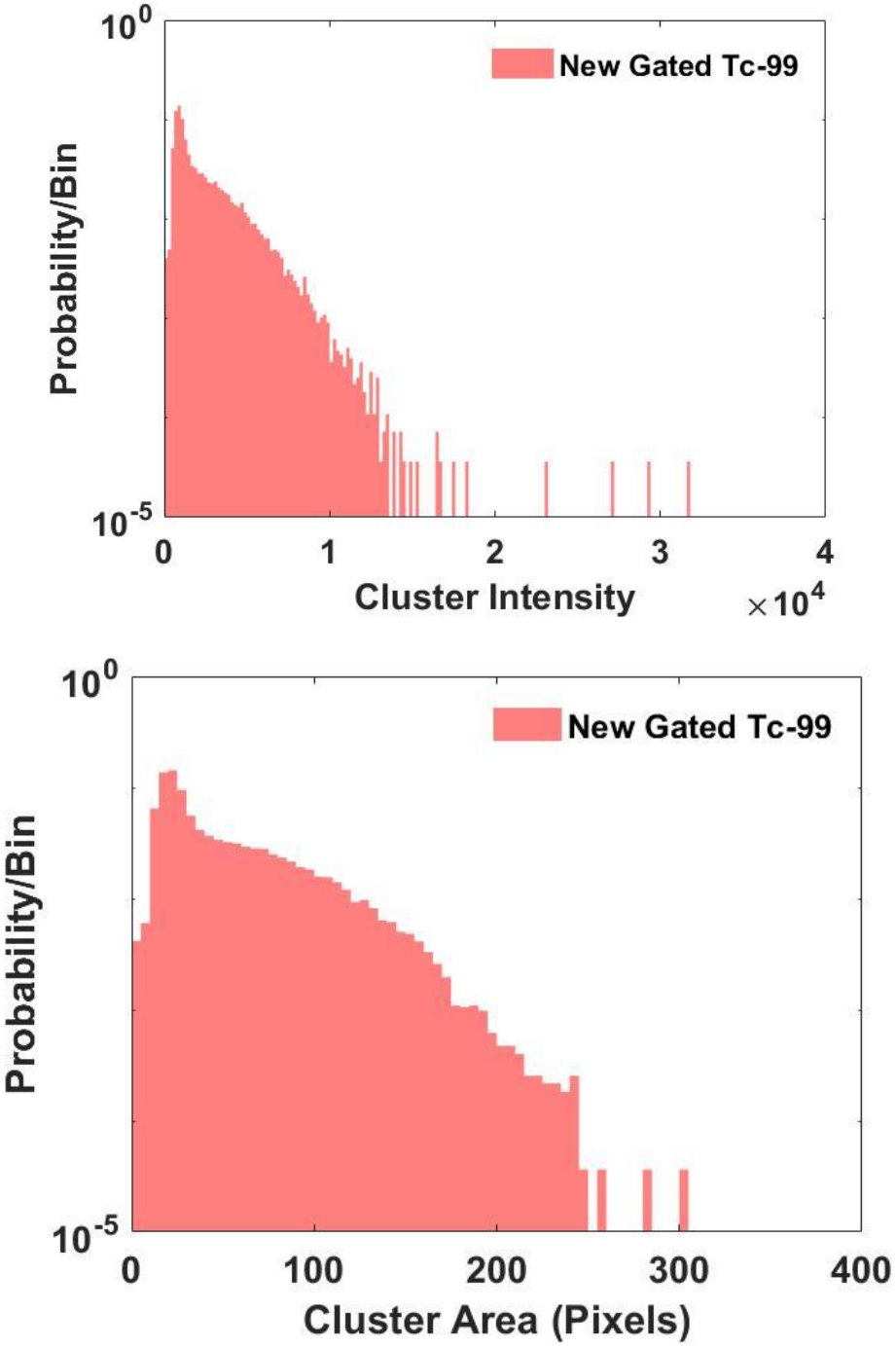

***Figure 47**: Histogram of cluster intensity (top) and cluster area (bottom) for new gated ^{99}Tc measurement at 99% inverted polarity, 20 Hz, +5Vpp, +2.5V DC offset.*

***Table 8**. Summary of the Cluster Intensity and Area Histograms for each Non-gated and Gated Measurement Setup*

	Non-gated Background	Gated Background	Non-gated ^{99}Tc	Gated ^{99}Tc
Cluster Intensity Peak Range [counts]	0 - 0.25 x10^4	0 - 0.75 x 10^4	400- 1,400	200 – 1.0 x10^4
Cluster Area Peak Range [pixels]	10 – 30	10 – 60	10 – 200	10 – 200
Location Exponential Trend [counts, pixels]	300 – 1,500 0-150	0 – 1.0 x 10^4 10 – 160	<1.5 x 10^4 <240	10 – 1.3 x10^4 <250

All the count-rate data was converted into **Figure 48** for simplicity to understand the gated image intensifier's characterization based on an inverted waveform polarity. As the duty cycle increased from 10% to 100%, the total count-rate for the new gated ^{99}Tc measurements also increased. This trend was similar for the ROI analysis of a 400 x 400-pixel area of the gated ^{99}Tc and non-source count-rates. Non-gated (yellow) and gated background (purple line) at higher count-rates had higher count-rates than previous background count-rates without a gated image intensifier. Higher detected background count-rates introduced by the gated image intensifier configuration translates to poorer MDA ranges. Likewise, the gated LAiQID could introduce higher background rates due to noise contribution from the new acquisition process from the external TTL pulse waveform generator. This is not concerning because the measured gated ^{99}Tc count-rate of 5,472 CPM at 100% duty cycle is fairly similar (~7.1% difference) to the newly calculated baseline ^{99}Tc count-rate 5,896 CPM.

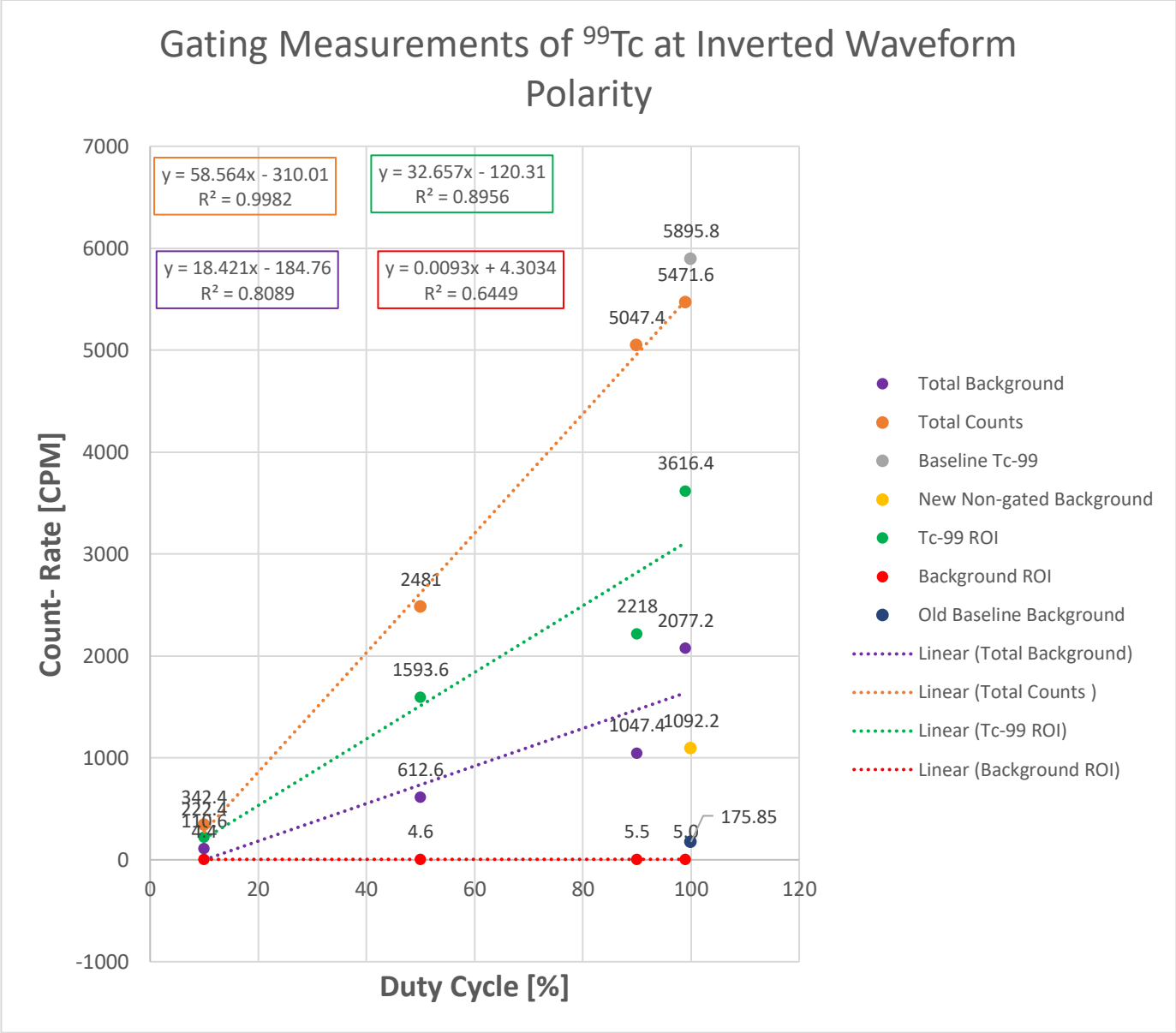

***Figure 48**: Results of count-rate in counts/minute vs. duty cycle in percent using ROIs for total, ^{99}Tc, and background counts at inverted polarity. Gray dot represents non-gated ^{99}Tc count-rate and orange dots are with gating.*

According to the vendor, Proxivision, the new gating configuration for the large-area iQID imager, should have an inverted polarity external TTL pulse. This means the highest detected count-rates should be at an inverted rather than normal wave polarity.

For characterization completeness, validation measurements were conducted at 10%, 50%, and 90% normal polarity (**Figure 49**). As expected, total count-rates decreased as the duty cycle increased to 100%. This demonstrated that the image intensifier is more inactive at a 100% duty cycle than a 10% duty cycle, not ideal for characterization.

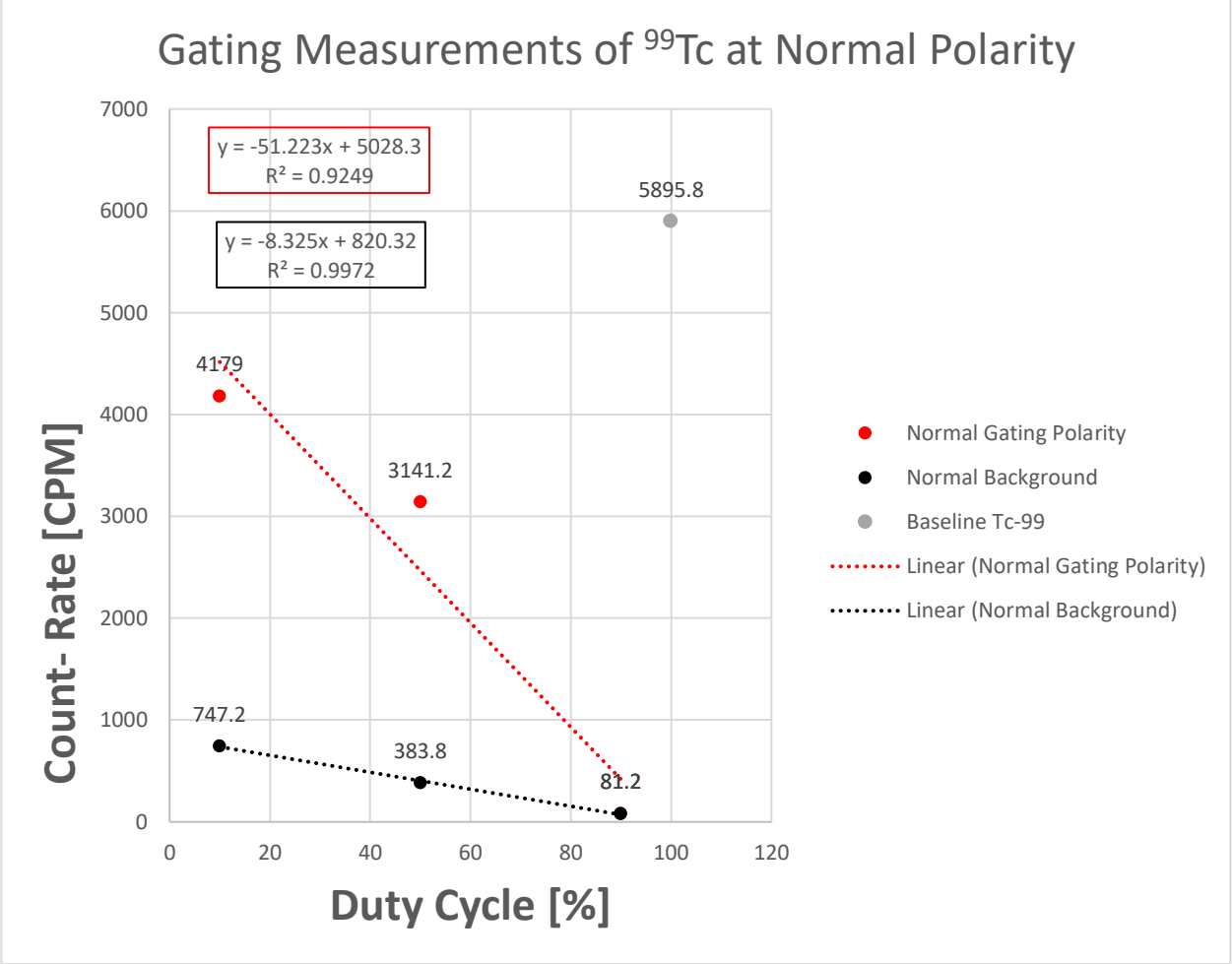

***Figure 49**: Results of count-rate in counts/minute vs. duty cycle in percent using ROIs for total, ^{99}Tc, and background counts at normal polarity.*

Furthermore, in **Figure 50**, the effect of normal and inverted polarity on the absolute efficiency of the large-area iQID imager. Absolute efficiency increased as the duty cycle increased with an inverted polarity than a normal polarity. With the new gated baseline absolute efficiency of ^{99}Tc at 25.6 % (lower than previous characterized results at ~30% in **Table 4**), the highest measured absolute efficiency was 3.9% at 100% duty cycle with inverted polarity. At normal polarity, the highest absolute efficiency is 18.25% at a 10% duty cycle.

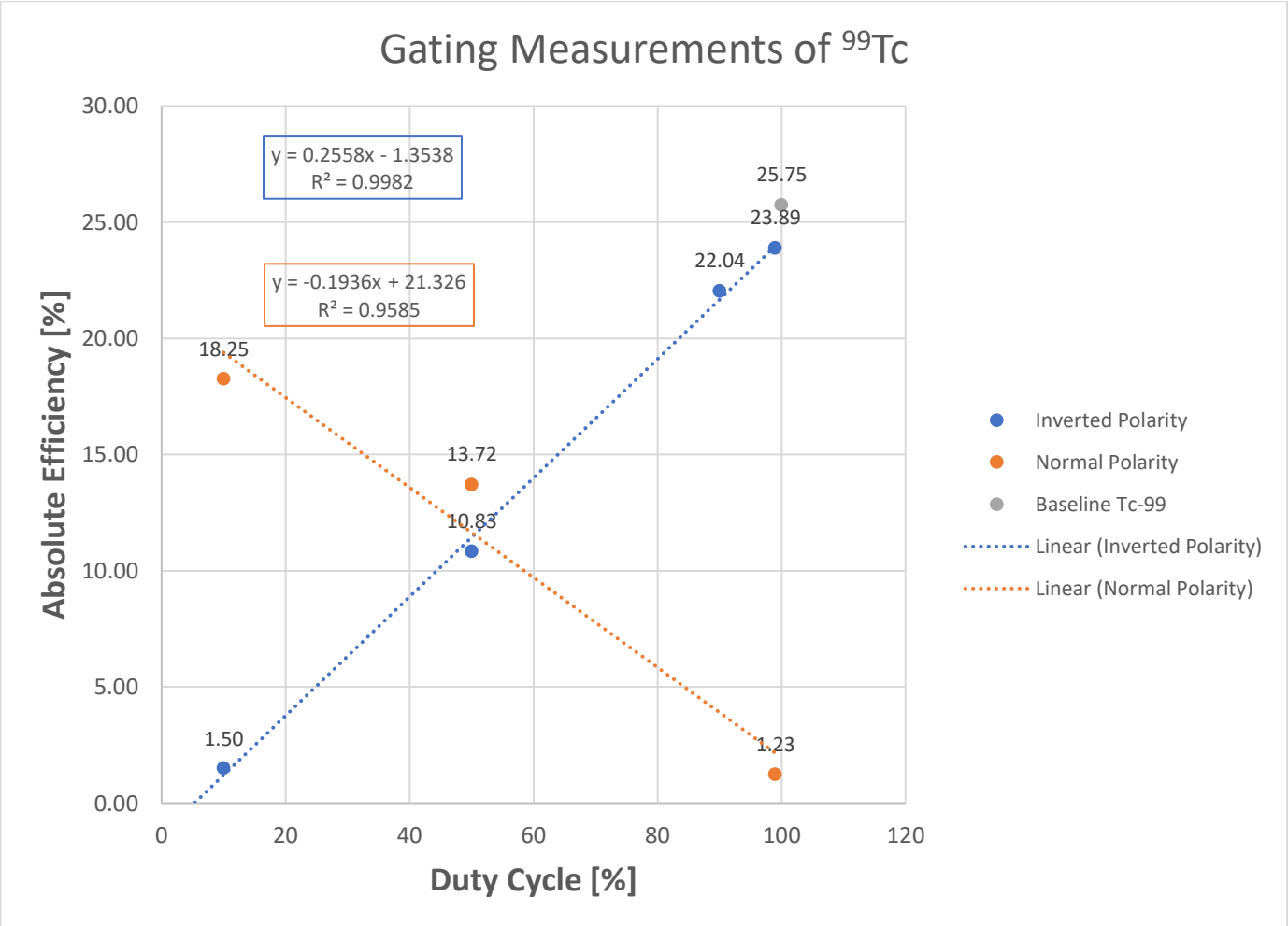

Figure 50: *Results of absolute Efficiency in percent vs. duty cycle in percent for total detected counts at normal and inverted gating polarities.*

4.2.1.C Results: Alpha Imaging Mode

New alpha imaging baseline background measurements of the gated large-area iQID imager were conducted to characterize the new system. All measurements were imaged for 5 minutes, and all ROIs consisted of 400 x 400 pixels in the centroid image. Unlike beta imaging mode, the CCD gain and image intensifier input voltage are reduced to 40 dB and 0.1V, respectively.

i) Non-gated Background Measurements

In **Figure 51**, the centroid image of the alpha non-gated background measurement was demonstrated with a total of 13 detected counts. This translates to a total count-rate of 2.6 CPM for the new alpha non-gated background measurements. The average event-rate for the alpha non-gated background was calculated and found to be 0.002 events per frame. As shown in **Figure 52**, the total event-rate during the full acquisition time varies between 0-2 events per frame. Event-rates in alpha imaging mode were less noisy, yet events occurred more temporally separately than beta imaging results.

***Figure 51**: Centroid image of the non-gated background measurement imaged in alpha mode with 13 total detected counts.*

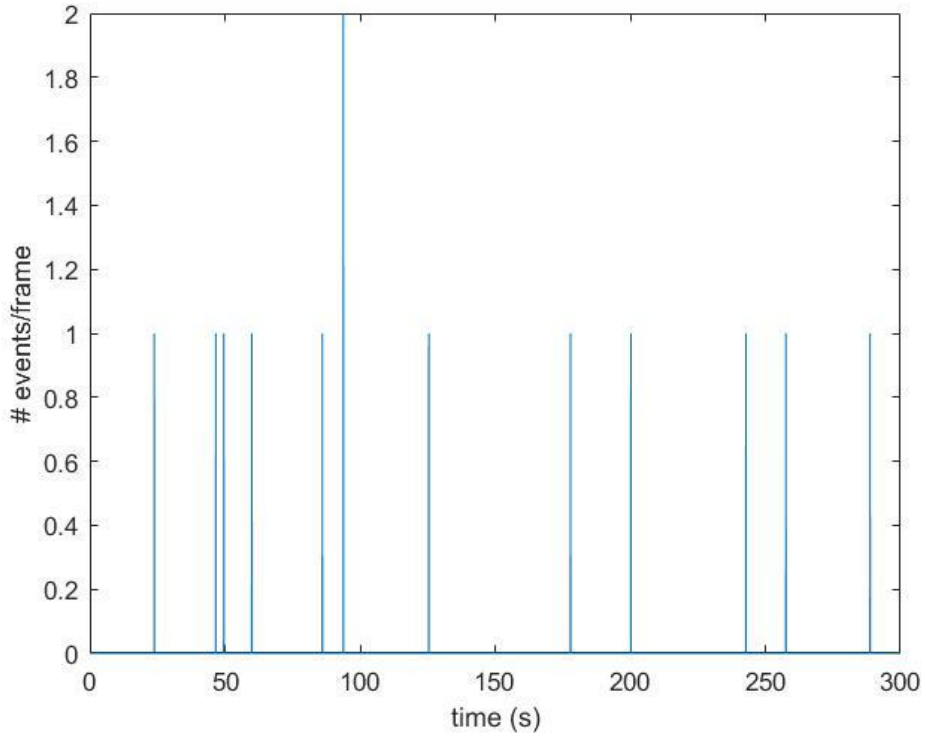

***Figure 52**: Total event-rate over 5 minutes for non-gated background measurement in alpha imaging mode.*

ii) Gated Background Measurements

Alpha gated background measurements were conducted and compared to the alpha non-gated background measurements above. These gated measurements were imaged at an inverted polarity, 20 Hz gating signal, +5Vpp, and +2.5V DC offset. The duty cycle was varied from 10%-99% to determine its effect on alpha background count-rate. As shown in **Figure 53**, total alpha background count-rates increased as the duty cycle increased for gated measurements. The highest alpha gated count-rate was found at a 90% duty cycle of 1.8 CPM. Alpha gated background count-rate was less than the new alpha non-gated background measurements at 2.6 CPM.

This gated count-rate for the alpha background was higher than the previous alpha background baseline of 1.1 CPM [9]. It should be noted that the alpha count-rate at 99% duty cycle was slightly less at 1.4 CPM.

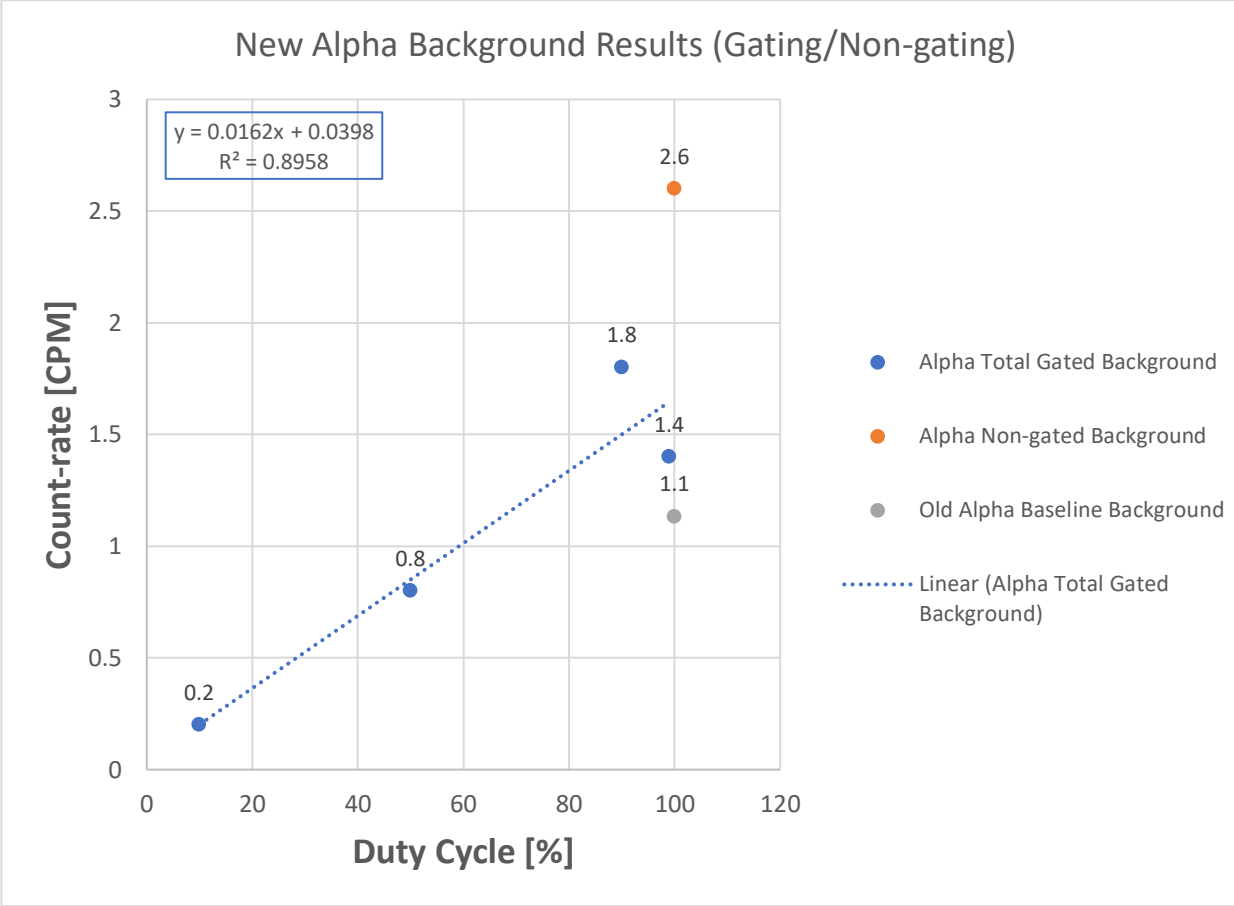

Figure 53: *Results of new background measurements imaged in alpha mode at different duty cycles*

Total event-rates for the full acquisition period at the different duty cycles were plotted. In **Figure 54**, total event-rates for 10% and 50% duty cycles were expressed and determined to vary between 0-1 events per frame. Events at a 10% duty cycle are detected within the first minute and a half. At 50% duty cycle, events are seen after the first 2-minutes.

In **Figure 55**, the total event-rates for 90% and 99% duty cycles are presented, which varies between 0-4 events per frame. Most events at 90% duty cycle occur within the full acquisition period (5 minutes), with the highest event-rate near 2 minutes. This is unlike the total event-rates detected in the 99% duty cycle. Most events are seen within the first minute of acquisition, with the highest event-rates within 10 seconds.

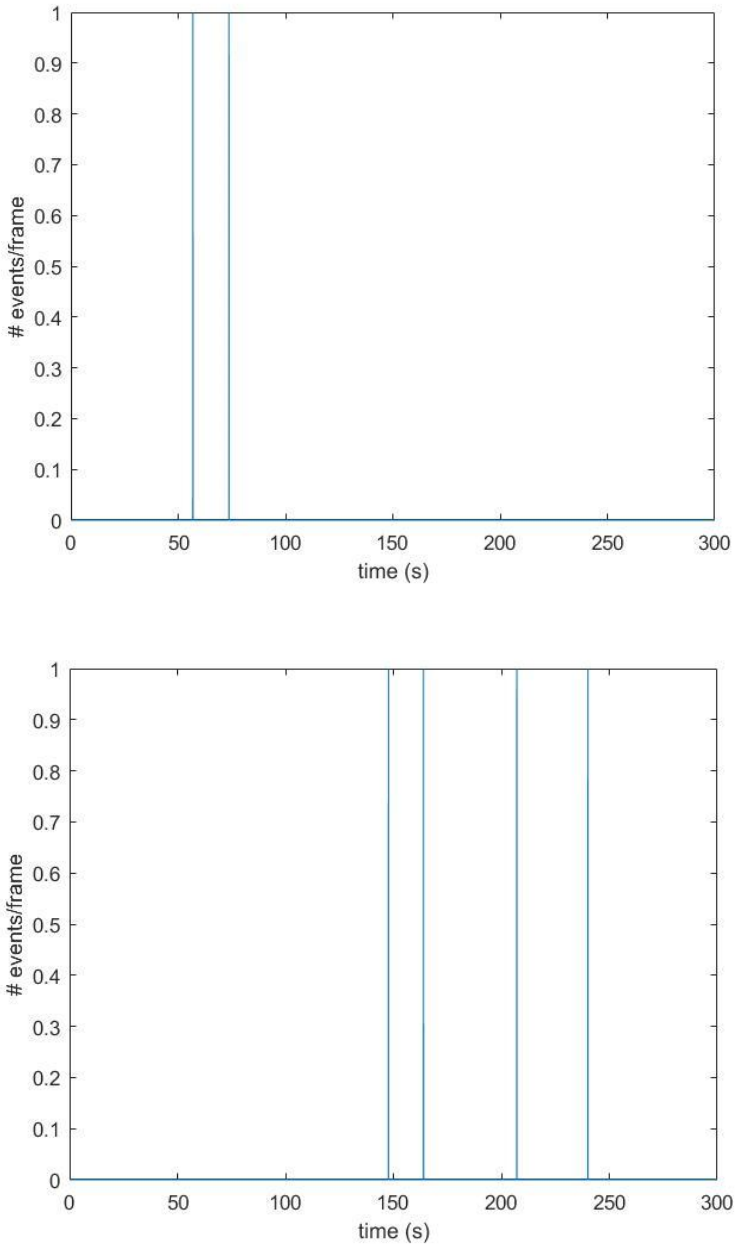

Figure 54: *(Top) Total event-rate during 5-minute acquisition at 10 % duty cycle. (Bottom): Total event-rate during 5-minute acquisition at 50% duty cycle.*

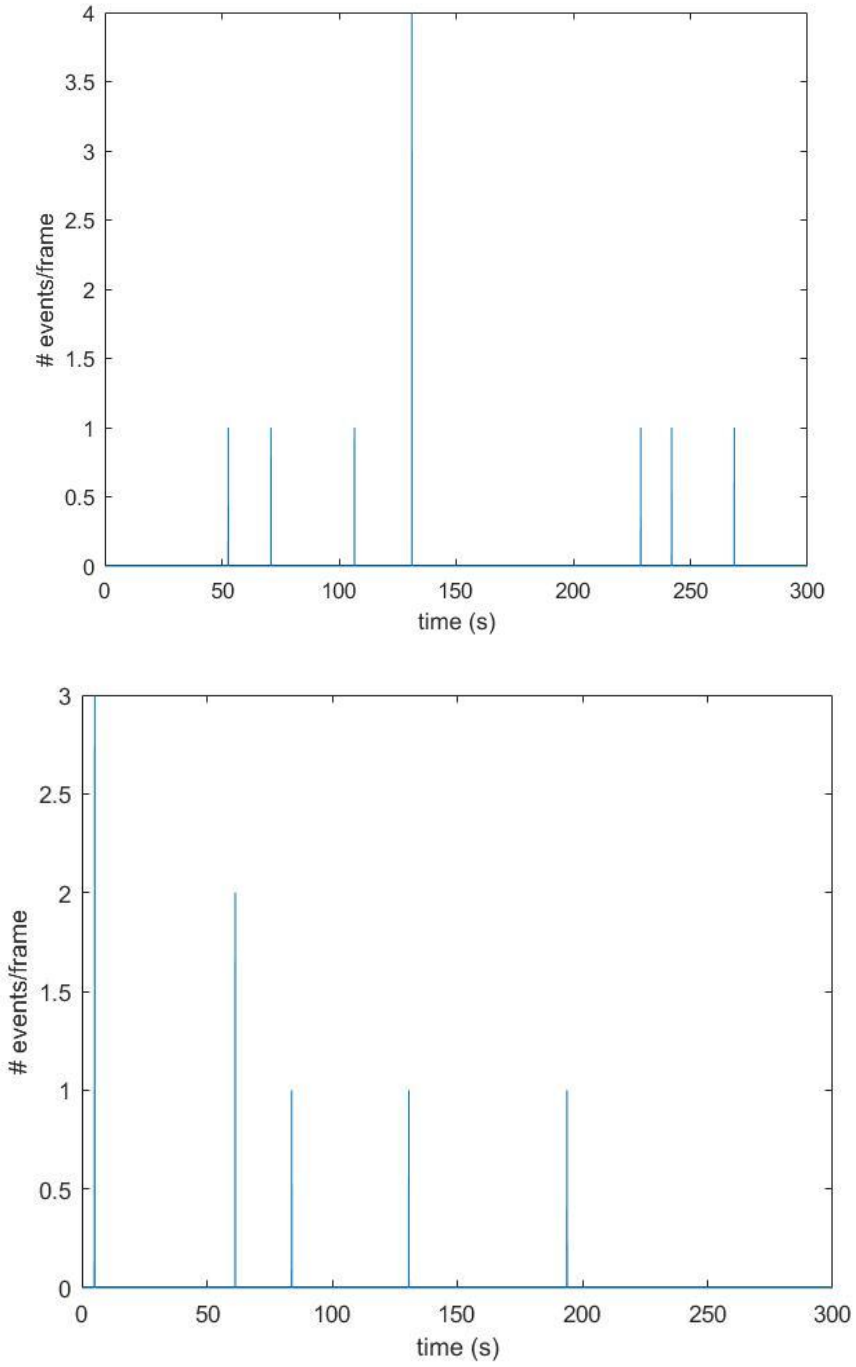

***Figure 55**: (Top) Total event-rate during 5-minute acquisition at 90 % duty cycle. (Bottom): Total event-rate during 5-minute acquisition at 99% duty cycle.*

Overall, all non-gated/gated background and source data with ROI analysis were summarized for both alpha and beta imaging modes and represented in **Table 9**.

Table 9: Results of ROI Analysis for Gated Inverted Polarity Measurements

Source	Duty Cycle [%]	Total Counts ROI [CPM]	Tc-99 ROI [CPM]	Background ROI [CPM]	Events per Frame [Averaged]
Beta Background	10	110.6	5.4	4.8	0.09
Beta Background	50	612.6	20.6	19.0	0.51
Beta Background	90	1047.4	37	40.8	0.23
Alpha Background	10	110.6	5.4	4.8	0.09
Alpha Background	50	0.8	0	0.0	0.00067
Alpha Background	90	1.8	3	1.0	0.00167
Alpha Background	99	1.4	0	0.0	0.00150
Tc-99	10	342.4	222.4	230.4	2.86
Tc-99	50	2481	1593.6	1573.8	2.08
Tc-99	90	5047.4	2218	2259.4	4.22
Gated Results					
Baseline Tc-99	99	5471.6	3616.4	2077.2	4.57
Baseline Beta Background	99	2077.2	115.6	114.6	1.74
Non-gated Results					
Baseline Tc-99	N/A (100)	5895.8	3839.4	318.12	4.93
Baseline Beta Background	N/A (100)	1092.2	11.6	10.6	0.92
Baseline Alpha Background	N/A (100)	1.4	0.0	0.0	0.00217
SORMA Results					
Previous Tc-99	N/A (100)	383.9	74.22	64.37	0.33
Previous Beta Background	N/A (100)	175.85	11.5	9.9	0.22
Previous Pu-239	N/A (100)	317.5			
Previous Alpha Background	N/A (100)	1.1			

4.2.1.D Discussion

The non-gated and gated measurements for the large-area iQID were necessary for two main reasons. Both sets of tests provided insight into the role of gating on the signal generation process of the large-area iQID. Furthermore, understanding gating's role also demonstrated the performance limitations of the image intensifier and CMOS readout device. Characterization measurements were conducted for both beta and alpha imaging modes. First, non-gated background measurements were compared to the gated background measurements imaged in beta mode. This comparison demonstrated how gating on the image intensifier contributed to count-rates detected by the large-area iQID imager.

Further insights regarding different scintillators' properties and performance limitations such as afterglow, light leakage, or extra electronic noise could be observed. For beta imaging mode results shown in **Table 9** and **Figure 48,** non-gated baseline background count-rates (1,092 CPM) were lower than gated background count-rates at 2,077 CPM. However, count-rates of the large-area iQID, before installing the TTL gating signal, were lower at 176 CPM than gated background measurements. Another interesting finding was the detected event-rate instability for the total event-rates for gated background and ^{99}Tc measurements, respectively (**Figure 43** and **Figure 46**). The fluctuation in event-rates (***Figure* 43**) for the gated background was similar to the instability in event-rates for ^{99}Tc measurements. However, the abrupt change in event-rates during the acquisition time of the gated ^{99}Tc measurements was larger than the event-rate difference in gated background measurements. These observed changes in total event-rates matched the steep instability in cluster intensity observed in (**Figure 44**) for gated background measurements. Similar instability trends in total event-rate changes and cluster intensity were observed in ^{99}Tc measurements (**Figure 47**).

For alpha imaging mode results (**Table 9** and **Figure 53**), non-gated and gated measurements were compared. Non-gated background count-rate at 2.6 CPM was higher than the total gated background count-rates at different duty cycles. The highest count-rate for the gated alpha background of 1.8 CPM was found at a 90% duty cycle. It should be noted that this new alpha gated background count-rate was higher than the previously reported non-gated alpha background measurement of 1.1 CPM [9]. This trend was similar to observations in non-gated and gated beta background measurements. This demonstrated that gating does increase count-rates overall because it is detected in both alpha and beta imaging modes. Yet, alpha gated background count-rates at 99% duty cycle were lower than alpha gated count-rates at 90% duty cycle of 1.4 CPM. Total beta event-rates for the full acquisition time at 90% and 99% duty cycle provided higher count-rates (**Figure 55**). Event-rates detected on the CMOS sensor were more temporally spread out in a 90% duty cycle than the 99% duty cycle. There were high average events per frame (2-3 events) peaks occurring within the first minute of the 99% duty cycle.

On the other hand, high average events per frame of 4 events occurred only at 2-minutes of 90% duty cycle. This observation was the opposite of what was observed in beta non-gated background measurements. The highest total gated background count-rates of 2077 CPM was detected at a 99% duty cycle. This beta gated background count-rate was lower than the beta non-gated background count-rate of 1092 CPM at a 99% duty cycle. Second, non-gated and gated ^{99}Tc were compared to determine the quality of performance and characterization of the new gated large-area. Despite an event/count instability in the gating background, quantitative imaging with gating was achieved. This was demonstrated as non-gated, and gated baseline ^{99}Tc had a similar total count-rate of 5,896 CPM and 5,472 CPM, respectively.

Likewise, the average events per frame were also identical between the non-gated and gated ^{99}Tc results with values of 4.93 and 4.57, respectively. This concludes that the gated large-area iQID was properly characterized despite minimal light leakage and event-rate instability.

Overall, these results of the gated image intensifier of the large-area iQID demonstrated its proper characterization. **Figure 48** and **Figure 53** shows the gated image intensifier's beta and alpha operation mode. Results showed the count-rate effect when the duty cycle is increased from 10% to 100%. As the duty cycle increased to a 100% duty cycle, the total count-rate of ^{99}Tc was 5,472 CPM, closer to the baseline ^{99}Tc count-rate of 5,896 CPM. This detected count-rate at 100% duty cycle was higher than the count-rate at 10% of 342 CPM. This was expected because the image intensifier was active for the full acquisition time of the CMOS shutter of 50ms at a 100% duty cycle. As the duty cycle decreased to 10%, the image intensifier was only active for 20% of the full acquisition time. Hence, it demonstrated a lower detected total count-rates. This was observed in gated background results conducted in alpha mode (**Figure 54**). In **Figure 54**, total events were seen within a minute and a half of the 5-minute acquisition period. This was approximately 20% of the full acquisition time. This leads to the finding that the proper experimental setup of the gated large-area iQID was at a 100% duty cycle at inverted polarity. Validation can be observed in **Figure 50** as the highest measured absolute efficiency of ^{99}Tc is 24% with an inverted polarity of 100% duty cycle. The new measurement baseline absolute efficiency for ^{99}Tc was 26% at the same settings.

4.2.2. Scenario 2: Linearity of count-rate versus source activity

Count-rates were compared to source activity as the frame-rate was increased up to 75fps. This would demonstrate how much source activity the large-area iQID can detect in the allotted measurement time. This was considered as a count-rate linearity test for the large-area iQID. The gated image intensifier was also used to limit the spatial pileup of a hot ^{241}Am source with an activity of 506 μCi.

4.2.2.A Methods

Based on previous characterization measurements for ^{241}Am (source ID 8251), theoretical calculations for the 506 μCi ^{241}Am source (source ID 15271) were conducted to determine the expected initial count-rate density. As depicted in **Figure *56***, a collimator ring was used during imaging with the 506 μCi ^{241}Am.

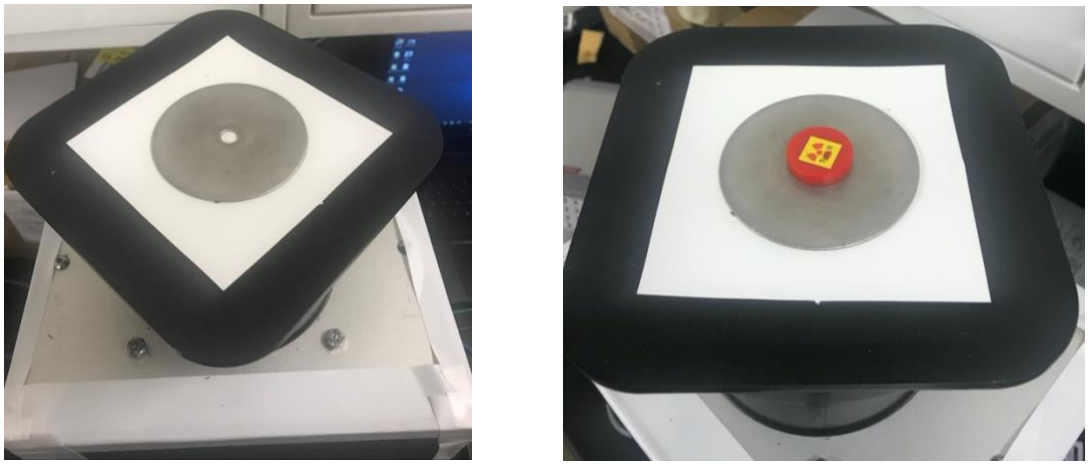

Figure 56: (Right) Image of the collimator ring and TranScreen LE scintillator used during high count-rate imaging on the large-area iQID with 506 μCi ^{241}Am sources. (Left): Image of collimator ring, TranScreen LE scintillator, and 506 μCi ^{241}Am sources used.

Total count-rate density incident on the large-area iQID and frame count-rate density detected on the CMOS sensor were calculated. This was achieved using the characterized absolute efficiency of 0.76% for ^{241}Am (source ID 8251) photon emissions. Experimental data of ^{241}Am (source ID 8251) was used to determine the optimal imaging settings to measure the ^{241}Am source (ID 15271) without gating. This first measurement test with ^{241}Am (ID 15271) was only attempted to reduce the CMOS sensor's count-rate density by changing the CMOS shutter time. CMOS frame-rate remained constant at 20 fps. CMOS shutter time was reduced from 49ms to reduce the number of detected spatial pileup events detected by the CMOS sensor.

It should be noted that the desired number for the spatial pileup was unknown. Therefore, an assumption regarding the acceptable amount of spatial pileup was made to determine whether quantitative imaging was achieved. The percent of a spatial pileup was selected as the imaging metric. Next, the 506 μCi ^{241}Am source (ID 15271) was imaged using the gated large-area iQID to reduce spatial pileup. This was tested by imaging ^{241}Am at a gating frequency of 20 Hz, gating amplitude of +5Vpp, and a +2.5V DC offset. The duty cycle was increased from 0.01% to 100%. Count density on the CMOS sensor (total and frame density based on the source imaging area) and spatial pileup were the metrics of comparison for the gated measurements.

4.2.2.B Results

Source information for two different activity ^{241}Am sources (IDs 8251 and 15271) are shown in **Table 10**. Data consisted of initial source emission rate and source activity from the source certificate, intrinsic Efficiency, solid angle, and adjusted source emission rate. The adjusted source emission rate was calculated using Equation 11 **Error! Reference source not found.** and expressed in **Table 10**. The decay constant was calculated as the inverse of the half-life (2.27 x 10^8 minutes) of ^{241}Am, and elapsed decay time was the amount of time the source has been allowed to decay at the time of measurement. The elapse time decay for both ^{241}Am sources (IDs: 8251 and 15271) is 16 years and 11 years, respectively.

$$Adj\ Emission\ rate = Intitial\ Emission\ Rate\ x\ e^{(-Decay\ constant\ x\ Elasped\ Decay\ Time)} \qquad \textbf{Equation 25}$$

The theoretical source activity of ^{241}Am (ID 15271) was calculated based on the characterized activity for ^{241}Am (source ID 8251) of 0.147 μCi. An activity scale factor of 51.2 uCi was theoretically calculated using the certified activities' ratios for both ^{241}Am sources. Using this activity scale factor, the theoretical activity for ^{241}Am (ID 15271) was estimated at 7.51 uCi.

***Table 10**. Source Information both ^{241}Am sources*

^{241}Am Source ID	Initial Emission Rate [gammas/minute]	Source Certificate Activity [uCi]	Elapsed Decay Time [minutes]	Adjusted Emission Rate [gammas/minute]	Intrinsic Efficiency [%]	Abs. Efficiency [%]	Solid Angle
15271	1.12E+09	505.73	5.78E+06	1.10E+09	1.6		5.88
8251	2.19E+07	9.875	8.41E+06	2.14E+07		0.76	

In **Table 11,** the initial source emission rate for both ^{241}Am sources was obtained from the source certificate and adjusted based on the total imaging area of the large-area iQID (100 cm^2). Based on the source certificate, the source active area per volume of the 506 uCi Am-241 source (ID 15271) was 5 mm (0.25 cm, 0.196 cm^2). This active area of ^{241}Am (ID 15271) was used to normalize the counts based on the source imaging area rather than the entire detector imaging area. Based on the active source area, the theoretical frame count density, scintillator flux, and the expected number of detections were calculated (**Table 11**). The expected number of detections provided a theoretical relationship to the spatial pileup. Likewise, the desired frame count density for Am-241 sources (ID 15271) was calculated as 1740 counts/frame*cm^2 based on measured source counts, measurement time, source imaging area, and frame-rate.

Table 11*. Theoretical Calculations for Spatial Pileup Analysis of ^{241}Am sources*

^{241}Am Source ID	**Initial Emission Rate per Total Imaging Area* [gammas/second* cm^2]**	**Initial Emission Rate per Source Imaging Area** [gammas/second* cm^2]**	**Frame Count Density [counts/frame*cm^2]**	**Scintillator Flux [gammas/ second]**	**Expected # of Detections [counts/second]**
15271	1.87E+05	5.73E+09	1.39E+04	1.08E+08	1.01E+07
8251	3.65E+03	1.12E+08	2.73E+02	2.10E+06	1.97E+05

*Based on the entire imaging area of the large-area iQID (100 cm^2)
**Based on ^{241}Am source 15271 imaging source area (0.196 cm^2)

i) ^{241}Am Experimental Data

Quantitative imaging with the large-area iQID was investigated using a 506 μCi ^{241}Am source. Count-rate and absolute Efficiency were the metrics for determining whether spatial pileup could be reduced. The effects of count-rate and CMOS shutter time for non-gating imaging results of a 506 μCi ^{241}Am were demonstrated in **Figure 57**. The count-rates for ^{241}Am exponentially increases as CMOS shutter time increases with a R^2 correlation value of 0.90. This was unexpected because the relationship between CMOS shutter time and the duty cycle is linear.

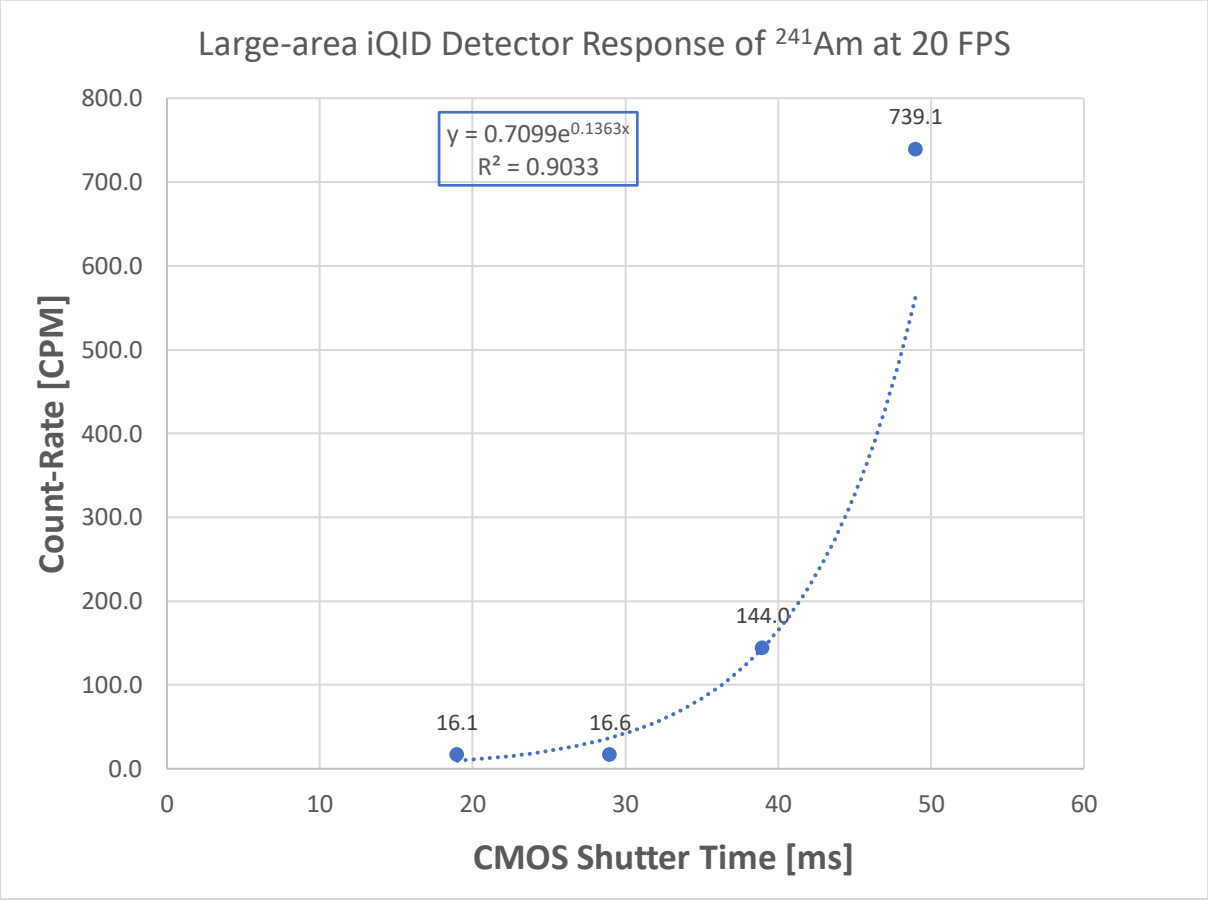

***Figure 57**: Non-gated imaging results with hot 241Am (505.73 μCi) and large-area iQID of count-rate in counts per minute vs. CMOS Shutter in microseconds.*

The highest detected count-rate for the 506 μCi ^{241}Am was 739 CPM during measurement at 49 ms CMOS shutter time. On the other hand, the lowest seen count-rate for 506 μCi ^{241}Am was 16 CPM with a shutter time of 19ms. These results were expected because the longer the CMOS shutter is open, the more scintillation light incident on the large-area iQID imager. The results of **Figure 57** can be view in **Table 12**.

Table 12. ^{241}Am count-rate results using the gated large-area iQID imager and different CMOS shutter times

Shutter	Live Time Fract	Corrected Total Counts	Total Counts	Source ROI Counts	Non-Source ROI Counts
49	0.98	45248	44343	22873	13521
39	0.78	11074	8638	8446	4762
29	0.58	3443	1997	1992	1240
19	0.38	5095	1936	1936	656

A similar analysis was conducted for gated measurements with 506 μCi ^{241}Am and expressed in **Figure 58**. This demonstrates the effects on count-rate as the duty cycle of the large-area iQID is increased from 10% to 99%. As expected, count-rates increased as the duty cycle increased. This trend was further observed in **Figure 59** as count-rates in the source ROIs increased, whereas the count-rates in the non-source ROIs decreased when the duty cycle increased.

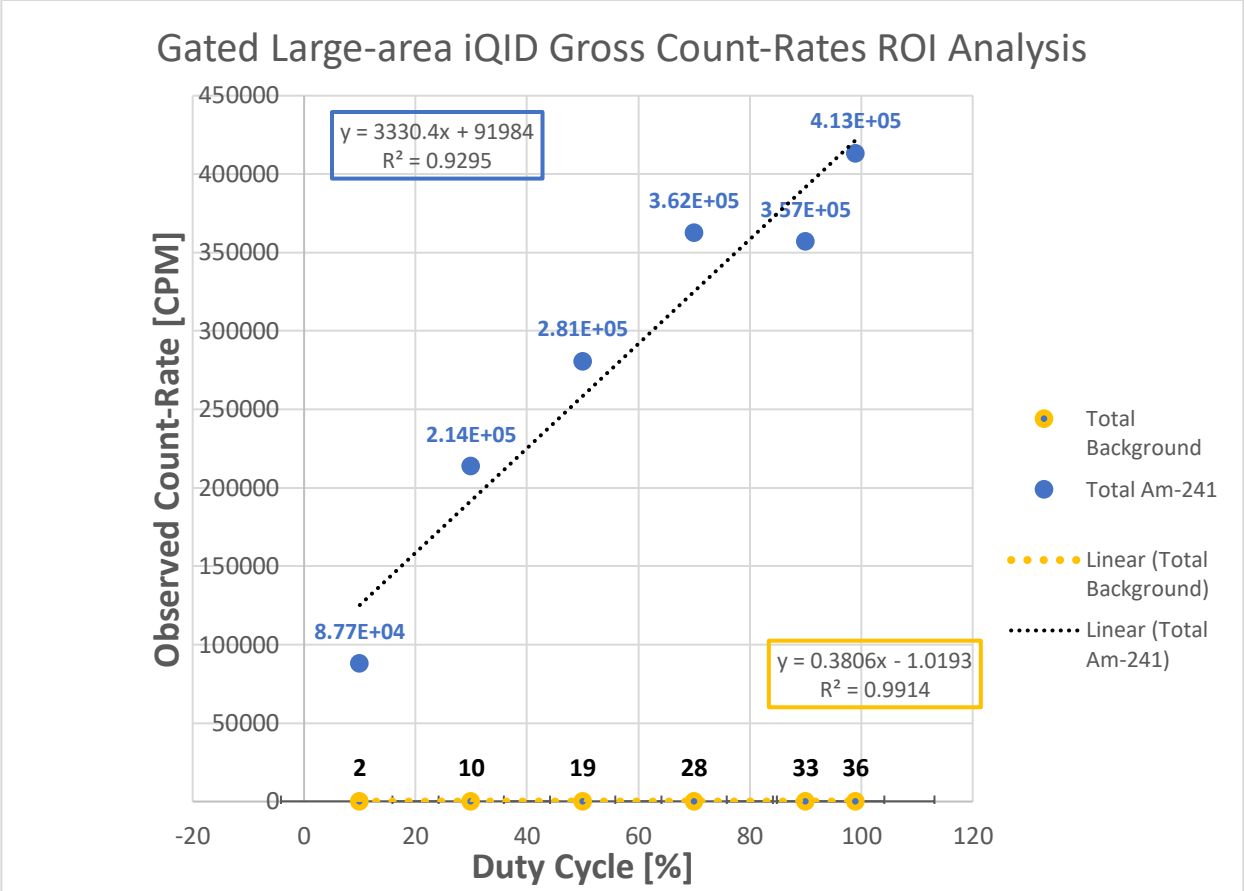

***Figure 58**: Gated imaging results with hot 241Am (505.73 μCi) and large-area iQID of observed count-rate in counts per minute vs. gated duty cycle in percent.*

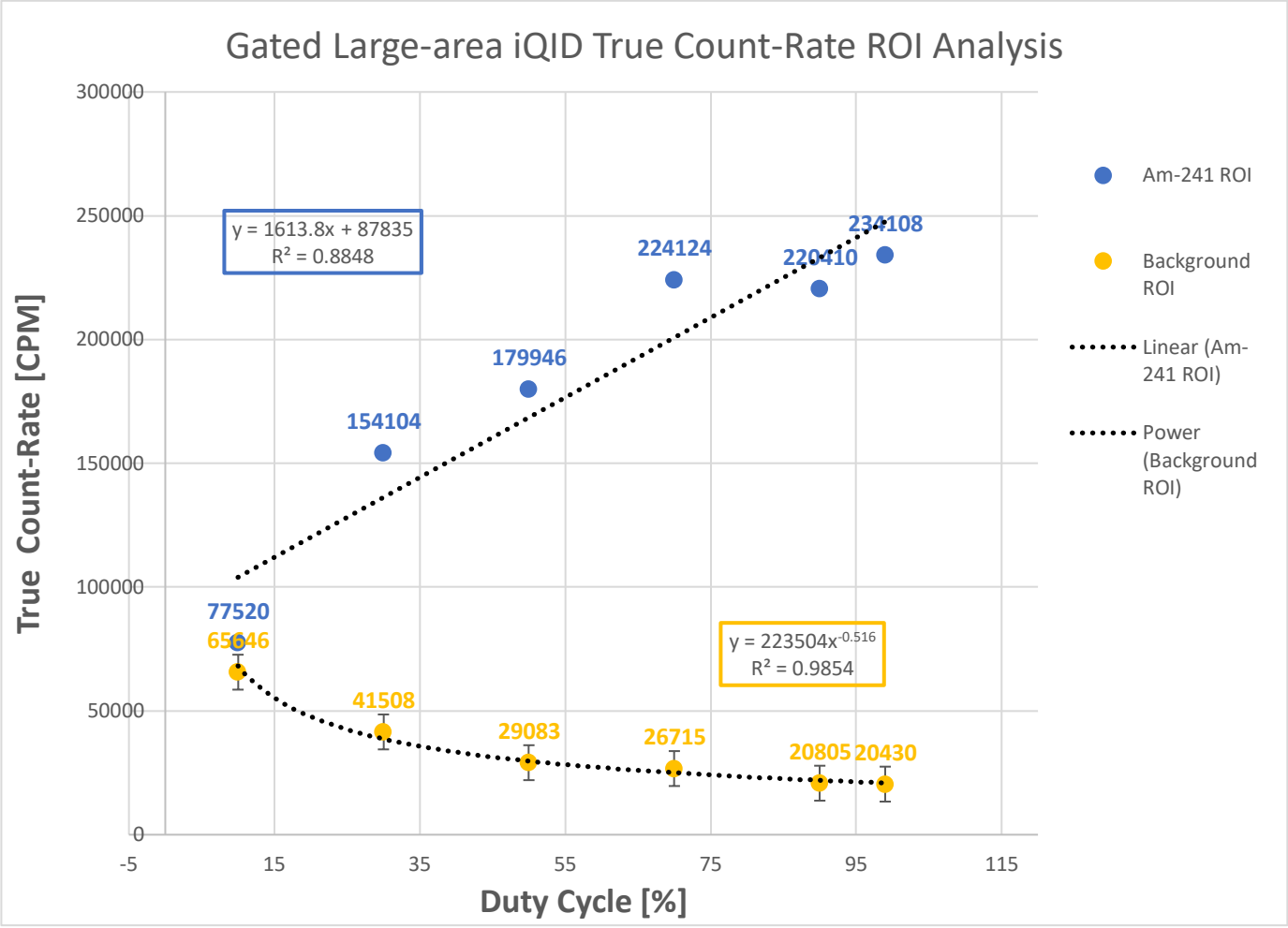

***Figure 59**: Gated imaging results with hot 241Am (505.73 μCi) and large-area iQID of true count-rate in counts per minute vs. gated duty cycle in percent. True count-rate corrected for system dead time*

One significant difference is that the count-rates increase linearly rather than exponentially, as in **Figure 57**. Additionally, gated count-rates are higher than the count-rates detected with the CMOS shutter time open for the longest time at 49 ms. In **Figure 58**, these results were observed at 50% and 99% duty cycle with detected count-rates of 1,029 CPM and 1,526 CPM.

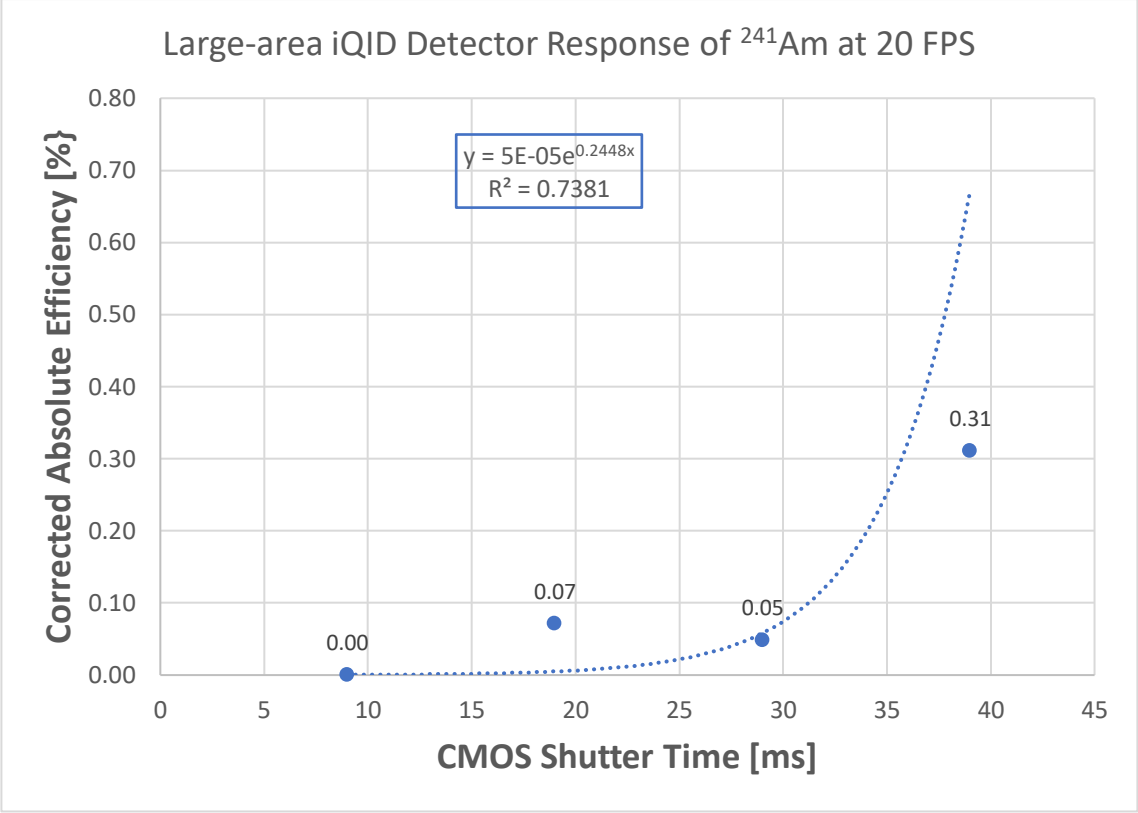

Figure 60: *Non-gated imaging results with hot ^{241}Am (505.73 uCi) and large-area iQID of absolute Efficiency in percent vs. CMOS shutter time in microseconds. Absolute Efficiency was live time corrected.*

The next analysis regarding quantitative imaging with the non-gated large-area iQID was investigated in terms of absolute Efficiency. As the CMOS was exposed to light for a longer time frame, absolute efficiency increases (**Figure 60**). Absolute efficiency was corrected based on the time in which the CMOS is open or "live". The highest detected absolute efficiency for 506 μCi ^{241}Am was measured at 0.31 %. This absolute Efficiency was lower than the baseline measurement for 506 μCi ^{241}Am of 0.76%. Therefore, gating was applied to the large-area iQID to determine its effect on absolute efficiency. This was achieved by increasing the duty cycle from 10% to 99%. In **Figure 61**, it was found that absolute efficiency increased as the duty cycle increased during imaging with the gated large-area iQID. The highest detected absolute efficiency with the gated large-area iQID was 1.29%. One exciting result was all absolute efficiencies with the gated large-area iQID imager were higher than the absolute baseline efficiency for 506 μCi ^{241}Am.

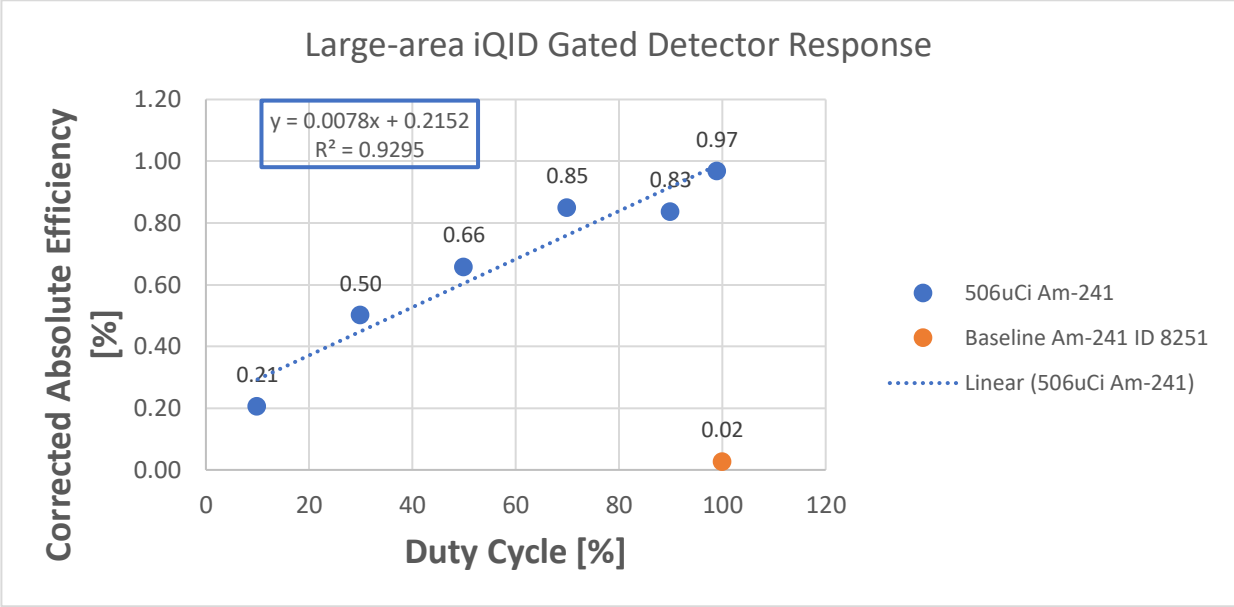

***Figure 61**: Gated imaging results with hot ^{241}Am (505.73 μCi) and large-area iQID of absolute efficiency in percent vs. duty cycle in percent. Absolute efficiency data is corrected based on dead time and observed counts.*

The last metric analyzed for quantitative imaging was experimental spatial pileup for gated large-area iQID imager. This was achieved by comparing the percent of pileup events to frame count-density incident on the CMOS sensor. In ***Figure 62***, the percent of pileup events linearly increased as frame count-density increases for the gated large-area iQID. This was represented with a R^2 correlation of 1. The relationship expressed in ***Figure 62*** was successful and expected because as more event clusters were detected on the CMOS frame, the higher the chances of pileup events.

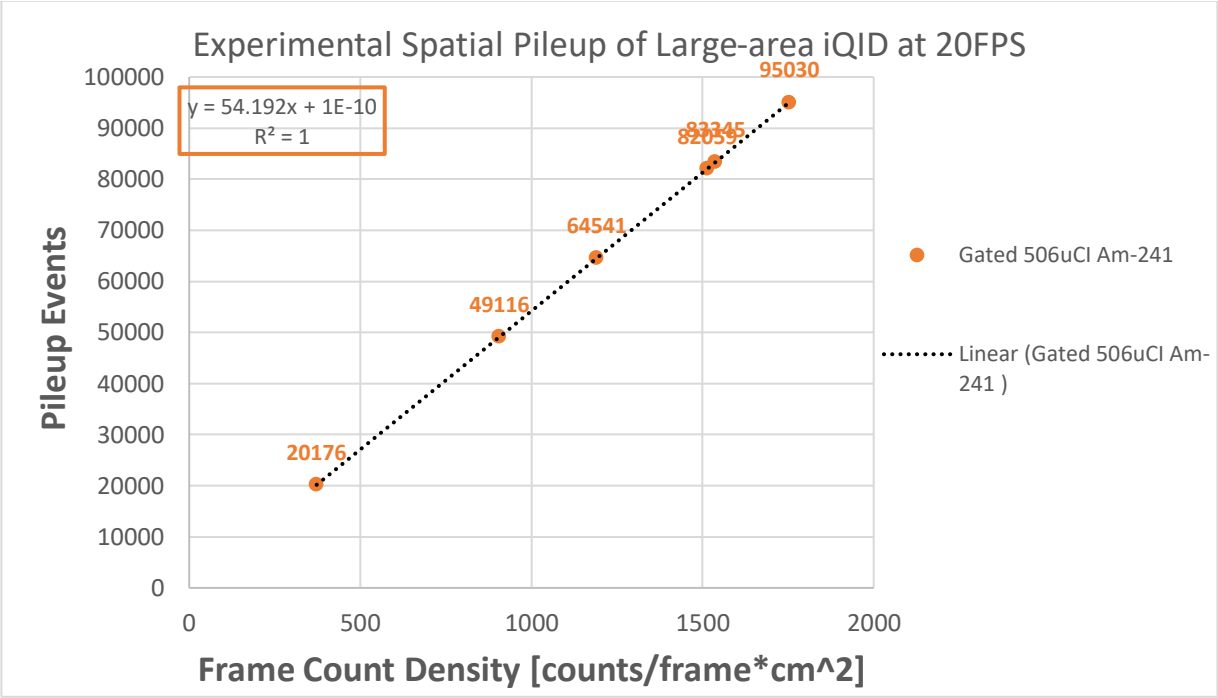

Figure 62*: Imaging results with hot ^{241}Am (505.73 μCi) and large-area iQID of detected pileup events in percent vs. frame count density in counts per frame and source area. ^{241}Am source area is 0.196 cm^2.*

Lastly, the duty cycle was reduced lower than 10% to determine its effect on the capability to quantitative image a hot source with the gated large-area iQID imager.

Using the ^{241}Am source (506 μCi), the idea was to induce spatial pileup and determine if the post-processing algorithm could allow successfully capture a centroid image indicative of the source. The source was placed directly on the TranScreen LE scintillator in a 2π geometry. To test the hot ^{241}Am source's quantitative imaging on the large-area iQID imager, measurements were calculated at duty cycles reducing from 5% to 0.01%. In **Figure 63**, the centroid image of the hot ^{241}Am source was processed and demonstrated missing counts in the ^{241}Am source center. At a duty cycle of 5%, imaging of the hot ^{241}Am source was unsuccessful and not quantitative because the iQID system was not adequately detecting all the counts emitted from the source.

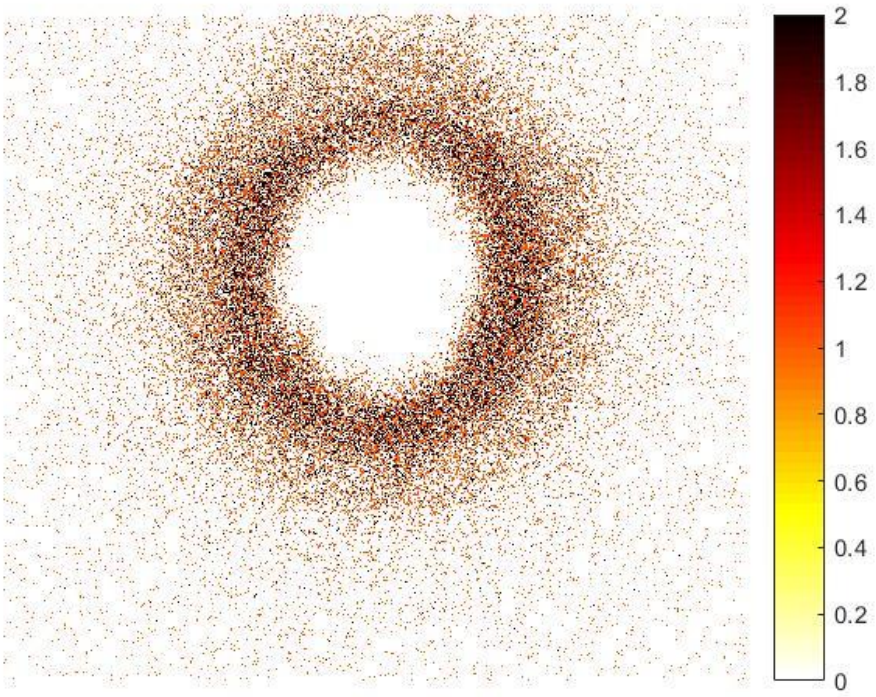

***Figure 63**: Imaging gated large-area iQID measured at a 5% duty cycle with a hot ^{241}Am source (506 μCi).*

Next, in **Figure 64**, the ^{241}Am hot source was imaged at a 1% duty cycle. Counts are detected in the center of the missing source when reflected at a 5% duty cycle. This imaging is seeing the majority of the counts emitted from the hot ^{241}Am source. Hence, no event clusters are being missed by the CMOS sensor or thrown out via the MATLAB post-processing algorithm. In **Figure 64**, imaging would be considered quantitative and successful.

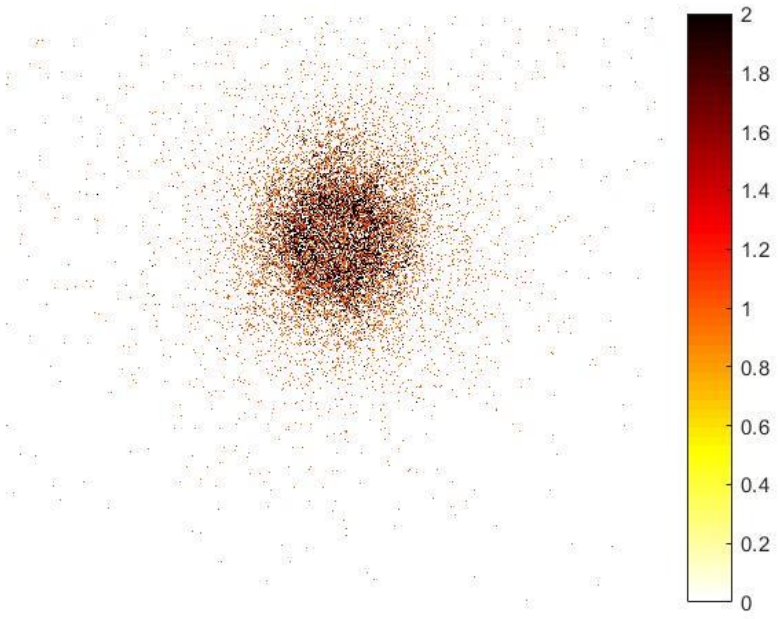

***Figure 64**: Imaging gated large-area iQID imager results measured at a 1% duty cycle with a hot ^{241}Am source (506 μCi).*

The gated large-area iQID imager also imaged the hot ^{241}Am source at a 0.1% duty cycle. This was demonstrated in **Figure 65**. In this figure, the hot ^{241}Am source's center was also detected, but fewer counts are surrounding the center of the source. This could be due to the CMOS sense missing counts or counts thrown out in the MATLAB post-processing algorithm. Quantitative imaging with the hot ^{241}Am source was more successful at a 1% duty cycle.

When the duty cycle was lowered to 0.1%, it demonstrated the performance tradeoff between the CMOS sensor and the post-processing algorithm. The CMOS sensor is detecting emitted counts or limitations in the post-processing algorithm to detect and image all the counts emitted during the acquisition period.

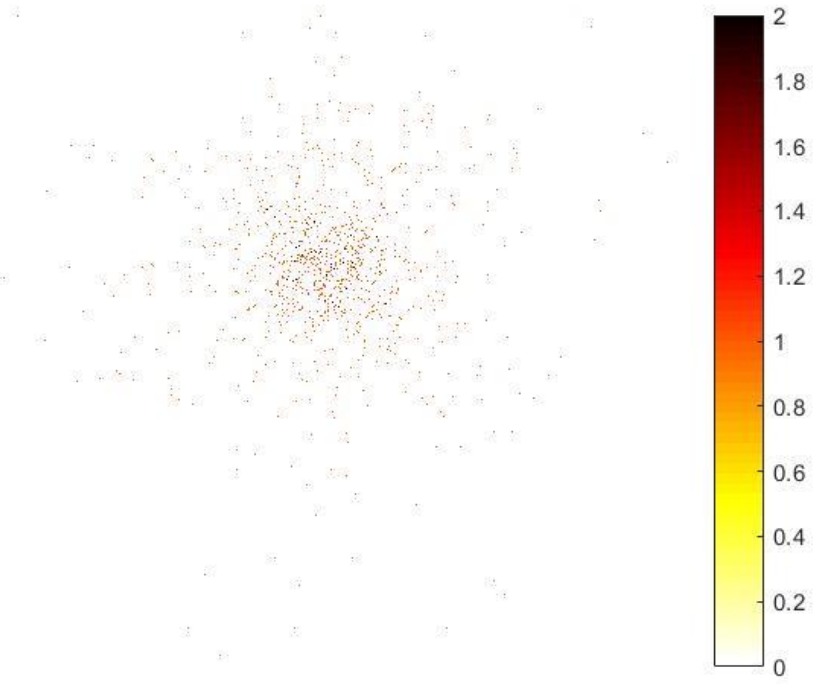

***Figure 65**: Imaging results of gated large-area iQID imager measured at 0.1% duty cycle with ^{241}Am source*

Lastly, the hot ^{241}Am source was imaged at 0.01% duty cycle and was demonstrated in **Figure 66**. Several counts were missing or thrown out via the post-processing algorithm at this duty cycle. Therefore, the duty cycle of 0.01% was too short to quantitatively and adequately imaging the 506 μCi ^{241}Am source.

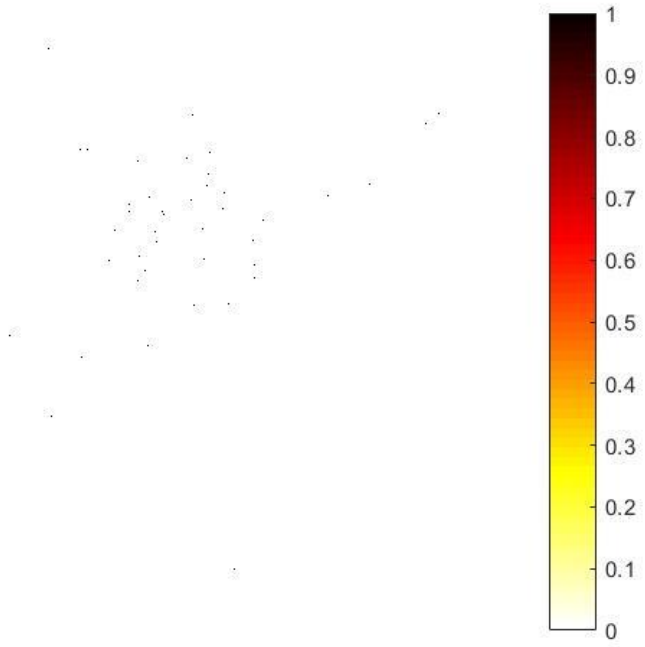

***Figure 66**: Imaging results of gated large-area iQID measured at 0.01% duty cycle with ^{241}Am source*

The quantitative imaging of the gated configuration of the large-area iQID imager was evaluated based on detected counts and activity. In **Figure 67**, the relationship between measured counts and activity was demonstrated using a hot ^{241}Am (506 μCi) and ^{99}Tc (~10 μCi) sources. This plot showed what range of activities could gated configuration of the large-area iQID imager detect. As expected, there is a linear relationship between measured counts and activity for either low-energy gammas or mid energy betas from ^{241}Am and ^{99}Tc, respectively. For the hot activity ^{241}Am source, all detected counts were less than 2 x 10^{-3} μCi, with the highest detected counts of 89,815 counts. On the other hand, for the beta ^{99}Tc source, there was a wider span of activities detected with the highest at 27,358 counts between 6-8 x 10^{-3} μCi.

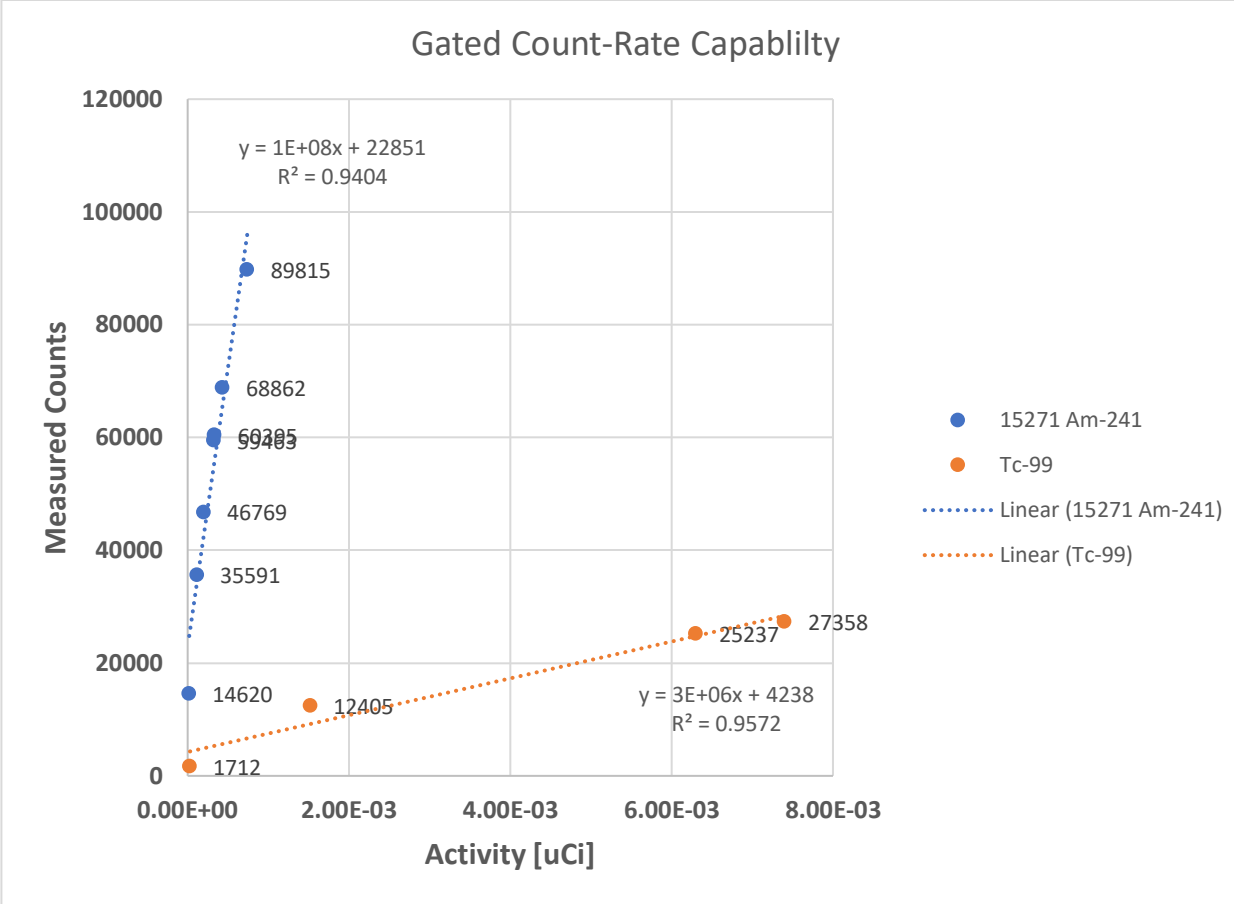

***Figure 67**: Results of measured counts vs. activity using a hot ^{241}Am (506 μCi) and ^{99}Tc sources on the gated configuration of the large-area iQID imager*

4.2.2.C Discussion

Count-rates and the capability of quantitative imaging with the large-area iQID imager were investigated in this chapter. This was achieved by testing two different types of configurations, which consisted of without and without gating on the image intensifier. Since the gated arrangement was a new setup for the large-area iQID, characterization measurements were required before imaging ^{99}Tc source data. It was determined that the count-rates detected in the non-gated background configuration (1,092.2 CPM) were lower than the gated background configuration (2,077.2 CPM) in beta imaging mode. This was demonstrated in **Figure 36** and **Figure 42**, respectively. It was also determined the non-gated ^{99}Tc count-rates (5,895.8 CPM) were higher than the gated ^{99}Tc source count-rate (5,471.6 CPM). This was demonstrated in **Figure 39** and **Figure 45**, respectively. Characterization of the gated large-area iQID imager was tested at both normal and inverted wave polarity to determine which setup detected the highest count-rates (**Figure 50**). Based on the vendor recommendation, it was hypothesized that the inverted wave polarity would produce the highest count-rates. This was tested with a ^{99}Tc source and validated in **Figure 50** in which the absolute Efficiency was highest at an inverted polarity. Likewise, the highest count-rates were calculated at an inverted polarity and demonstrated in **Figure 48**.

Quantitative imaging with the large-area iQID imager was evaluated using a hot ^{241}Am source (506 uCi) and a gated image intensifier. The purpose was to induce spatial pileup on the scintillator and determine if the CMOS sensor could properly detect counts without missing actual event clusters. Since the gated image intensifier could control the pulse width via the duty cycle, the scintillation light sampling could also be held. The duty cycle was reduced from 100% to 0.01%, and successful quantitative imaging was based on how the centroid image appeared after post-processing.

It was determined that a duty cycle of 1% could appropriately image the incident flux of 506 μCi ^{241}Am source. This can be seen in **Figure 64**. Duty cycles lower than 1%, such as 0.1% (**Figure 65**) and 0.01% (**Figure 66**) removed/missed necessary event clusters emitted from the 506 μCi ^{241}Am source. An additional evaluation of quantitative imaging with the gated configuration of the large-area iQID imager was also tested by determining the range of activities and detectable counts. This evaluation was demonstrated in **Figure 67**. It was determined that the low to medium energy betas had a more comprehensive range of observable activities and counts when using a ^{99}Tc of ~10 μCi.

On the other hand, low energy gammas were detected at a lower activity range despite using a very hot ^{241}Am source at 506 μCi. This means the gated large-area iQID had a greater chance for quantitative imaging for low-medium energy betas than low energy gammas. However, if the duty cycle was lowered to 1% when imaging the hot ^{241}Am source, then the detectable counts and activity range may have been higher.

Chapter 5

Additional Imaging Studies of iQID

This chapter will demonstrate a brief overview of further imaging studies conducted with the large-area iQID imager. These studies were performed during this dissertation but out of the scope of the proposed work. Particle and energy discrimination of beta and gamma events with the large-area iQID imager, if achieved, would enhance its imaging characteristics to be useful in the safeguards field and other applications. This hypothesis is based on the performance benefits and increased imaging area of the large-area iQID mentioned in Chapter 2. Methodology and results for particle and energy discrimination with the large-area iQID imager will be presented. Particle and energy discrimination with the large-area iQID can be based on three post-processing metrics: cluster eccentricity, cluster intensity, and cluster area. Cluster eccentricity is based on the shape of the event clusters. Cluster intensity is related to how energy is deposited and detected within the scintillator and the large-area iQID. Cluster area is defined as how dispersed or spread-out energy is collected within the scintillator and large-area iQID imager. In a previous iQID system, some elongated clusters were observed in a phosphor screen, and cluster eccentricity was solely used as a metric for particle discrimination (See Appendix). It was hypothesized that these events were beta particle interactions. This system did not include a fiber optic taper and used a different phosphor screen (Columnar CsI) than screens used with the large-area iQID. This study also suggested scintillation light blurring could occur through the taper of the large-area iQID imager. If this statement is true, then event cluster information such as shape could be distorted. This would make distinguishing beta and gamma events rather challenging.

Therefore, hypothesized beta tracks could be observed with the large-area iQID when using columnar CsI:Tl as light would be trapped to individual columns as beta particles traversed across them. However, in this dissertation, Columnar CsI was not a scintillator option. Section 5.1 **below** of this dissertation will investigate the possibility of beta and gamma particle discrimination with the large-area iQID imager and TranScreen LE phosphor screen.

The next imaging study was expressed in Section 5.2 below**;** a post-processing MATLAB algorithm was created based on image co-registration with the large-area iQID. This algorithm was able to successfully co-register a photograph of a sample and an autoradiograph made on the large-area iQID. The methods and results of this algorithm were presented **below**.

The last imaging study with iQID was involved imaging electrostatically-collected air deposited on a sample. Room air contains beta and gamma daughter emissions from ^{222}Rn. In this study, the large-area iQID was used to determine the collection pattern of these air particulates and quantify if beta/gamma emissions were collected onto the sample. Results suggested an accurate collection of beta and gamma daughter emissions from ^{222}Rn with further details were expressed in Section 5.3 **below**.

5.1. Particle and energy discrimination

5.1.1. Introduction

As a further evaluation of how radiation interacts within a phosphor screen/scintillator and is imaged on the large-area iQID imager, this section will demonstrate if the large-area iQID imager has the capability to distinguish between beta and gamma events based on cluster area and intensity.

For imaging with the large-area iQID, Transcreen LE was isolated as the scintillator option based on its performance characteristics and signal-to-noise ratio previously mentioned in Section 2.2.1 **above**. The purpose of this study is to determine whether particle and energy discrimination is possible through MATLAB post-processing data analysis. If discrimination is possible, which post-processing metric, cluster area, or intensity will be optimal to differentiate gamma events from ^{241}Am and beta events from ^{90}Sr/^{90}Y. Based on a preliminary analysis of the fiber-optic taper, cluster eccentricity was not explored as a discrimination factor in this study. I hypothesize cluster intensity and area would be more appropriate for particle and energy discrimination with the large-area iQID imager.

To support this hypothesis, MCNP modeling of LA-iQID was benchmarked for the absolute efficiencies of beta sources for the Transcreen LE phosphor screen using measured data. MCNP demonstrated scintillation light is optically channeled through the taper to the image intensifier rather than losing light through blurring across the taper. This MCNP modeling data is further shown in the Appendix of this dissertation. With this new MCNP modeling data and characterized information in Chapter 2, I hypothesized beta/gamma discrimination is possible with large-area iQID using post-processing data analysis. To enhance discrimination via post-processing techniques, 2D histogram data cuts were applied based on cluster intensity and area. I hypothesize gamma events from ^{241}Am will have a large cluster intensity across a larger cluster area. Additionally, I hypothesize beta events from ^{90}Sr/^{90}Y (i.e., cluster intensity) will have a more extensive cluster intensity across a smaller cluster area. This hypothesis will be evaluated, and the methodology for the post-processing algorithm will be outlined in the next section.

5.1.2. Methods

In a previous study, several beta and gamma sources were measured on the large-area iQID to determine its ability to distinguish between both types of radiation interactions. Pure beta emitters, ^{99}Tc and ^{90}Sr/^{90}Y (generates bremsstrahlung), were chosen based on the emitted betas particles' energies, which occurs at ~292 keV, 546 keV endpoint for ^{90}Sr and 2.27 MeV endpoint for ^{90}Y, which is in secular equilibrium. ^{241}Am and ^{137}Cs sources were used for gammas, which have emissions at ~60 keV and 662 keV. Likewise, ^{241}Am source emits multiple x-rays which the TranScreen LE is very good at detecting. ^{137}Cs source also emits conversion electrons which if they make it out of the plastic shell. Measurements were conducted using two different phosphor screens/scintillators to 450 μm-thick columnar CsI:Tl sample from RMD and Transcreen LE, to determine which scintillator is optimal beta/gamma discrimination. The results of this study showed discrimination was for a small subset of events likely from the highest energy beta particles. I re-visited the post-processing techniques with new methodology and the existing scintillator option available. Columnar CsI was not available new measurements related to this dissertation. Based on previous characterized results, Transcreen LE was isolated for this study as an optimal scintillator based on its enhanced sensitivity to low-energy beta particles.

To evaluate the particle and energy capability of the large-area iQID, measurements were made again with Transcreen LE, ^{241}Am, and ^{90}Sr/^{90}Y. An image of these sources and the imaging setup is shown in **Figure 68**. Both sources were simultaneously imaged on the large-area iQID, so each source's location would be known in the post-processing script. These locations would assist with a region of interest (ROI) analysis via MATLAB. The proposed post-processing MATLAB algorithm written to discriminate between these sources is outlined below. The steps of the MATLAB algorithm will be tested as follows:

1. Isolate beta/gamma emissions in the large-area iQID imager using ROI analysis of characterized energy response data and applying data cuts based on cluster area and cluster intensity
2. Generate two 1D histograms of cluster intensity and area to determine the distribution for each source
3. Based on the ROI analysis, create one 2D histogram and scatter plot of cluster intensity vs. cluster area for beta and gamma events.
4. The 2D histogram helps select data cuts for the optimal range for cluster intensity and area where each source is most different.
5. Generate a 1D projection by summing along with cluster areas from a 2D histogram created with the data cuts. This new graph can be used to determine the figure of merit for beta/gamma discrimination with the large-area iQID imager.

The figure of merit for the large-area iQID will be calculated as shown in Equation 26 **below** where D is the separation in peaks from beta and gamma events, $\sigma_{betas,}$ and σ_{gammas} full-width-half maximum of betas and gammas, respectively.

$$FOM = \frac{D}{\sigma_{betas} + \sigma_{gammas}} \qquad \textit{Equation 26}$$

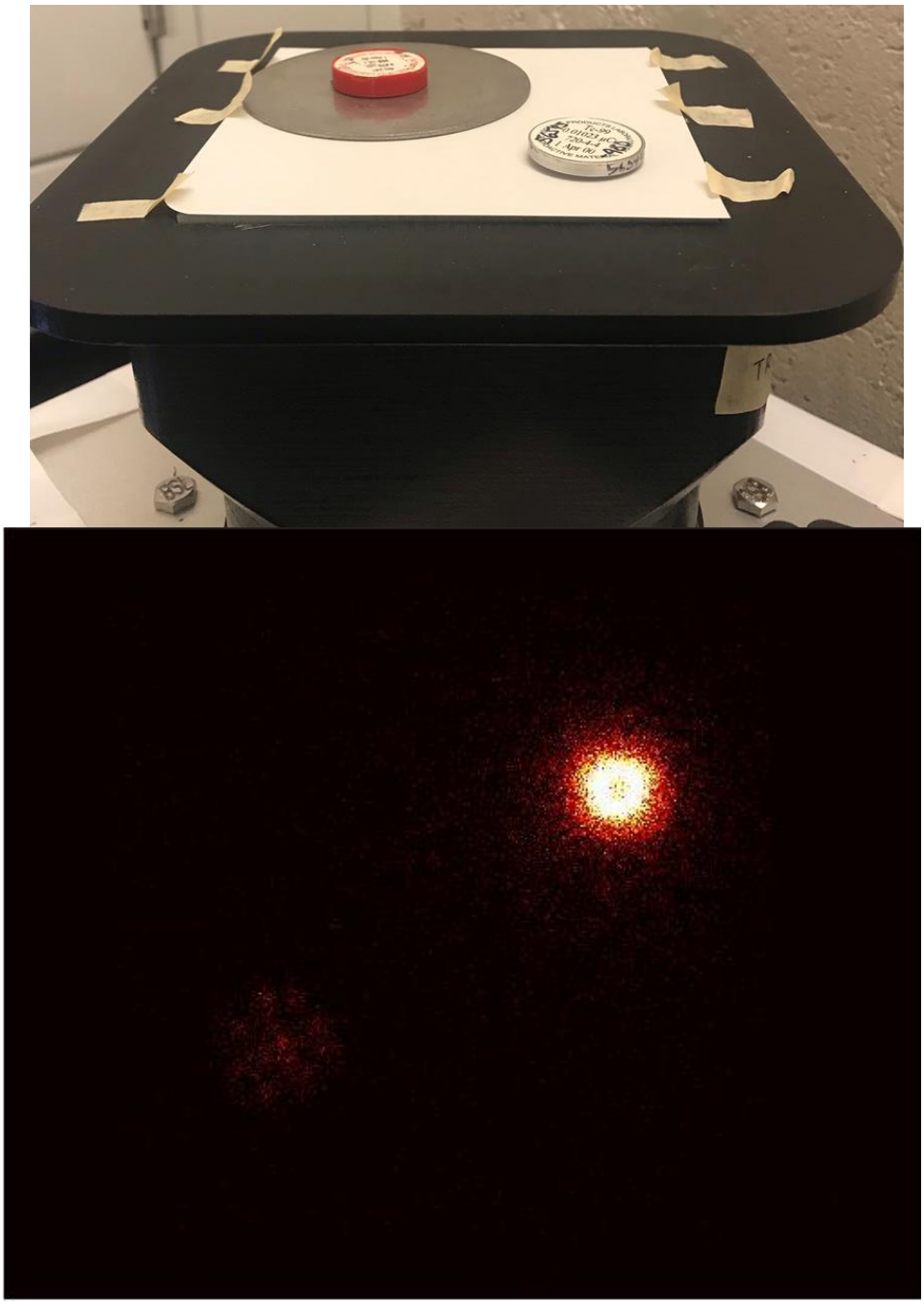

***Figure 68**: (Top) Example setup of beta/gamma discrimination measurements of LA iQID imaging. ^{241}Am (red button source) with tungsten collimator (flat round disk of metal under the red button) and ^{99}Tc (silver one with white sticker). (Bottom) Actual sources used for particle discrimination MATLAB algorithm, ^{241}Am in top right and ^{90}Sr/^{90}Y in bottom left.*

5.1.3. Results

The results from each step of the proposed particle and energy discrimination MATLAB algorithm is presented in this section. Firstly, using ROI analysis, the post-processed images of ^{241}Am and ^{90}Sr sources are shown in **Figure 69**. These source ROIs will be used later in the algorithm. The high spatial resolution of the large-area iQID imager allows for distinctive source differences to be seen. Due to the tungsten collimator in the ^{241}Am source image, you can see highly localized event clusters in the center with lower intensity event clusters scattered around the collimator. Likewise, you can see several localized event clusters detected within the ^{90}Sr/^{90}Y source showing the stippling pattern of how the radioactive material was deposited.

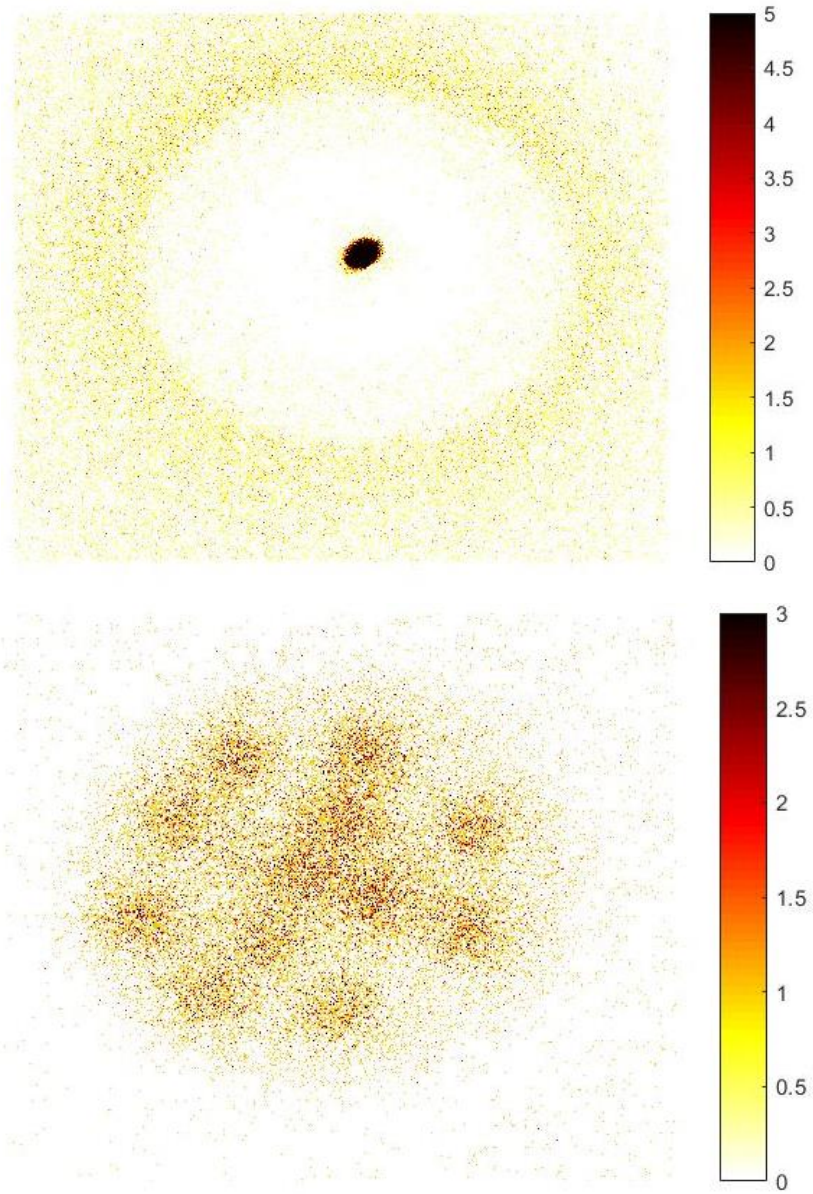

Figure 69: iQID images of both ^{241}Am (top) and ^{90}Sr (bottom) sources used in the MATLAB algorithm.

Next, two 1D histograms were generated for each source in terms of cluster area (**Figure 70**) and cluster intensity (**Figure 71**). In **Figure 70**, the most event clusters of ^{90}Sr/^{90}Y were detected in cluster areas ranging from 0-250 pixels. ^{90}Sr/^{90}Y event clusters seem to peak at approximately 100 pixels and then gradually decreases until reaching 250 pixels.

The event clusters detected from ^{241}Am seem to span a larger cluster area from 0-390 pixels with peaks between 50-60 pixels and 250 pixels. The spike between cluster area 50-60 pixels was likely due to the gamma emission at ~60 keV energy of ^{241}Am. Overall, both sources seem to have a distinctively different distribution for how energy was deposited in the phosphor screen on the large-area iQID imager. This demonstrates that the cluster area was an appropriate option for discriminating beta and gamma events in the large-area iQID imager.

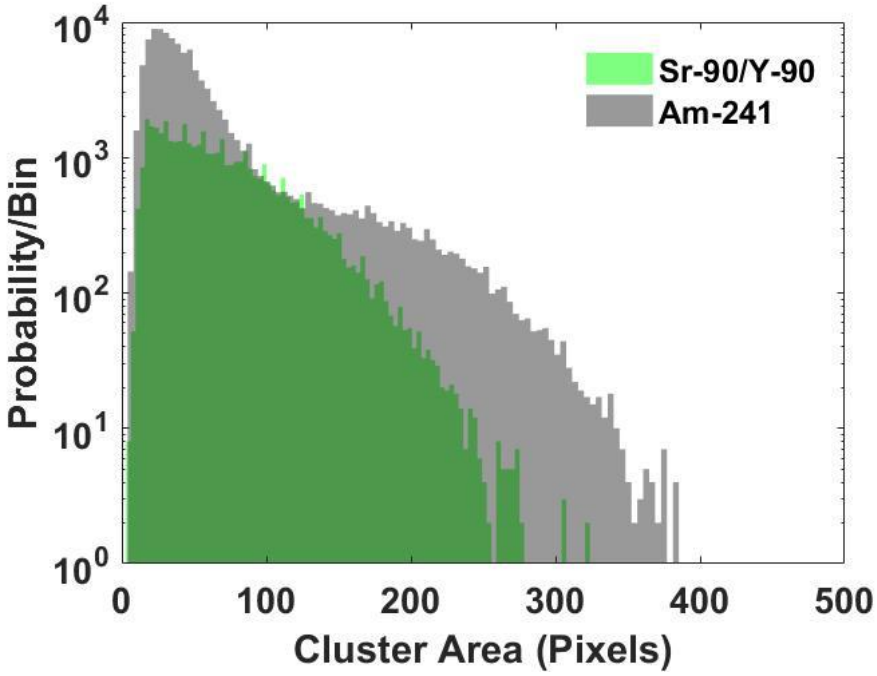

***Figure 70**: 1D Histogram of the cluster area detected by ^{241}Am and ^{90}Sr imaged on the large-area iQID.*

In **Figure 71**, the 1D histogram for cluster intensity is shown. For both sources, the distribution of how much energy is deposited in the scintillator seems very similar. The energy distribution of ^{241}Am has a broad distinct peak with a secondary arc.

The large-area iQID imager could detect gammas like the ~60 keV peak, and the second arc was detecting scattered X-rays. Likewise, the distribution from $^{90}Sr/^{90}Y$ appeared as a broad continuous arc. It was likely due to the constant beta energy spectrum of both isotopes with end point energies ranging from 546 keV to 2.28 keV. An additional observation is the event clusters detected from $^{90}Sr/^{90}Y$ have a slightly lower intensity than the ^{241}Am source. This could be because the activity of the ^{241}Am (506 μCi) was two orders of magnitude higher which induced more spatial pileup than the $^{90}Sr/^{90}Y$ (9.9 μCi) source.

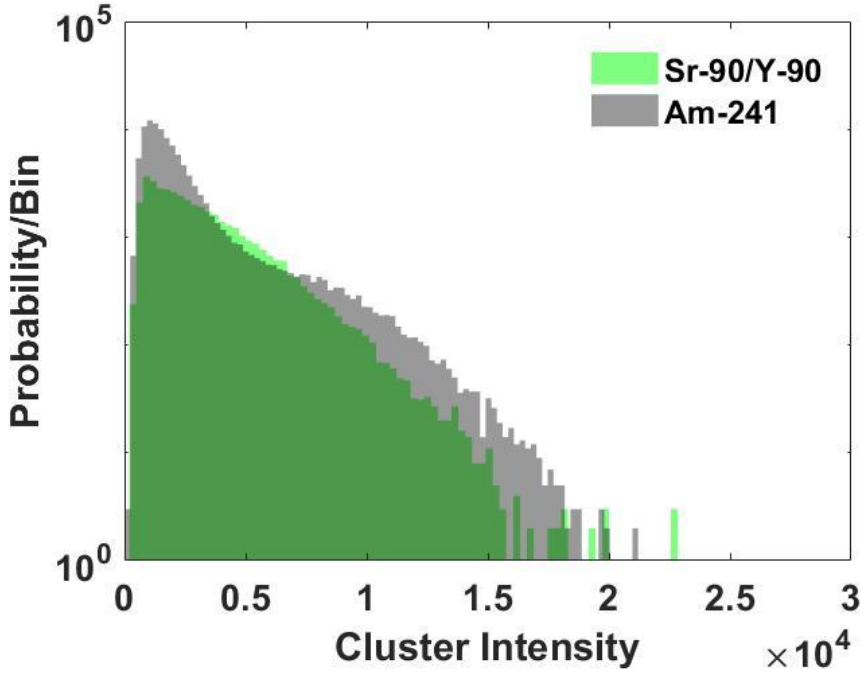

***Figure 71**: 1D Histogram of cluster intensity for $^{90}Sr/^{90}Y$ and ^{241}Am sources imaged via the large-area iQID imager.*

Next, each source's ROI analysis was used to create a 2D histogram of cluster intensity vs. cluster area. This was demonstrated in **Figure 72**. A 2D histogram was successfully created for ^{241}Am and $^{90}Sr/^{90}Y$ sources using the detected event clusters in this figure.

It is shown that the gammas from 241Am deposited most of its energy across a larger area within the scintillator of the large-area iQID. On the contrary, the betas from ^{90}Sr/^{90}Y deposited its energy across a shorter area. In this experiment, the cluster area is the stronger discrimination metric than cluster intensity. This was further explored by creating a new 2D histogram by decreasing the source differences by summing both ^{241}Am and ^{90}Sr/^{90}Y ROIs in the x-direction (i.e., along cluster area). This result was demonstrated in **Figure 73**.

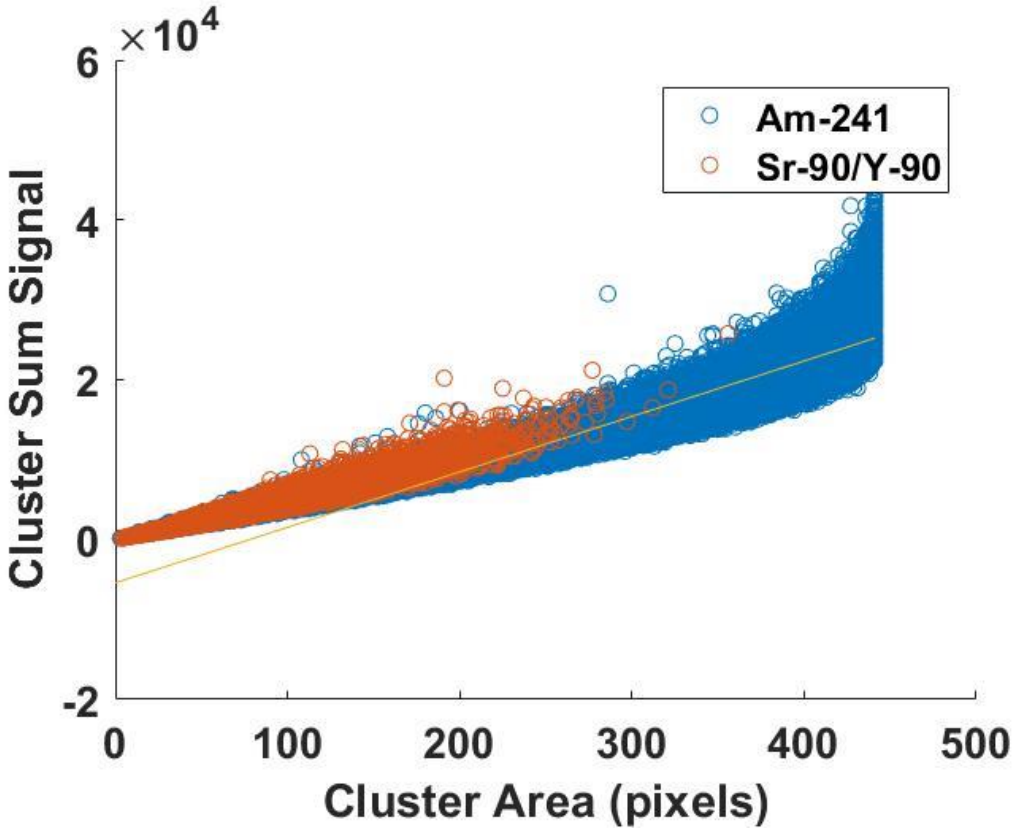

***Figure 72**: 2D Histogram of cluster intensity and cluster area of both 241Am and 90Sr sources. The discriminator line is used to determine the following figure-of-merit (FOM) graph.*

In **Figure 73**, the figure-of-merit graph was demonstrated for ^{241}Am and ^{90}Sr/^{90}Y.The differences in terms of cluster area are diminished because the values were summed along to highlight each source's cluster intensity differences. The red box in **Figure 73** shows the prominent event cluster peaks used to calculate the FOM for particle discrimination. Considering that the large-area iQID imager was not a typical detector used for particle discrimination, a set metric or equation was not created. One possibility was looking at the differences in the peaks from each source. The peak of ^{241}Am was located at a cluster intensity of ~ 550, whereas the peak of ^{90}Sr/^{90}Y is located at ~ 2400. The difference between the two can demonstrate how well the large-area iQID imager can detect differences between gammas and betas. Further work could be done to deconvolute this graph and obtain a FOM value.

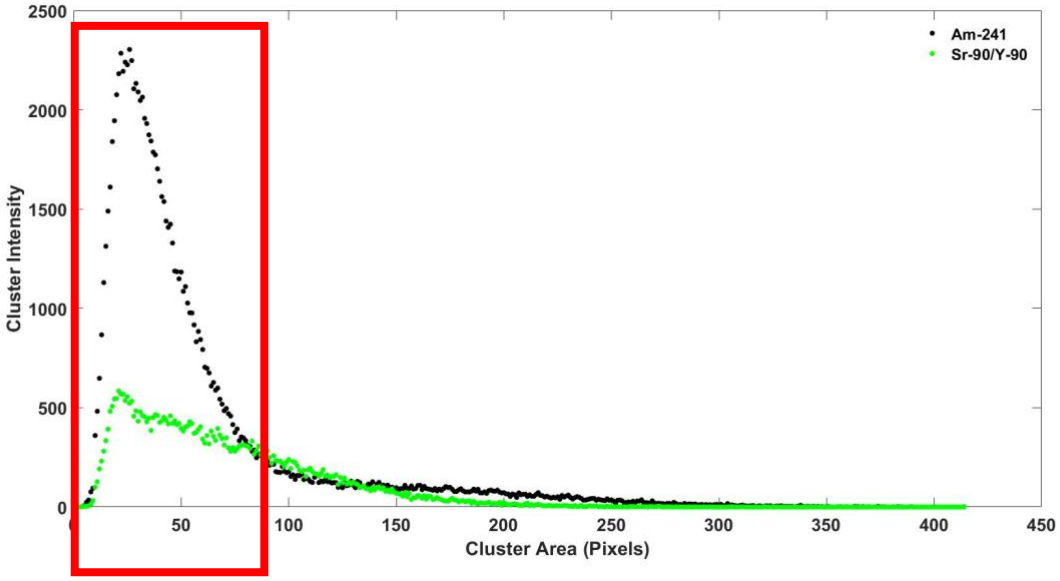

***Figure 73**: Figure of merit (FOM) 2D histogram graph for 241Am and 90Sr/90Y.*

5.1.4. Discussion

An evaluation of the large-area iQID imager was done to determine whether this type of imager could discriminate between different kinds of radiation. To test this potential capability, post-processing MATLAB metrics were used to analyze the large-area iQID imager's image data. Cluster area and intensity were the two chosen post-processing metrics. For this experiment, two different sources, ^{241}Am and ^{90}Sr/^{90}Y, were tested to discriminate event clusters from gamma and beta radiation. It was determined that cluster area and intensity were accurate metrics to distinguish gamma and beta events emitted from each source. Cluster area was the stronger metric to discriminate the gammas from ^{241}Am and betas from ^{90}Sr/^{90}Y. In this case, the energy detected from the ^{241}Am gammas were more dispersed across more pixels than the betas from ^{90}Sr/^{90}Y. It is possible the collimator used during imaging with ^{241}Am allowed the events to be localized but also scattered the gammas and X-rays across the phosphor screen. This specific set of sources and setup does should that particle discrimination is possible for only some events, but more work is necessary to determine whether LAiQID can fully discriminate radiation interactions. One disadvantage of this study was the lack of time and funding to determine an appropriate metric/ equation to obtain a FOM for the LAiQID imager. Therefore, the study is incomplete. Future work would require more research related to energy dependence, collimation, source spatial extent and what fraction of events can be successfully discriminated from the other isotope. Cluster area and intensity features may just be dependent on energy deposition rather than the particle type that is depositing the energy. In the future, this could be tested with electrons and gammas at the same energy.

5.2. Image Co-registration

5.2.1. Introduction

Image registration is the process of transforming different sets of data into one coordinate system. Once images are converted into one coordinate system, images are defined as co-registered. Several applications find image co-registration as a useful technique to compare or integrate data from different measurements. Some applications are computer vision, medical imaging, satellite imagery, remote sensing, and target recognition. In **Figure 74**, examples of image registration in computer vision, medical imaging, and satellite imagery are expressed.

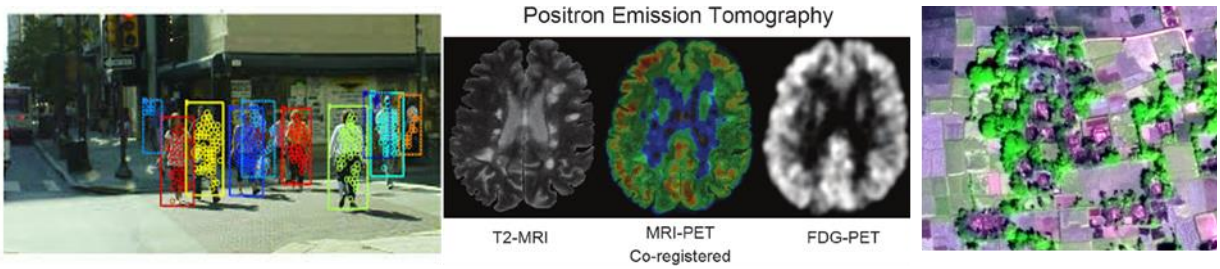

***Figure 74**: (Left to right) Examples of co-registered images in computer vision [64], medical imaging [65], and satellite imagery [66] .*

The process of image co-registration improves the overall signal-to-noise ratio of both images. This occurs by enhancing the individual properties of each image and then overlaying together. For example, in the satellite imagery photo above, one image would contain information on the geological landscape information (i.e., trees, rivers, etc.). The other image would have information related to the architecture landscape (i.e., buildings, houses, etc.). Through image co-registration, one would extract information from one signal/image, such as where the trees are compared to the buildings.

Overall, the approach to image registration is situation-dependent and requires a carefully selected point transformation model as the reference point between images.

There are four main algorithm classifications for image registration, which define different ways to align images. These were intensity-based, feature-based, spatial domain methods, or frequency-domain methods. Both photos will either be depicted as a reference image or moving image despite the classification type. The reference image is the static image, and the moving image undergoes a spatial transformation to match the reference image. Intensity-based image classification is an iterative process that aligns images based on their relative intensity patterns via correlation metrics. These correlation metrics consists of the pair of images, the similarity metric, an optimizer, and a transformation type. In this context, the similarity metric evaluates the registration accuracy by how similar the images are without a transformation. Based on the similarity metric result, the optimizer will either minimize or maximize the similarity metric. The transformation type defines the type of 2D geometric transformation necessary to align the misaligned moving image with the reference image. This process is repeated until both images are best aligned together. An example of the process flow of intensity-based automatic image registration is shown in **Figure 75**. The registered image was the entire image with the center of the image and different intensities/labels as a feature point.

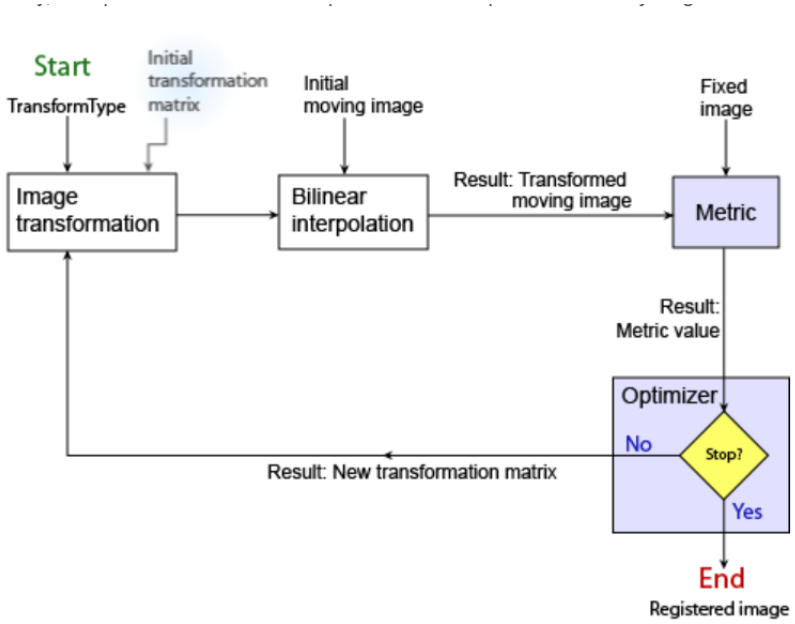

***Figure 75**: Process flow chart of intensity-based automatic image registration classification [67].*

The second type of image classification is an algorithm called feature-based classification. This type of registration is based on image features such as points, lines, or contours. These features are isolated in both images and become the number of corresponding distinct points in images. Between these specific image points, a point-by-point correspondence is calculated. A geometric transformation is performed to map the moving image to the reference image. This technique of feature-based automatic image classification is widely used in computer vision and satellite imagery applications. An example of a feature-based automated image co-registration is expressed in **Figure 76**.

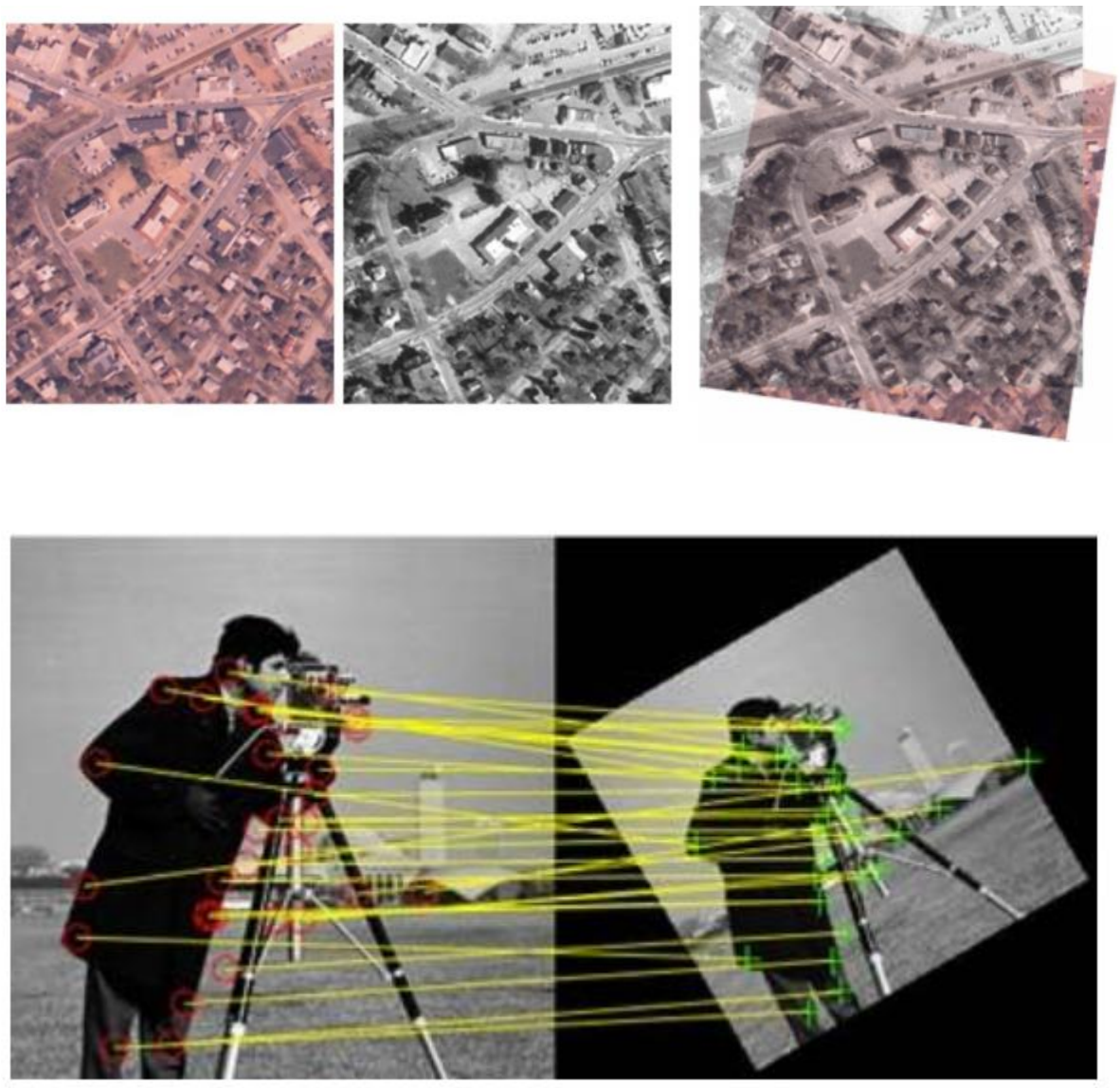

***Figure 76**: Examples of feature-based image classification. (Top): Point mapping of aerial photos. (Bottom): Line mapping of the same photo but images of different orientations [66].*

The third and fourth type of image classification algorithm is based on the kind of image domain. Image enhancements occur either in spatial or frequency domains. The spatial domain represents the image plane itself, whereas the frequency domain deals with pixel change rate.

Any image enhancements in the spatial domain operate on the direct manipulation of image pixels. Likewise, image modifications in the spatial domain are computational less demanding when compared to the frequency domain.

This section of the dissertation will present how image co-registration was applied to imaging with the large-area iQID. The objective was to develop an automated image co-registration scheme in MATLAB to co-register a photograph and an autoradiograph collected from a sample measured with an iQID. An example of an autoradiograph and photo of fiducial uranium glass shapes are expressed in **Figure 77**. These shapes were used as fiducial markers for the MATLAB program. The darker colored glass shapes had higher levels of uranium in the glass than the lighter colored pieces. Uranium and progeny isotopes emit radiation that can be detected by the iQID in beta/gamma or alpha mode.

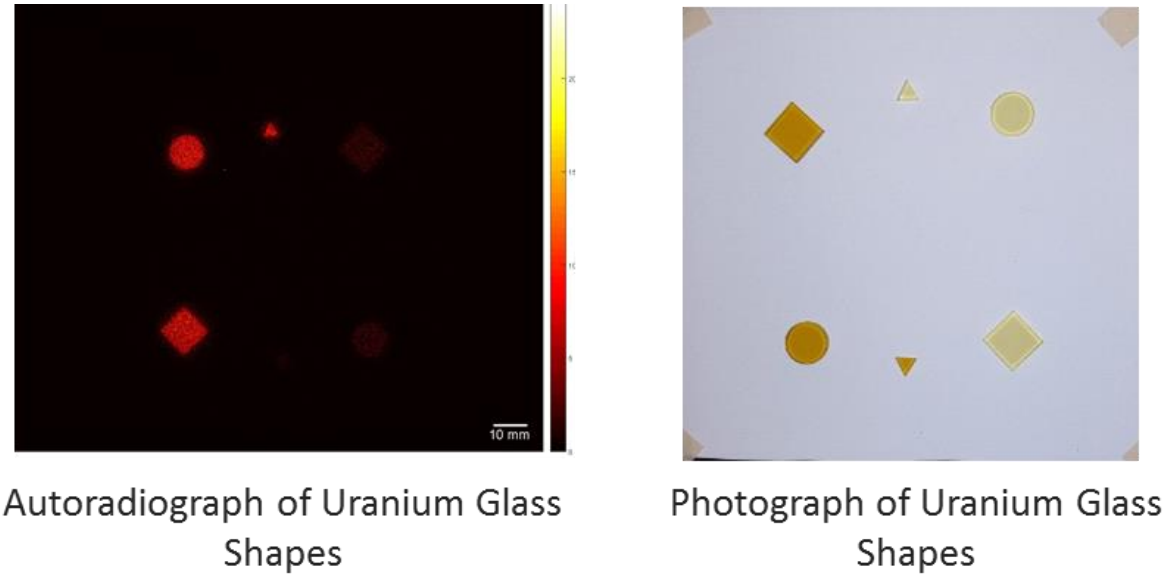

***Figure 77**: Examples of images to be co-registered (left) autoradiograph from large-area iQID and (right) a photograph of uranium glass shapes*

Some differences between both images in **Figure 77** are the background color, the orientation of shapes, pixel size and scale, and the need to depict radioactivity colormap in the autoradiograph. These differences will be highlighted in the MATLAB scheme to properly co-register both images. Image modifications of the autoradiograph and photograph will take place directly in the image domain. Therefore, spatial domain algorithm methods for image co-registration will be explored instead of the frequency domain. Considering image co-registration with large-area iQID is a new application, achieving a MATLAB scheme was unknown. It was also unknown which image classification method, intensity-based or feature-based, would create the best transformation model between both images. Therefore, an assumption was made regarding the images in **Figure 77**. There are no apparent image features expect the fiducial markers (i.e., points, lines, or contours), so feature-based image classification will not be used. Therefore, the intensity-based image classification will be explored to co-register the autoradiograph and photograph.

5.2.2. Methods

The developed MATLAB image co-registration scheme is expressed as a process flow chart for simplicity in **Figure 78**.

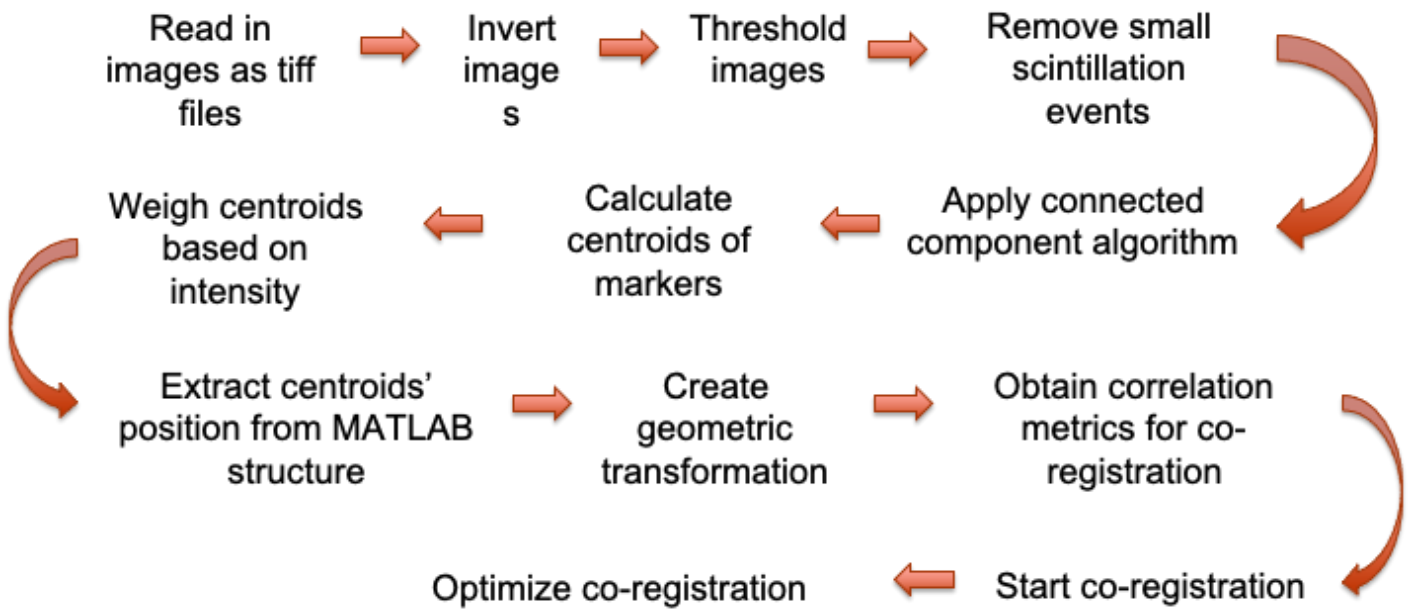

***Figure 78**: Process flow chart of the image co-registration scheme for the large-area iQID.*

5.2.3. Results

The co-registered image of the autoradiograph and photograph of uranium glass shapes is shown in **Figure 79**. In **Figure 79**, the automated image co-registration scheme was successful on the left of the image because the co-registered image demonstrates characteristics from both images. All uranium glass shapes and their corresponding details from the photograph can be seen in the co-registered image. Likewise, the co-registered image demonstrates higher radioactivity (red) from 3 out of 6 uranium shapes and lower radioactivity in the other 3 shapes. Lower radioactivity is expressed as yellow and superimposed onto right-most shapes.

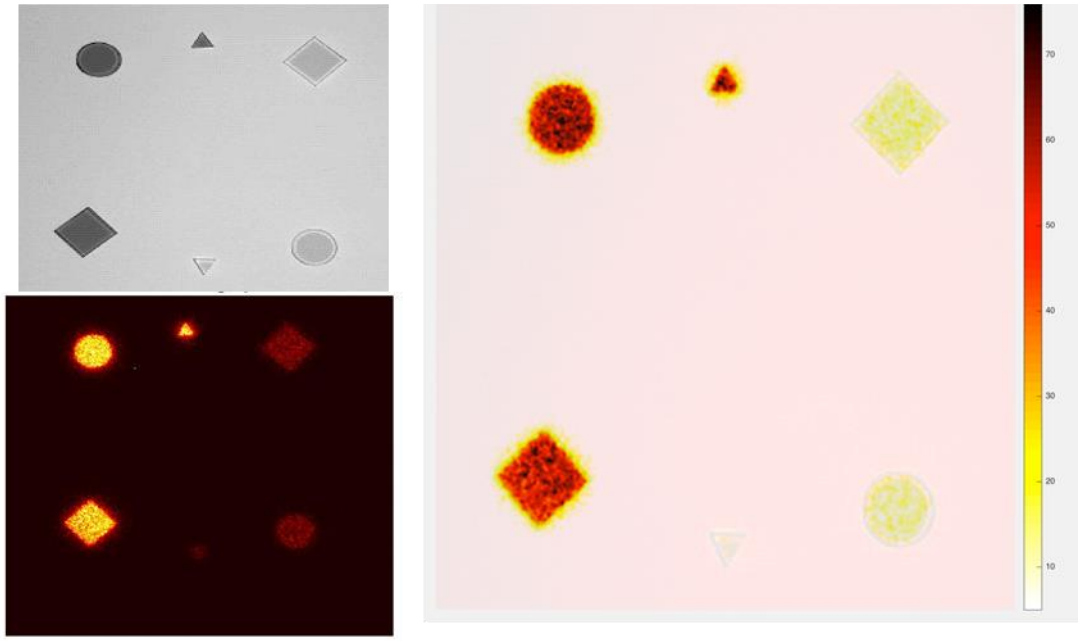

***Figure 79**: Results of image co-registration with e large-area iQID. (Top left) Photograph image. (Bottom left) Autoradiograph image. (Right) Co-registered image of both autoradiograph and photograph.*

5.2.4. Discussion

An automated co-registration scheme for the large-area iQID was successfully developed using MATLAB. Until this dissertation, the technique of image co-registration was not applied to the large-area iQID. Therefore, a unique approach was conducted to determine which classification method of image registration should be used. Based on the complexities that arose during the process, both image classification algorithms of intensity-based and spatial/image domain methods were used. Intensity-based and spatial/image domain methods were chosen instead of feature-based and frequency-domain methods, respectively.

Three main complexities influenced the decision to take this approach. First, the scale and background differences between images delayed registration optimization as images could not be directly superimposed. Optimization was found to work if the photograph's scale was reduced to match the scale of the autoradiograph. The orientation of the picture was also flipped to match the autoradiograph. Additionally, optimization was improved if the background differences were corrected by inverting both images before registration/transformation. The second complexity was the decision-making of determining which photo would be the reference and moving image. This is very important for geometric change necessary to conduct image co-registration successfully. The reference image is stationary, while the moving image is spatially transformed to match the reference image. The geometric transformation was successful if the photograph was selected as the reference image, and the autoradiograph was the moving image. The third complexity was the removal of human involvement to streamline the scheme's automation. There is a built-in function for image classification in MATLAB using spatial methods called the Control Point Registration. However, this built-in function requires human involvement to choose the control points for co-registration in images.

It was found that the manual involvement of the Control Point Registration could be removed if control points were selected based on intensity. The weighted centroids of event intensities were calculated for the uranium markers in both the autoradiograph and photograph. The geometric transformation was much improved by using these intensity-based and spatial methods for the image co-registration scheme. This further enhanced the co-registration's optimization, leading to a successful co-registered image of the autoradiograph and photograph.

In conclusion, the image co-registration of the large-area iQID did not work with only one type of algorithm classification method. The successful scheme was achieved by isolating differences in both the autoradiography and photograph. This led to the decision to use both intensity-based and spatial domain methods in the classification algorithm.

5.3. Electrostatic Air Precipitator Film Imaging with iQID

5.3.1. Introduction

Ambient air particles were electrostatically collected onto a conductive tape sample and imaged on the iQID imager. For this imaging test, interested ambient air particles included decay products from ^{222}Rn. ^{222}Rn is in the uranium series and the immediate alpha-decay product of radium-226 (^{226}Ra). The half-life of ^{226}Ra and ^{222}Rn is 1.62 x10^3 years and 3.82 days, respectively. The alpha decay of ^{222}Rn from ^{226}Ra results in three crucial decay products. These decay products consist of polonium-218 (^{218}Po) via alpha and beta decay, lead-214 (^{214}Pb) via beta decay, and bismuth-214 (^{214}Bi) via beta decay. These decay products have a short half-life time, which will be vital for iQID imaging of the electrostatic tape sample. This will be achieved by using the short half-lives of these beta decay products. The half-life of ^{214}Pb and ^{214}Bi is 26.8 minutes and 19.7 minutes, respectively. For completeness, the half-life of ^{218}Po is 3.05 minutes [68].

The objectives of this imaging study were divided into two parts. The first objective was proof of concept to determine if the conductive tape sample can be imaged on the iQID. If iQID imaging was successful, then the electrostatically deposited air particles' pattern could be studied further. This became the second task of the first experiment. The trajectory of the different air particles and location on the tape sample is based on the electric field and the various air particles' mass. Therefore, through iQID imaging, the pattern and trajectory of these air particles could be determined. This study's second objective was to determine if the iQID imager can quantitatively detect the beta decay products of ^{222}Rn.

5.3.2. Methods

iQID imaging of the electrostatic tape sample was conducted with two different iQID imagers. The imaging area is the significant difference between iQID imagers: the large-area iQID system and a smaller iQID system (ø 40mm imaging area). This difference is due to the lack of a fiber optic taper, hence reduced imaging area. All measurements with these iQID systems were imaged in beta mode using the TranScreen LE phosphor screen. The tape sample consisted of a blue painter's tape. Using an iQID imaging method called time slicing, the number of detected air particles within 5-minute intervals will be collected. Based on the decay rates and initial abundances, the detected abundances and activities within a decay chain can be calculated as a function of time. In nuclear physics, this mathematical model is called the Bateman equation. Equation 27 **below** demonstrates changes in isotope *(i)* amounts within the decay chain as a function of time (*t*) when there are N_i (*t*) isotope atoms that decays into isotope (i+1) at a rate of λ_i.

$$\frac{dN_1(t)}{dt} = -\lambda_1 N_1(t)$$

$$\frac{dN_i(t)}{dt} = -\lambda_i N_i(t) + \lambda_{i-1} N_{i-1}(t) \qquad \textit{Equation 27}$$

$$\frac{dN_k(t)}{dt} = \lambda_{k-1} N_{k-1}(t)$$

Coupling time-slicing iQID imaging technique with the Bateman equation, the detected activities for decay products ^{218}Po, ^{214}Bi, and ^{214}Pb will be calculated. These two methods will determine the usefulness of iQID imaging with an electrostatic tape sample.

5.3.3. Results

An image of the tape sample with electrostatically deposited ^{222}Rn air particles can be observed in **Figure 80**. This tape sample is expressed on top of the input window of the large-area iQID.

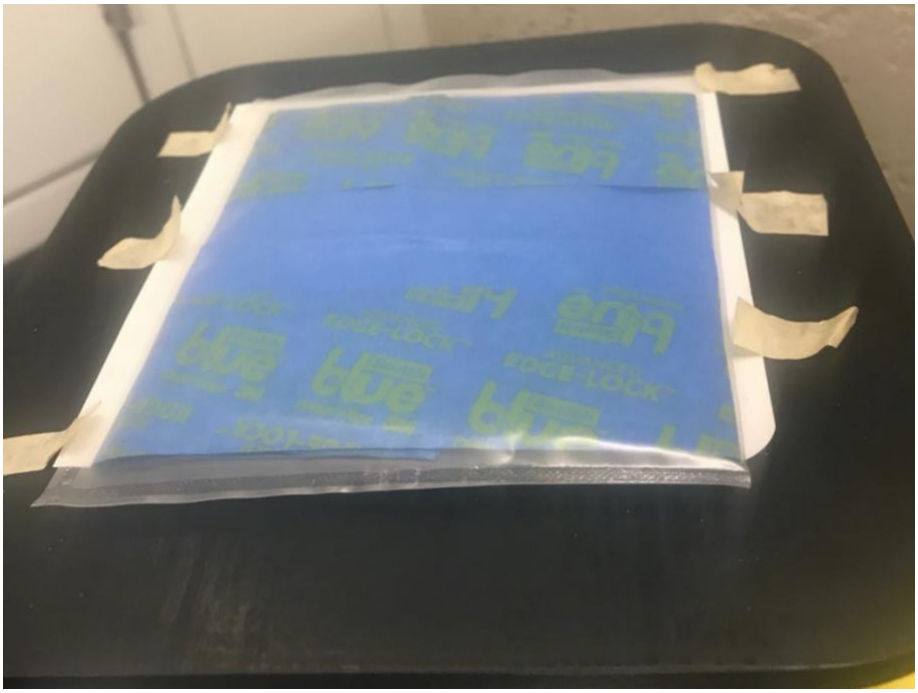

***Figure 80**: Image of the blue painter's tape electrostatic tape sample on the large-area iQID*

Next, the time slicing iQID imaging technique and Bateman equation was applied to analyze the electrostatic tape sample. In **Figure 81**, a plot of the count-rate vs. elapsed time with a corresponding three-component Bateman fit was calculated based on the decay products of ^{218}Po, ^{214}Bi, and ^{214}Pb. In **Figure 81**, a high drop in count-rates over the first 5 minutes was detected that matched the decay rate of ^{218}Po.

In **Table 13**, the signature, detected activity on the large-area iQID, and associated uncertainty were calculated.

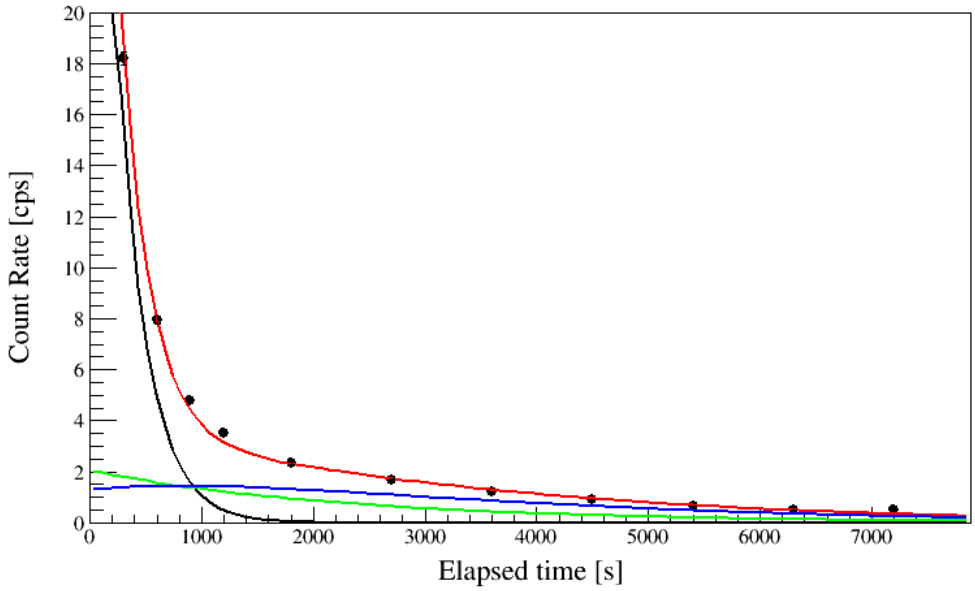

Figure 81: *Decay curves of count rate vs. elapsed time obtained from the electrostatic precipitator tape sample on large-area iQID. Beta/gamma decay products measured for 2 hours with TranScreen LE. ^{218}Po (red curve) , black curve is the fit used to calculate uncertainty, ^{214}Bi (green line), and ^{214}Pb (blue line).*

Table 13*. Imaging Results of Electrostatic Air Sample on the Large-area iQID*

Signature	Detected Activity	Uncertainty [%]
^{214}Pb	2.06	0.03
^{214}Bi	1.28	0.14
^{218}Po	47.99	0.81

5.3.4. Discussion

In **Figure 81**, count-rates exponentially decreased at a decay rate of ^{218}Po during the first 5- minutes with an uncertainty of 0.81 %. This is an unexpected finding because iQID was placed in beta imaging mode, and the emission of ^{218}Po is primarily via alpha decay. This finding was compared to the event-rate/count-rate instability observed and discussed in Chapter 4. Therefore, the high drop in count-rate was determined not to be related to the emission of ^{218}Po but rather to count-rate instability within the first 5-minutes of acquisition. This finding may be caused by electronic noise within the iQID components when the power supply is turned. This observation is supported because count-rates seem more stable as the elapsed time increases after 5-minutes. Therefore, the system's count-rate instability decreases the longer the acquisition time. This instability is essential to be aware of when doing short-lived half-life measurements with the large-area iQID. During long half-life measurements, count-rate instability is not a factor. This informs the LAiQID should be on for several minutes before acquiring data to stabilize.

Chapter 6

Conclusions

The purpose of this dissertation was to determine whether the large-area iQID imager could be adapted into the safeguards field. For detectors to be considered essential towards safeguards applications, sensors should be capable of specific performance characteristics. In environmental sampling, swipe samples are analyzed, using HRGS detector and XRF imager, to determine whether radioactivity is present on these samples. Alpha and beta/gamma radioactive emissions are of interest in terms of this dissertation. If detectors could pre-screen where radioactive particles are located on the sample, then high-activity particles on swipe samples could be more efficiently measured in further analysis such as HRGS, XRF, and mass spectrometry. In terms of mass spectrometry, having a smaller piece of the swipe sample allows a reduction in background from the natural radioactivity in the fabric. It is essential for the IAEA to measure radioactive material of swipe samples and verify declared nuclear material is consistent with declarations. For iQID to be relevant for safeguards, the following criteria were deemed important: high spatial resolution, sensitivity to a wide range of radioactive activities 0.001 Bq to 10^7 Bq, larger imaging area (10 cm x 10 cm), and high count-rate capability. An iQID for safeguards should be able to quantitatively image high activity samples due to the activities potentially detected on swipe samples. For the large-area iQID to be adapted for safeguards applications, first, the baseline performance of the large-area iQID was characterized.

Two detector configurations of the iQID imager were evaluated: addition of a fiber-optic taper (i.e., larger imaging area) and gating feature on the image intensifier (i.e., increases count-rate capability). Performance metrics evaluated were spatial resolution, energy response for alphas and betas/gammas, MDA, detector uniformity, and count-rate capability.

The intrinsic alpha and beta/gamma spatial resolution for the large-area iQID imager was 95 μm and 142 μm, respectively. Based on the CMOS pixel size magnification, the effective pixel size of large-area iQID is 60μm. With an alpha spatial resolution of 95 μm, this means an alpha event cluster spreads laterally approximately 1.5 times the effective pixel size of the large-area iQID.

On the other hand, beta/gamma event clusters are detected at 2.3 times the effective pixel size of the large-area iQID. This alpha, beta, and gamma event clusters can be observed in **Figure 18**. The lateral spread of these alpha and beta/gamma event clusters broadens the photopeak of energy response signals (**Figure 19**), which makes accurately identifying and discriminating radioactive signatures difficult. Large-area-iQID imager can differentiate between alpha and beta/gamma events but not betas from gammas events. Future research is needed to investigate beta/gamma discrimination further to determine its adapting into the safeguards field would not be ideal. The lateral spread or blurring of the alpha and beta/gamma event clusters could be due to their light spreading within the fiber-optic taper. Despite this, alphas and beta/gammas' energy responses have distinctly different energy distributions (**Figure 19**). In **Figure 19**, beta and gamma have similar energy response distributions, further supporting that discriminating between beta/gamma responses may be challenging for the large-area iQID imager.

Post-processing data-cuts based on event size, shape, and intensity could help discriminate between beta/gamma event clusters (Chapter 5.1 **above**). If post-processing MATLAB data cuts could not differentiate between beta/gamma event clusters, it would remove some utility of iQID for imaging swipe samples. In Chapter 5.1 **above,** an evaluation of the large-area iQID imager was done to determine whether this type of imager could discriminate between different kinds of radiation. Cluster area and intensity were the two chosen post-processing metrics.

For this experiment, two other sources, ^{241}Am and ^{90}Sr/^{90}Y, were tested to discriminate event clusters detected from gamma and beta radiation. It was determined that the cluster area and intensity were useful metrics to attempt differentiate gamma and beta events emitted from each source. Cluster area was the better metric to discriminate the gammas from ^{241}Am and betas from ^{90}Sr/^{90}Y. Cluster shape was determined to be the least useful metric to differentiate beta/gamma events because different event shapes disappear due to the lateral spread during event interactions with the fiber-optic taper. Energy detected from the ^{241}Am gammas were more dispersed across more pixels than the betas from ^{90}Sr/^{90}Y (**Figure 72**). It is possible the collimator used during imaging with ^{241}Am allowed the events to be localized but also scattered the gammas and X-rays across the scintillator. One disadvantage of this study was more time was required to determine an appropriate metric/ equation to obtain a FOM for the large-area iQID imager. In the future, provided more time and funding, a new FOM graph should be attempted by summing along with cluster intensity (y-axis). This would genuinely answer the question of whether the large-area iQID imager has the capability to discriminate between beta/gamma event clusters.

A surprising discovery related to detector uniformity was made while characterizing the large-area iQID imager's baseline performance. The large-area iQID detector has an overall efficiency that drops by a factor of 2 when measurements are conducted in the center and edge (**Figure 20**). This demonstrates the presence of nonuniformity from the fiber-optic taper. Despite this nonuniformity, the large-area iQID imager can have an intrinsic efficiency for alphas, and high-energy betas are nearly 100%. Future studies could correct this nonuniformity based on conducting a flat field correction or spatially-varying event detection threshold. However, for this dissertation, the nonuniformity was not seen as a performance issue.

The large-area iQID was characterized to detect a range of particles and energies, from >50 keV electrons and gammas to 6 MeV alpha particles. The minimum detectable activity (MDA) for the large-area iQID ranges from 0.01-0.1 Bq/cm^2 for β emitters and 4 mBq/cm^2 for α-emitters. Detecting alphas and beta/gamma emitters at these lower limits are vital for safeguards applications due to the pre-screening benefit. Detecting high activity limits are also essential for imaging swipe samples. Therefore, the count-rate capability of the large-area iQID was investigated. The performance effects of adding a gating capability to the image intensifier of the large-area iQID for imaging higher activity samples were also characterized and evaluated.

Count-rate capability is an important performance metric to investigate whether the large-area iQID imager can be adapted into the safeguards field. Two different types of large-area iQID configurations were evaluated: without and without gating on the image intensifier. Without gating, the large-area iQID imager (10 cm x 10 cm) has a more significant count-rate capability (lower spatial pileup) when compared to a previous small-area iQID system (4 cm x 4 cm) without a fiber-optic taper. Characterization measurements were required before quantitative imaging measurements could be done using the gated image intensifier. Characterization of the gated large-area iQID imager was tested at both normal and inverted wave polarity to determine which setup detected the highest count-rates (**Figure 50**). Based on the vendor recommendation, it was hypothesized that the inverted wave polarity would produce the highest count-rates. This hypothesis was deemed supported as the highest absolute efficiency (**Figure 50**) and count-rates were calculated at an inverted polarity (**Figure 48**) using a ^{99}Tc source. Therefore, gated measurements using the large-area iQID would be evaluated at an inverted polarity.

Next, quantitative imaging with the large-area iQID imager was evaluated using a ^{241}Am source (506 μCi) and a gated image intensifier.

The purpose was to induce spatial pileup on the scintillator and determine if the CMOS sensor could estimate the true detection rate from a time-sampling of the data accomplished through gating, where the sampled data did not have as much spatial pileup. If this could be achieved, then the gated large-area iQID could be adapted to image swipe samples across a greater range of expected activities. Secondly, low energy gammas were detected at lower activity range while using a ^{241}Am source. The incident flux of the 506 μCi ^{241}Am source was quantitatively imaged with the large-area iQID at a duty cycle of 1% (**Figure 64**). Duty cycles lower than 1% such as 0.1% (**Figure 65**) and 0.01% (**Figure 66**) removed/missed necessary event clusters emitted from the 506 μCi ^{241}Am source. As a result, the gated large-area iQID a higher capability to quantitative image low-medium energy betas than low energy gammas. However, in the future, if the duty cycle was lowered to 1% when imaging the ^{241}Am source again, then the detectable counts and activity range may have been higher. In other words, adding the gated capability to the image intensifier of the large-area iQID improved the detector's count-rate capability by imaging a higher activity range. Hence, the gated large-area iQID imager could quantitatively image swipe high activity samples.

Lastly, to assist adaptation of the large-area iQID imager into the safeguards field, this dissertation aimed at achieving two additional tasks. In addition to having the ability to quantitatively image relatively high activity samples (506 μCi), the large-area iQID demonstrated it could be application to additional imaging studies outside the main scope of this dissertation. It was determined that 1) sample autoradiographs and photographs could be co-registered with good fidelity, and 2) the large-area iQID could be used to image beta/gamma progeny deposited on a sample from an electrostatic air precipitator.

This dissertation demonstrated how the large-area iQID imager could have beneficial performance metrics useful to the safeguards field such as high spatial resolution and count-rate capability (gated configuration), modest energy resolution with potential for particle discrimination with post-processing techniques, and portable lightweight size. The large-area iQID imager could be adapted as a pre-screening technique useful in imaging swipe samples in the field. The gated large-area iQID could be adapted as an imaging technique for environmental swipe sampling for a large range of sample activities.

Future work should investigate discrimination capabilities between gamma and beta events due to its usefulness in safeguard applications to detect trace amounts of nuclear material and prevent nuclear material proliferation. It would also be worth investigating whether the optimal duty cycle for quantitative imaging changes based on its radiation interaction (alpha, beta, photon).

Appendix

A. Previous MCNP Modeling Study with Large-area iQID

A MCNP6.1.1b model of the large-area iQID system was developed to understand and calculate the theoretical absolute efficiencies for different beta and gamma sources of interest. This work was performed by Edward Siciliano and Ben McDonald [10] [11]. Overall, MCNP agreed with the measured theoretical intrinsic and absolute efficiencies for several beta sources. This indicated that incident beta particles were successfully being detected on the phosphor screens. This was validated with measured data presented throughout Chapter 3 **above**. In terms of gammas, the MCNP6 simulations did not benchmark ^{241}Am accurately and needs to be re-investigated. This MCNP information was essential in determining performance characteristics of the large-area iQID. For example, this MCNP data was vital as to whether the large-area iQID could theoretically distinguish between beta and gamma events in Chapter 5 **above.** The MCNP model was used to assess detection efficiencies and confirm data wasn't lost during the signal generation process of the LAiQID. The MCNP model confirmed experimental measurements. Lastly, the large-area iQID was expected to have low energy response yet reasonable count-rate capability while reaching signal saturation level (high spatial pileup) as count-rate increases [10].

B. Particle and Energy Discrimination on Smaller iQID system

Figure 82 demonstrates how a different, yet smaller (40 mm or 4 cm) iQID system distinguishes between different radiation. A smaller pixel size aids in separating different radiation interactions from one another. In this figure, elognated event clusters were detected. Cluster shape was the post-processing MATLAB metric used to demonstrate the beta elongated tracks in this smaller iQID system configuration. It was hypothesized these elongated shapes were beta tracks losing energy in the phosphor screen as only a small fraction of the total events had these shapes. It was not confirmed if these event shapes were beta tracks but this finding drove further investigation of particle discrimination with LAiQID.

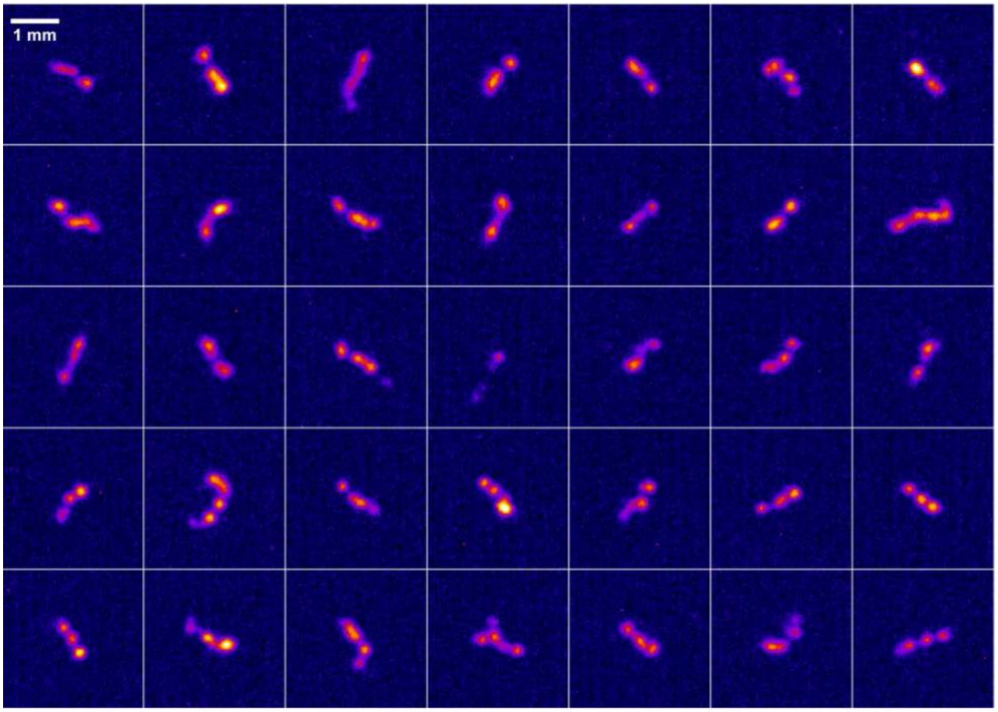

Figure 82: Individual event clusters from a $^{90}Sr/^{90}Y$ source and a Blue 100 phosphor screen (MCI Optonix, LLC.). Some of the event clusters had distinctive tracks, which might be used to discriminate beta and gamma interactions.

Bibliography

[1] IAEA, "Basics of IAEA Safeguards," IAEA, 1998. [Online]. Available: https://www.iaea.org/topics/basics-of-iaea-safeguards. [Accessed 10 June 2019].

[2] B. Jones, Next Generation Safeguards Initiative Nonproliferation and International Safeguards Summer Course, Richland, WA: Pacific Northwest National Laboratory-PNNL-SA-110958, 2016.

[3] IAEA, "IAEA Safeguards Techniques and Equipment: 2011 Edition, International Nuclear Verification Series No. 1 (Rev.2)," IAEA, Vienna, Austria, 2011.

[4] IAEA, "Swipe Check: Collecting and Analysing Environmental Samples for Nuclear Verification," IAEA, 19 January 2016. [Online]. Available: https://www.iaea.org/newscenter/news/swipe-check-collecting-and-analysing-environmental-samples-nuclear-verification. [Accessed 15 January 2020].

[5] B. S. McDonald, M. A. Zalavadia, B. W. Miller, M. Bliss, K. Olsen and D. Kasparek, "Quantitative Digital Autoradiography for Environmental Swipe Sample Prioritization: System Design, Characterization, and Initial Measurements," *Proceedings of the Institute of Nuclear Materials Managements Annual Meeting*, no. PNNL-SA-126590, 2016.

[6] B. W. Miller, S. J. Gregory, E. S. Fuller, H. H. Barrett, H. B. Barber and L. R. Furenlid, "The iQID camera: An ionizing-radiation quantum imaging detector," *Nuclear Instruments and Methods in Physics Research Section A: Accelerators, Spectrometers,Detectors and Associated Equipment*, vol. 767, pp. 146-152, 2014.

[7] B. W. Miller, S. H. Frost, S. L. Frayo, A. L. Kenoyer, E. Santos, J. C. Jones, D. J. Green, D. K. Hamlin, D. S. Wilbur, D. R. Fisher, J. J. Orozco, O. W. Press, J. M. Pagel and B. M. Sandmaier, "Quantitative single-particle digital autoradiography with alpha-particle emitters for targeted radionuclide therapy using the iQID camera," *Medical Physics*, pp. 4094-4105, 2015.

[8] L. Han, "Advances in Gamma-Ray Imaging with Intensified Quantum-Imaging Detectors," The University of Arizona, Tuscon, 2017.

[9] A. M. Clarke, B. S. McDonald, M. A. Zalavadia, D. M. Kasparek and B. W. Miller, "Characterization of Large-area iQID for Safeguards Application," *Nuclear Instruments Measurements and Analysis (NIMA)*, p. doi:10.1016/j.nima.2018.08.084, 2018.

[10] B. S. McDonald, M. A. Zalavadia, A. M. Clarke, M. Bliss, K. B. Olsen and E. R. Siciliano, "Quantitative Digital Autoradiography for Environmenta; Samples: Final Report," PNNL, Richland, 2018.

[11] T. Goorley and et al., "MCNP6.1.1-Beta Release Notes," 2014.

[12] P. Seller, S. Bell, R. J. Cernik, C. Christodoulou, C. K. Egan, J. A. Gaskin, S. Jacques, S. Pani, B. D. Ramsey, C. Reid, P. J. Sellin, J. W. Scuffham, R. D. Speller, M. D. Wilson and M. C. Veale, "Pixellated Cd(Zn)Te high-energy X-ray instrument," *Journal of Instrumentation*, vol. 6, 2011.

[13] L. Jones, P. Seller, M. Wilson and A. Hardie, "HEXITEC ASIC-a pixellated readout chip for CZT detectors," *Nuclear Instruments and Methods in Physics Research Section A: Accelerators, Spectrometers, Detectors, and Associated Equipment*, vol. 604, no. 1-2, pp. 34-37, 2009.

[14] L. R. Furenlid, E. Clarkson, D. G. Marks and H. H. Barrett, "Spatial Pileup Considerations for Pixellated Gamma-ray Detectors," *IEEE Transactions on Nuclear Science*, vol. 47, no. 4, pp. 1399-1403, 2000.

[15] M. P. Taggart, C. Payne and P. J. Sellin, "Neutron-gamma discrimination via PSD plastic scintillator and SiPMs," *Journal of Physics: Conference Series*, vol. 763, no. 10.1088/1742-6596/763/1/012007, p. 012007, 2016.

[16] G. F. Knoll, Radiation Detection and Measurement, Wiley, 1979.

[17] D. Halliday, Introductory Nuclear Physics, New York: John Wiley and Sons, Inc, 1955.

[18] I. A. E. Agency and E. B. Podgorsak, Review of Radiation Oncology Physics: A Handbook for Teachers and Students, Vienna (Austria): IAEA, 2005.

[19] N. Tsoulfanidis, Measurement and Detection of Radiation: Second Edition, Taylor & Francis, 1995.

[20] T. E. Peterson and L. R. Furenlid, "SPECT detectors: the Anger Camera and beyond," *Physics in Medicine and Biology*, vol. 56, pp. R145-R182, 2011.

[21] U. Nations, "Treaty on the Non-Proliferation of Nuclear Weapons (NPT)," United Nations, 1970. [Online]. Available: https://www.un.org/disarmament/wmd/nuclear/npt/. [Accessed 15 Janauary 2020].

[22] U. Nations, "Review Conference of the Parties to the Treaty on the Non-Proliferation of Nuclear Weapons," United Nations, 2015. [Online]. Available: https://www.un.org/en/conf/npt/2015/pdf/text%20of%20the%20treaty.pdf. [Accessed 15 January 2020].

[23] IAEA, "IAEA Safeguards Overview: Comprehensive Safeguards Agreements and Additional Protocols," IAEA, [Online]. Available: https://www.iaea.org/publications/factsheets/iaea-safeguards-overview. [Accessed 15 January 2020].

[24] B. Jones, "Next Generation Safeguards Initiative Nonproliferation and International Safeguards Summer Course," Pacific Northwest National Laboratory. PNNL-SA-110958, Richland, WA, 2016.

[25] "IAEA Safeguards Techniques and Equipment: 2011 Edition, International Nuclear Verification Series No. 1 (Rev. 2)," IAEA, Austria, 2011.

[26] Y. Kuno, D. Donohue, P. Doherty, R. Lafolie and M. Kohl, "Development and improvement of analytical techniques for U/Pu/Np/Am/Cm at the safeguards analytical laboratory," IAEA, Austria, 2006.

[27] S. L. Maxwell and J. P. Clark, "Automated spike preparation system for Isotope Dilution Mass Spectrometry (IDMS)," in *Institute of Nuclear Materials Management (INMM) conference*, Los Angeles, CA, 1990.

[28] I. A. E. Agency, "Radioactive Particles in the Environment: Sources, Particle Characterization and Analytical Techniques," IAEA, Vienna, 2011.

[29] D. Donohue, V. Maiorov, W. Raab and A. Nirschl, "A New XRF Scanner for Screening Environmental Samples," in *Symposium on Safeguards and Nuclear Materials Management, Proc. ESARDA Symp*, Stockholm, 2003.

[30] D. Donohue, Y. Ito, A. Nirschl, W. Raab and V. Maiorov, "Development of an XRF analyser with preliminary energy selection filter for screening environmental samples," in *Proceedings of an international safeguards symposium on addressing verification challenges.* , 2007.

[31] A. Dixit, "Swipe check: collecting and analysing environmental samples," IAEA, June 2016. [Online]. Available: https://www.iaea.org/sites/default/files/5722223.pdf. [Accessed 28 Oct 2020].

[32] I. A. E. A. (IAEA), "Research and Development Plan: Enhancing Capabilities for Nuclear Verification," IAEA: STR-385, January 2018. [Online]. Available: https://www.bnl.gov/ISPO/docs/STR-385-IAEA-Department-of-Safeguards-RD-Plan.pdf. [Accessed 15 January 2020].

[33] M. N. Rao, K. Yoshikawa, M. Thein, R. S. Clark and P. K. Kuroda, "Radiochemical and Physical Characteristics of Single Fallout Particles," *Health Physics*, no. 14, pp. 135-139, 1968.

[34] R. Pollanen, A. Kansanaho and H. Toivonen, "Detection and analysis of radioactive particles using autoradiography," Aerosol Laboratory, Helsinki, 1996.

[35] A. Kerkapoly, N. Vajda and T. Pinter, "Film Autoradiography Used for Hot Particle Identification,"

J. Radioanal. Nucl. Chem., vol. 265, no. 3, pp. 423-429, 2005.

[36] M. Eriksson, K. Ljunggren and C. Hindorf, "Pu hot particle separation techniques using real-time digital image systems," *Nucl. Instr. Methods Phys. Research A*, no. 488, pp. 375-380, 2002.

[37] B. W. Miller, "Radiation Imagers for Quantitative, Single-particle Digital Autoradiography of Alpha- and Beta-particle Emitters," *Semainars in Nuclear Medicine*, vol. 48, no. 4, pp. 367-376, 2018.

[38] J. Cabello, A. Bailey, I. Kitchen, A. Clark, J. Crooks, R. Halsall, M. Key-Charriere, S. Martin, m. Prydderch, R. Turchetta and K. Wells, "Digital autoradiography using CCD and CMOS imaging technology," in *2006 IEEE Nuclear Science Symposium Conference Record*, San Diego, 2006.

[39] R. F. Johnston, S. C. Pickett and D. L. Barker, "Autoradiography using storage phosphor technology," *Electrophoresis*, vol. 11, pp. 355-360, 1990.

[40] W. L. Reichert, J. E. Stein, B. French, P. Goodwin and U. Varanasi, "Storage phosphor imaging technique for detection and quantitation of DNA adducts measured by the 32P-postlabeling assay," *Carcinogenesis*, vol. 13, pp. 1475-1479, 1992.

[41] Y. Petegnief, A. Petiet, M. C. Peker and F. Bonnin, "Quantitative autoradiography using a radioimager based on a multiwire proportional chamber," *Physics in Medicine and Biology*, vol. 43, pp. 3629-3638, 1998.

[42] K. Ljunggren and S. E. Strand, "Beta camera for static and dynamic imaging of charged-paiticle emitting radionuclides in biologic samples," *Journal of Nuclear Medicine*, vol. 31, pp. 2058-2063, 1990.

[43] J. E. Lees, A. Murray, A. C. Perkins and G. W. Fraser, "Autoradiography of High-Energy radionuclides using a microchannel plate detector," *IEEE Transactions of Nuclear Science*, vol. 49, pp. 153-155, 2002.

[44] J. E. Lees, J. F. Pearson, G. W. Fraser, J. M. Hales and P. G. Richards, "An MCP-based system for beta autoradiography," *IEEE Transactions of Nuclear Science*, vol. 46, pp. 636-638, 1999.

[45] G. Mettivier, M. C. Motesi and P. Russo, "Tritium digital autoradiography with a Medipix2 hybrid silicon pixel detector," *Nuclear Instruments and Methods in Physics Research*, vol. 516, 2004.

[46] R. J. Ott, J. MacDonald and K. Wells, "The performance of a CCD digital autoradiography imaging system," *Physics in Medicine and Biology*, vol. 45, pp. 2011-2027, 2000.

[47] J. Jakubek, M. Jakubek, M. Platkevic, P. Soukup, D. Turecek, V. Sykora and D. Vavrik, "Large area pixel detector WIDEPIX with full area sensitivity composed of 100 Timepix assemblies with edgeless sensors," *Journal of Instrumentation*, vol. 9, no. 4, pp. C04018--C04018, 2014.

[48] D. Pennicard, S. Smoljanin, B. Struth, H. Hirsemann, A. Fauler, M. Fiederle, O. Tolbanov, A. Zarubin, A. Tyazhev, G. Shelkov and H. Graafsma, "The LAMBDA photon-counting pixel detector and high-Z sensor development," *Journal of Instrumentation*, vol. 9, 2014.

[49] J. W. Scuffham, M. D. Wilson, P. Selker, M. C. Veale, P. J. Sellin, S. D. Jacques and R. J. Cernik, "A CdTe detector for hyperspectral SPECT imaging," *JINST*, vol. 7, p. P08027, 2012.

[50] N. Suzui, K. Tanoi, J. Furukawa and N. Kawachi, "Recent Advances in Radioisotope Imaging Technology for Plant Science Research in Japan," *Quantum Beam Science*, vol. 3, no. 18, 2019.

[51] I. Roper Scientific, "Fiberoptic Tapers in High Resolution Scientific Imaging," Roper Scientific, Inc, Trenton, NJ, 2000.

[52] E. Britannica, "Total internal reflection," Britannica, [Online]. Available: https://www.britannica.com/science/total-internal-reflection. [Accessed 1 April 2019].

[53] I. PCO-Tech, "Intensified sCMOS Whitepaper," PCO AG, Romulus, MI, 2019.

[54] T. N. V. C. (TNVC), "TNVC Technoogy," Tactical Night Vision Company (TNVC), 2019. [Online]. Available: https://tnvc.com/technology/. [Accessed 7 April 2019].

[55] Proxivision, "High Performance Image Intensifers," PROXITRONIC Detector Systems GmbH, 2011.

[56] "Chapter 1- A Systematic View of Remote Sensing," in *Advanced Remote Sensing*, Oxford, Elsevier, 2012, pp. 1-31.

[57] S. Park, S.-W. Kwak and H.-B. Kang, "High resolution alpha particle spectrometry through collimation," *Nuclear Instruments and Methods in Physics Research Section A: Accelerators, Spectrometers, Detectors and Associated Equipment*, vol. 784, no. 1, pp. 470-473, 2015.

[58] B. W. Miller, J. M. Bowen and E. C. Morrison, "High-resolution, single-particle digital autoradiography of actinide sources using microcapillary array collimators and the iQID camera," *Applied Radiation and Isotopes*, vol. 166, no. 109348, 2020.

[59] V. Maiorov, A. Ciurapinski, W. Raab and V. Jansta, "Screening and radiometric measurement of environmental swipe samples IAEA-SM-367/10/04/P," in *International Atomic Energy Agency Symposium on international sageguards: Verification and nuclear material security*, Vienna, Austria, 2001.

[60] B. Miller, "High-Resolution Gamma-Ray Imaging with Columnar Scintillators and CCD/CMOS Sensors, and FastSPECT III: A Third-Generation Stationary SPECT Imager," The University of Arizona, Tuscon, AZ, 2011.

[61] Q. Detectors, "HEXITEC," Quantum Detectors, [Online]. Available: https://quantumdetectors.com/n/products/hexitec/. [Accessed March 2019].

[62] E. o. E. Britannica, "Amplitude," Britannica, [Online]. Available: https://www.britannica.com/science/amplitude-physics. [Accessed 21 5 2019].

[63] A. Technologies, "Agilent 33500 Series 30 MHz Function / Arbitrary Waveform Generator," Agilent Technologies, Inc, September 2010. [Online]. Available: http://ecee.colorado.edu/~ecen2270/components/33520-90001.pdf. [Accessed 23 5 2019].

[64] S. Ashken, "WHAT IS COMPUTER VISION – POST 5: A VERY QUICK HISTORY," Blippar, 4 October 2016. [Online]. Available: https://www.blippar.com/blog/2016/10/04/what-computer-vision-post-5-very-quick-history. [Accessed 2018].

[65] MathWorks, "Image Registration," MathWorks, [Online]. Available: https://www.mathworks.com/discovery/image-registration.html. [Accessed 2018].

[66] MathWorks, "Image Registration," MathWorks, 1994. [Online]. Available: https://www.mathworks.com/discovery/image-registration.html. [Accessed 19 10 2017].

[67] MathWorks, "Intensity-Based Automatic Image Registration," MathWorks, 1994. [Online]. Available: https://www.mathworks.com/help/images/intensity-based-automatic-image-registration.html. [Accessed 10 19 2017].

[68] V. Nostrand, "Attachment 7: Table 1. Uranium Series," in *Scientific Encyclopedia 5th Edition*, New York, Van Nostrand Reinhold Company, 1976, p. 1866.

[69] "IAEA Department of Safeguards Long-Term R&D Plan, 2012-2013, STR-375," IAEA, 2013. [Online]. Available: https://www.iaea.org/safeguards/symposium/2014/images/pdfs/STR_375_--_IAEA_Department_of_Safeguards_Long-Term_R%26D_Plan_2012-2023.pdf. . [Accessed 28 January 2019].

[70] I. A. E. A. (IAEA), "INFCIRC/153 : The Structure and Content of Agreements between the Agency and States required in Connection with the Treaty on the Non-proliferation of Nuclear Weapons," IAEA, Austria, 1972.

[71] L. Han, B. W. Miller, B. H. Barber and L. R. Furenlid, "Advances in iQID: Upgraded algorithms, thicker scintillators and larger area," in *IEEE Nuclear Science Symposium and Medical Imaging Conference (NSS/MIC)*, 2015.

[72] I. A. E. Agency, "Environmental Sample Laboratory," IAEA, November 2015. [Online]. Available: https://www.iaea.org/newscenter/multimedia/videos/environmental-sample-laboratory. [Accessed 15 January 2020].